AAS | IOP Astronomy

Multimessenger Astronomy in Practice

Miroslav D Filipović and Nicholas F H Tothill

Chapter 7

Gamma-Ray Astronomy

Gavin Rowell

Gamma-ray astronomy has advanced tremendously over the past couple of decades with high-impact results in a variety of scientific areas such as high-energy astrophysics, particle cosmology, Standard Model, and beyond-Standard-Model particle physics. This chapter provides an overview of the field by looking at the key results over the past few years and the connections with other areas of astronomy and identifies the key breakthroughs made. It concludes with a summary of the next generation of new gamma-ray facilities that promise to expand the field further into a mainstream astronomical activity.

7.1 Gamma Rays as Tracers of High-energy Particles and New Physics

Gamma rays are nature's highest-energy photons. They can trace elements, fundamental particle physics processes, and accelerated particles, and they can be used to indirectly probe for dark matter and its properties. For example, the fundamental particle physics of gamma-ray production from particles links them to processes producing radio to X-ray photons and neutrinos. Thus, gamma-ray studies of astrophysical particle accelerators like supernova remnants (SNRs), pulsars and their wind nebulae (PWN), black hole environments and jets (both active galactic nuclei (AGNs) and microquasars), and massive star clusters require a multiwavelength and multimessenger approach.

As the highest-energy photons, gamma rays can constrain important parameters of particle acceleration such as shock speed, acceleration timescale, magnetic fields, and the maximum particle energies attained. Gamma rays often represent a significant fraction of nonthermal energy in extreme objects and are extremely important in understanding transient and variable sources. The absorption of gamma rays from distant objects probes the extragalactic background light and allows the study of star formation and galaxy populations.

doi:10.1088/2514-3433/ac2256ch7

Gamma-ray astronomy is the most recent photon window into the universe to be exploited. Gamma rays are the highest-energy photons and theoretically extend to energies beyond $\sim 10^{20}$ eV (matching the highest-energy cosmic rays detected), although to date the highest-energy gamma rays actually measured have energies of about 10^{14} eV. Figure 7.1 illustrates the multimessenger spectrum and highlights the various underlying physics processes.

We will concentrate our discussion here on gamma-ray astronomy at energies above about 100 MeV, which has seen great advances in the past two decades. We will, however, include a historical overview of MeV to multi-TeV gamma-ray astronomy. The electron rest mass at 0.51 MeV is generally considered to be the starting energy of gamma rays although the term "soft" gamma rays is often applied to facilities working down to 0.1 MeV or so. Gamma rays in the energy range ~0.1 to 10s of MeV (MeV gamma-ray astronomy) are associated with nuclear spectral lines from supernova and massive stars, the annihilation of electron–positron pairs, and broadband gamma rays from low-energy cosmic rays and electrons (via the same processes that produce >GeV gamma rays, which we will discuss later). Some further discussion of MeV gamma-ray astronomy results and perspectives may be found in Pinkau (2009), Roland (2016), and De Angelis et al. (2017).

7.1.1 A Brief History of MeV to Multi-TeV Gamma-Ray Astronomy

It could be argued that the field attracted serious attention in the mid-1960s with the observations of bursts of gamma rays by the Vela satellites launched for the US military (Klebesadel et al. 1973). This followed the first detection of gamma rays in 1962 by the Explorer XI satellite (Kraushaar & Clark 1962). The mid-1960s also saw many efforts with high-altitude balloons that proved unsuccessful (see review by Weekes 1988 as well as Book 1, Chapter 1.3.6). However, astronomy was only possible, at least in part, once precise locations of the gamma-ray emission could be pinpointed, leading to the situation today where many gamma-ray sources are now spatially resolved down to the arcminute level.

The OSO-3 space mission (Kraushaar et al. 1972) provided the first glimpse of the gamma-ray sky in MeV to GeV gamma rays, revealing large-scale emission along

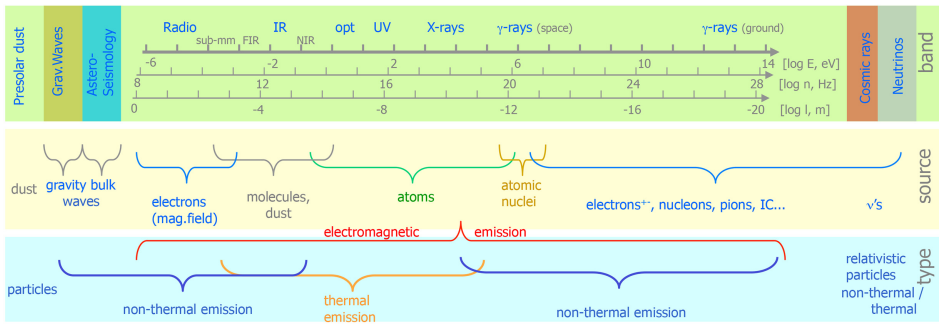

Figure 7.1. Multimessenger spectrum with underlying physics processes responsible for the photons and particles. Image credit: Roland (2016).

the plane of the Milky Way, clearly indicating its origin in our own galaxy. This was followed by the SAS-2 (Fichtel et al. 1975) and COS-B (Bignami & Hermsen 1983) missions. The latter established about 25 discrete gamma-ray sources and permitted the first detailed counterpart studies. These groundbreaking detectors utilized the conversion of gamma rays into a cascade of electrons, positrons, and lower-energy gamma rays via a spark chamber. Using this approach with better technology, the late 1990s saw the launch of the EGRET mission on board the Compton Gamma-Ray Observatory (CGRO).

EGRET greatly expanded the number of MeV to GeV gamma-ray sources to over 200 (Hartman et al. 1999) and enabled the first detailed views of the diffuse emission along the Galactic Plane and made significant contributions to the understanding of pulsars. Although EGRET's capabilities allowed the discrete gamma-ray sources to be pinpointed to better than 1°, the first real hints of the challenges that lay ahead came with the fact that a large fraction of the Galactic Plane sources were unidentified in that they had no obvious counterparts, a situation that continues today for GeV gamma-ray astronomy (see, e.g., Thompson 2015).

The Fermi-LAT (Large Area Telescope; Atwood et al. 2009) was launched in 2008 and replaced EGRET, following de-orbiting of the CGRO in 2000. Still operating today, Fermi-LAT utilizes the pair-creation tracking technique to reconstruct the arrival direction of gamma rays. In this process, incoming gamma rays create electron–positron pairs, which then go on to create ion tracks in the silicon strip tracking detectors. The silicon strip detectors measure the direction of these pairs, which enables reconstruction of the incoming gamma-ray to a precision approaching 0.1° at energies >10 GeV. Fermi-LAT has been a great success in revolutionizing GeV gamma-ray astronomy with the detection of over 5000 sources in the 0.1 to 100 GeV-energy band (Abdollahi et al. 2020).

Moving to higher energies, gamma-ray astronomy from multi-GeV to beyond 100 TeV energies relies on detection with ground-based telescopes. This is due to extraterrestrial gamma-ray photon fluxes following a steeply falling power law in their energy distribution and hence space-based telescopes do not have sufficient collection area to gather useful photon statistics.

Gamma rays of energy above a few GeV will, upon entering Earth's atmosphere, initiate an extensive air shower (EAS) of secondary particles (predominantly electron and positrons) that generate Čerenkov radiation. The most sensitive ground-based telescopes today image this Čerenkov light to reconstruct the arrival direction and energy of the gamma-ray. For gamma rays of several TeV energies and above, and depending on the ground-level altitude above sea level, the secondary EAS particles can be detected at ground level, and several telescopes have exploited this avenue effectively.

The huge size of the Čerenkov light pool on the ground (approaching 1 km^2) and large spread of the EAS particles nicely compensate for the low photon fluxes in the TeV energy range, enabling the ground-based telescopes to carry out highly sensitive studies of steady and time-varying sources. For some recent detailed reviews of the history and various techniques, see Hillas (2013), Mirzoyan (2014), de Naurois & Mazin (2015), and Fegan (2019).

The early days of ground-based gamma-ray astronomy were devoted to establishing the observational existence of Čerenkov light from EAS and in 1953, the first such detection was made using a photomultiplier (PMT) coupled to a searchlight mirror (Galbraith & Jelley 1953). Nesterova & Čudakov (1955) were to later repeat this in 1955. The late 1950s and early 1960s saw the first multipixel arrays (about 10 to 20) of PMTs being used to revealed the somewhat extended nature of the Čerenkov EAS image (Brennan et al. 1958; Boley & Macoy 1961; Millar et al. 1962). However, the use of an image intensifier and phosphor storage system by Hill & Porter (1961), who photographed details of the Čerenkov image elongation, clearly demonstrated that the EAS arrival direction could be determined to within about 0.5°.

Following Hillas' (1985) proposal to use a detailed parameterization of the Čerenkov image shape (the angular distribution), and related ideas put forward by Pliasheshnikov & Bignami (1985), it was not until 1989 that the first convincing detection of TeV gamma rays came (9σ statistical significance above the cosmic ray, CR, background; Weekes et al. 1989). The source in question was the Crab Nebula (a PWN), recognized as the standard candle for TeV astronomy. This was achieved using the 37 PMT pixel camera installed on the Whipple telescope in Arizona, USA. Interestingly in the 1970s, a related method to detect Čerenkov light using widely separated telescopes in Narrabri, Australia (the "double-beam" technique) provided a tantalizing hint for a signal from our nearest AGN, Centaurus A (Grindlay et al. 1975), but this method was never developed further.

By the late 1990s, the power of stereoscopic Čerenkov imaging with more than one telescope was proven by the HEGRA IACT System (Daum et al. 1997), as well as the benefits of a high-resolution camera pixelation on a single telescope by CAT (Barrau et al. 1998). Besides the imaging Čerenkov technique, several other methods have proved themselves, with the most successful being the direct detection of EAS particles at ground level via an array of large water tanks in the MILAGRO experiment (Abdo et al. 2007b), and to a certain extent, Čerenkov detection via its lateral distribution with the use of thermal solar towers (e.g., Gingrich et al. 2005; Paré et al. 2002).

Today, ground-based gamma-ray observatories such as HESS (High energy stereoscopic system), https://www.mpi-hd.mpg.de/hfm/HESS/; VERITAS (Very energetic radiation imaging telescope array system), https://veritas.sao.arizona.edu/; and MAGIC (Major atmospheric gamma imaging cherenkov), https://magic.mpp.mpg.de/ (stereoscopic air Čerenkov arrays); ARGO-YGJ (Aielli et al. 2006) (Resistive Plate Counter array); HAWC, High-altitude water cherenkov, www.hawc–observatory.orghttps://www.hawc-observatory.org/ (water Čerenkov array following on from MILAGRO; Smith 2005) lead the way at TeV energies, while the Fermi-LAT space mission at GeV energies still operates.

7.2 The Status of MeV to TeV Gamma-Ray Astronomy

In this section we will review the present-day situation in gamma-ray astronomy, starting with an overview of the catalogs of sources across the gamma-ray bands.

Figure 7.2 presents an all-sky view of some all-sky views based on selected source catalogs spanning the sub-MeV to the multi-TeV gamma-ray bands.

The catalogs shown here (from Swift-BAT, Fermi-LAT, and TeVCat (combining results from all TeV gamma-ray facilities TevCat: catalog of TeV gamma-ray sources, http://tevcat2.uchicago.edu/) focus primarily on discrete sources, either

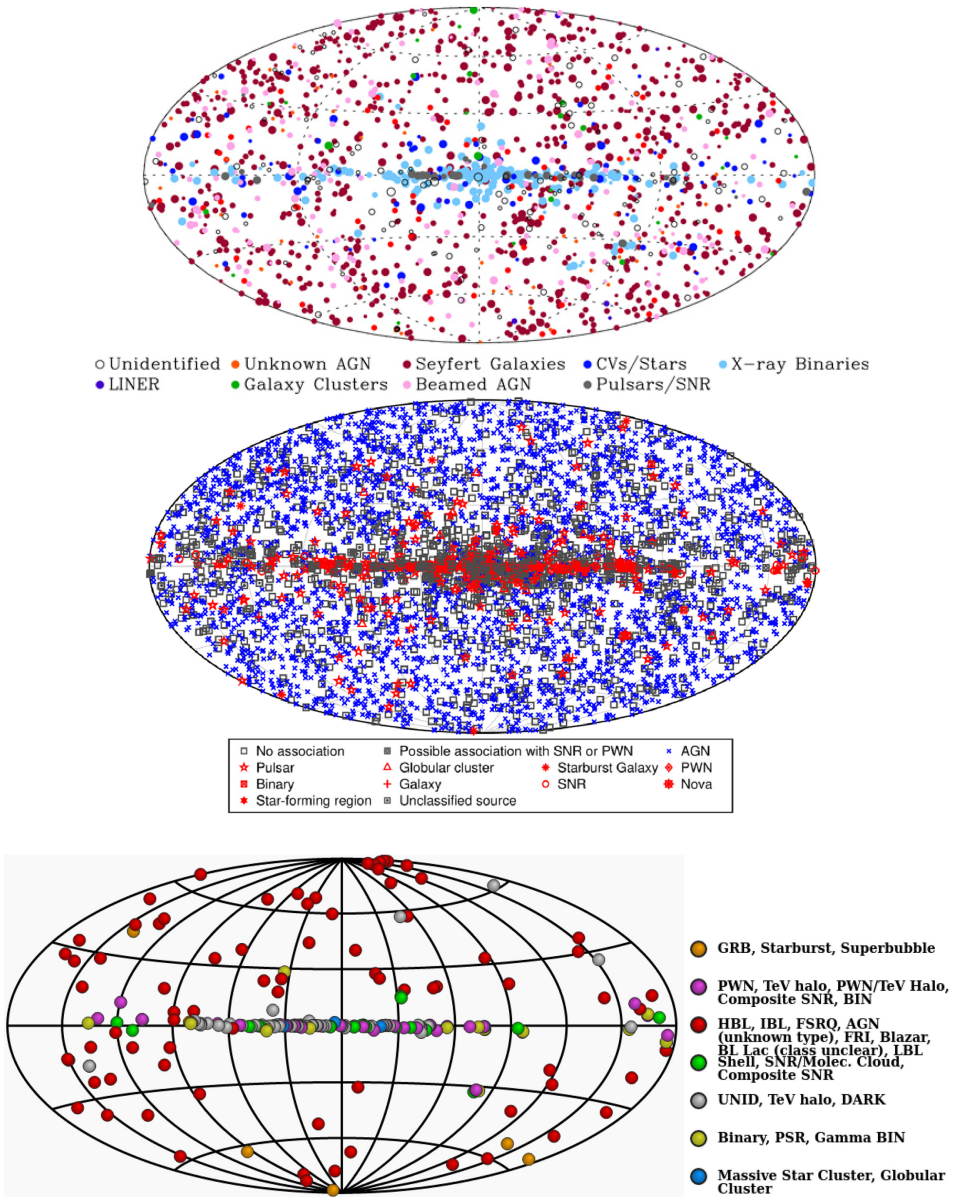

Figure 7.2. All-sky gamma-ray source catalogs in various bands: sub-MeV (top: 14 keV to 0.2 MeV; Oh et al. 2018), GeV (middle: 0.1 to 100 GeV; Abdollahi et al. 2020) and TeV (bottom: >0.1 TeV; TeVCat: catalog of TeV gamma-ray sources, http://tevcat2.uchicago.edu/).

steady or variable in flux. Another important catalog is that from COMPTEL (0.7–30 MeV; Schönfelder et al. 2000), which provided the first detailed look at the MeV gamma-ray sky and paved the way for the Swift-BAT and INTEGRAL missions, which have cataloged many hundreds of sources up to a few MeV (Oh et al. 2018; Bird et al. 2007; Bouchet et al. 2008). The AGILE mission overlaps Fermi-LAT in the GeV band and has provided its catalog (Bulgarelli et al. 2019).

We note a number of these facilities (e.g., Fermi-LAT, Ajello et al. 2019; Fermi-GBM, von Kienlin et al. 2020; and Swift-BAT, Lien et al. 2016) have separate catalogs devoted to one-off transient sources such as gamma-ray bursts (GRBs) in the hard X-ray to soft gamma-ray band up to 1 MeV.

Additionally, there are several degree-scale features not tied to individual sources, such as the ^{26}Al line at 1.809 MeV from COMPTEL and INTEGRAL (Diehl et al. 1995; Bouchet et al. 2015) tracing nuclear reactions in massive star and core-collapse supernovae, the e^+/e^- annihilation line at 0.511 MeV (Knödlseder et al. 2005) tracing electron production, and the Galactic Plane diffuse emission tracing the broad population of Galactic cosmic rays and electrons (Ackermann et al. 2012).

What is abundantly clear from these catalogs is the wide variety of source types that emit gamma rays. In the sub-MeV and MeV bands, accreting sources such as X-ray bursts (XRBs; high mass and low mass) and AGNs tend to dominate the Galactic and extragalactic populations, respectively. In the GeV and TeV bands, AGNs (with various subtypes) dominate the extragalactic population, while the Galactic population is more varied with PWNe, SNRs, pulsars, gamma-ray binaries, globular clusters, star-forming regions being represented.

Notably, the fraction of unidentified gamma-ray sources has become significant in the GeV and TeV bands, particularly in the Galactic population. These sources have no obvious counterparts in other wavelengths, and this fact has motivated news efforts to probe deeper with renewed observations across the radio to X-ray domains. We will leave further discussion to later sections devoted specifically to the Galactic and extragalactic source populations.

It is, however, worth noting the growth in source numbers over time. Figure 7.3 charts the growth of X-ray and gamma-ray source numbers up to 2019 in what is known as the "Kifune" plot, a logarithmic format first shown by Kifune (1996).

What is obvious is that the growth rate of source numbers across the X-ray and gamma-ray domains is rather similar, reflecting the development of new facilities. To date there are now over 5000 and 200 sources in the GeV and TeV gamma-ray domains, respectively.

7.3 GeV to TeV Gamma-Ray Production

In this section we will briefly review the physics behind GeV to TeV gamma-ray production and see how such gamma-ray emission is deeply connected to relativistic particles and to the production of other photons spanning radio waves to X-rays.

The mechanism most often invoked to explain the existence of relativistic particles is shock acceleration (in some extreme environments, particle acceleration by electric fields and by reconnection in magnetic fields is also discussed). More

specifically, the so-called diffusive shock acceleration process (e.g., Drury 1983) appears to operate in a variety of astrophysical sources, as we will highlight later. An overview of shock acceleration is presented in Book 1 (Section 7.3). We will here provide just a summary of the spectral properties of the accelerated particles to underpin our discussion of gamma-ray production. Diffusive shock acceleration leads to a nonthermal energy distribution of relativistic particles, described mathematically as a power law. A simple form for the resulting differential particle flux number versus energy dN/dE or particle spectrum, is given by

$$dN/dE = KE^{-\Gamma} \exp(-E/E_c), \tag{7.1}$$

where Γ is the power-law spectral index, E_c is a cutoff energy determining the strength of the exponential term, and K a normalization. The spectral index can be expressed in the form $\Gamma \approx (r+1)/(r-1)$, where the shock compression factor $r = 4$ for strong shocks, thus giving $\Gamma = 2$ (variation to this are predicted according to shock properties and nonlinear effects). The exponential term encapsulates the upper-energy limit of the accelerator, and such limits are imposed by the shock environment (e.g., shock speed, size, and magnetic field—see Hillas 1985) and/or

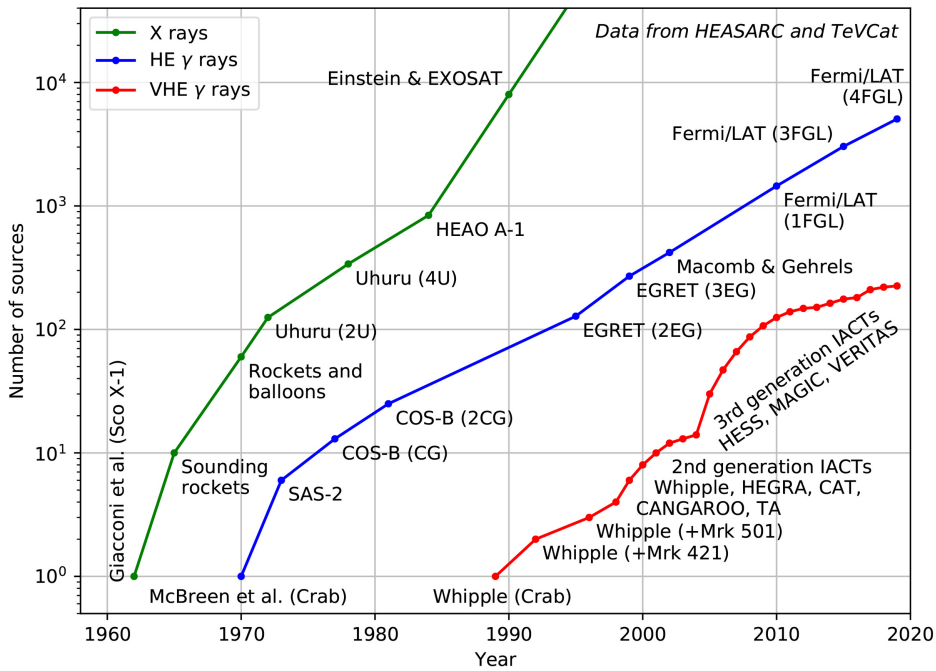

Figure 7.3. The latest "Kifune" plot charting the growth of X-ray and gamma-ray source numbers over time to 2019, available from https://github.com/sfegan/kifune-plot, Copyright 2017, Stephen Fegan. The data for the X-ray and high-energy (HE gamma-ray) source counts are from "How Many Known X-Ray (and Other) Sources Are There?", https://heasarc.gsfc.nasa.gov/docs/heasarc/headates/how_many_xray.html and the very high-energy (VHE) or TeV gamma-ray source counts are from TeVCat: catalog of TeV gamma-ray sources, http://tevcat2.uchicago.edu/.

radiative losses such as synchrotron emission usually for electrons (see Zirakashvili & Aharonian 2007). We refer the reader to Aharonian (2004) for an in-depth look at these topics.

GeV to TeV gamma rays are produced by relativistic cosmic rays (protons, nuclei) and electrons in hadronic and leptonic radiative processes respectively. The spectral shape of the resulting gamma rays is heavily influenced by the particle spectrum properties (Equation (7.1)).

The hadronic process involves the inelastic collision of cosmic rays with ambient protons or nuclei and is often labeled proton–proton (or pp) collisions. The ambient protons/nuclei (N) are often in the form of interstellar gas either, neutral (predominantly), or ionized and proceed according to the following reactions:

Hadronic–Cosmic rays p of energy $E_{\rm p}$ colliding with matter nuclei N:

$$p + N \rightarrow N' + \pi^{\circ}, \pi^{+}, \pi^{-} \ (\pi \approx \text{equal numbers}) \tag{7.2}$$

$$\pi^{\circ} \rightarrow \gamma\,\gamma \ \left(E_{\gamma} \sim 0.17 E_{\rm p}\right) \tag{7.3}$$

$$\pi^{+} \rightarrow \mu^{+} + \nu_{\mu} \rightarrow e^{+} + \nu_{e} + \overline{\nu_{\mu}} \tag{7.4}$$

$$\pi^{-} \rightarrow \mu^{-} + \overline{\nu_{\mu}} \rightarrow e^{-} + \overline{\nu_{e}} + \nu_{\mu}. \tag{7.5}$$

Thus, the GeV to TeV gamma rays with energy E_{γ} result from π° decay and the decay of charged $\pi^{\pm}$ leads to muons, electrons, and their associated neutrinos. The neutrinos are detected by telescopes such as IceCube and KM3Net (see Chapter 8). Interestingly, the electrons generated via the decay of muons can then provide secondary radio to X-ray synchrotron emission.

The energy-loss rate for cosmic-ray protons interacting with a ambient medium of number density n (typical units cm^{-3}) is given by $dE_p/dt = (n\sigma_{\rm pp} f c)E_{\rm p}$, where $f \sim 0.5$ (Gaisser et al. 2016) is the inelasticity for single interactions, $\sigma_{\rm pp}$ is the total cross section for pp collisions, and c is the speed of light. Figure 7.4 presents $\sigma_{\rm pp}$ versus proton kinetic energy $T_{\rm P} = E_{\rm P} - m_{\rm p}c^2$.

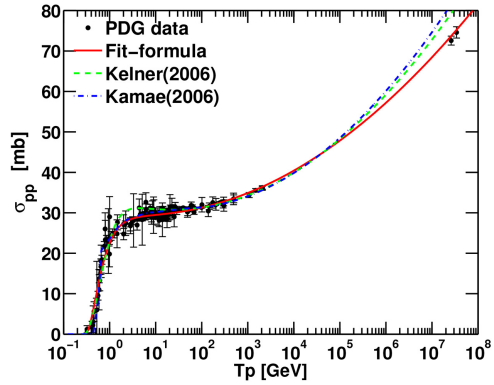

Figure 7.4. Total pp cross section $\sigma_{\rm pp}$ versus proton kinetic energy $T_{\rm P}$ with functional parameterizations given by Kafexhiu et al. (2014). Image adapted with permission from Kafexhiu et al. (2014), Copyright 2014 by the American Physical Society.

From this we can see that *pp* collisions become important for energies above a few GeV. Below this energy, ionization losses are dominant (see Padovani et al. 2009).

For electrons, several processes are relevant, namely inverse-Compton (IC) scattering, synchrotron emission, and bremsstrahlung.

Leptonic–Inverse-Compton Scattering:

TeV electrons will upscatter soft photons such as the cosmic microwave background CMB and local IR, optical, and UV components to TeV energies via the IC process[1]:

$$e^{-}+\gamma_{\mathrm{soft}} \rightarrow e^{'-}+\gamma_{\mathrm{TeV}}. \tag{7.6}$$

Assuming a monoenergetic soft photon energy ω with number density n_{ph}, the IC energy-loss rate for electrons with Lorentz factor $\gamma = E_{\mathrm{e}}/(m_{\mathrm{e}}c^2)$ is $dE_{\mathrm{e}}/dt = \frac{4}{3}\sigma_{\mathrm{T}}c\omega n_{\mathrm{ph}}\gamma^2$. Here, σ_T is the Thompson cross section, and the energy-loss rate expression given above is valid for the Thompson regime where $b = 4\omega\gamma << 1$ (typical for the CMB, and IR soft photon targets and TeV electrons). Following Aharonian (2004), the Klein–Nishina (KN) limit occurs for $b >> 1$ (often on optical, UV fields, or >100 TeV electrons on the CMB) in which case the energy-loss rate follows $dE_{\mathrm{e}}/dt = \frac{3}{8}(\sigma_{\mathrm{T}}cn_{\mathrm{ph}}(\ln b - 11/6))/\omega$. An extreme version of IC is synchrotron self-Compton (SSC) emission (often invoked in AGN and GRB jets), whereby electrons upscatter their own X-ray synchrotron photons to TeV energies.

Leptonic–Synchrotron Radio to X-Rays (electron acceleration in magnetic fields):

Electrons will be accelerated in a magnetic field via the Lorentz force (see Book 1 for a discussion). Here, we just note the electron's energy-loss rate given by the expression $dE_{\mathrm{e}}/dt = \frac{4}{3}\sigma_T c U_{\mathrm{B}}\gamma^2$, where $U_B = B^2/8\pi$ is the magnetic field energy density (cgs units) and B is the magnetic field flux density (Gauss). As a rule of thumb in a magnetic field typically found in our Galaxy (few microgauss), GeV and TeV electrons will give rise to radio and X-ray synchrotron emission respectively. For extreme magnetic fields such as that around neutron stars, a related emission process known as curvature radiation becomes important as relativistic electrons follow their highly curved magnetic field lines.

Leptonic–Bremsstrahlung:

Electrons can also convert their energy to TeV photons upon scattering in the field of a nucleus (within ambient matter of density n_{p}). The energy-loss rate is $dE_{\mathrm{e}}/dt = cm_{\mathrm{p}}n_{\mathrm{p}}(E_{\mathrm{e}}/X_o)$ for the radiation length $X_o = \frac{7}{9}(\rho/(n_{\mathrm{p}}\sigma_o)$ (gm cm^{-2}). Here, σ_o is the pair production cross section, m_p is the proton mass, and $\rho = m_{\mathrm{p}}n_{\mathrm{p}}$ is the matter mass density. Bremsstrahlung is usually subdominant unless the ambient matter density is very large, $n > 10^4$ cm^{-3}, and the B-field low (<few microgauss), which may be found in some environments, such as large quiescent clouds. The IC and synchrotron process will therefore generally dominate and thus compete for the electron's energy.

[1] Also see Section 2.1.3 and Book 1, Section 7.3.1.

An extremely useful way to characterize the importance of these process is via their so-called cooling time $t = E/\dot{E}$, which is the time taken for a population of particles to radiate all of their energy away at a loss rate $\dot{E} = dE/dt$. A short cooling time implies fast conversion of particle energy to photon energy, and hence, such a process will dominate over other competing processes with a longer cooling time. This issue is particularly important for electrons where synchrotron and IC radiation losses usually compete. The cooling times for all four processes discussed above in units of years are

$$t_{\rm pp} = \left(n\sigma_{\rm pp} fc\right)^{-1} \approx 5.3 \times 10^7 (n/{\rm cm}^3)^{-1} \ {\rm yr}, \tag{7.7}$$

$$t_{\rm IC} \approx 3 \times 10^5 (U_{\rm rad}/{\rm eV/cm}^3)^{-1} (E_{\rm e}/{\rm TeV})^{-1} \Big) f_{\rm KN}^{-1} \ {\rm yr}, \tag{7.8}$$

$$t_{\rm Sync} \approx 12 \times 10^6 (B/\mu{\rm G})^{-2} (E_{\rm e}/{\rm TeV})^{-1} \ {\rm yr}, \tag{7.9}$$

$$t_{\rm Br} \approx 4 \times 10^7 (n/{\rm cm}^3)^{-1} \ {\rm yr}, \tag{7.10}$$

where $E_{\rm e}$ is the electron energy in TeV units. The KN suppression factor $f_{\rm KN} \approx (1 + b)^{-1.5}$ is included in the IC cooling time.

7.4 Gamma Rays and Multimessenger Links

From the previous section we can now appreciate the intimate links between gamma-ray emission and nonthermal emission at lower energies from radio up to X-rays. Here, we will discuss some relevant examples.

The close connection between the TeV gamma-ray IC $F_{\rm IC}$ and X-ray synchrotron $F_{\rm sync}$ fluxes was pointed out by Aharonian et al. (1997). By taking the ratio of their cooling times $t_{\rm IC}/t_{\rm Sync}$, a simple expression for the flux ratios can be found such that $F_{\rm IC}/F_{\rm sync} = 10(B/10\mu{\rm G})$. Here, a δ-function approximation for the synchrotron and IC cross sections, and IC scattering of the CMB in the Thompson regime are assumed (Book 1, Chapter 4).

Thus, a comparison of the TeV gamma-ray and X-ray synchrotron fluxes can provide an independent estimate of the magnetic field B in an extreme environment. Because the synchrotron process also extends down to the radio band, we can see the close connections across the radio to TeV gamma-ray bands in the context of leptonic processes. Furthermore, the secondary synchrotron component as a by-product of the hadronic process provides additional links to the radio to X-ray bands.

Multiwavelength photon spectra from the hadronic and leptonic processes can be computed by integrating over the underlying particle spectrum (Equation (7.1)) multiplied by the relevant cross sections and particle to photon conversion efficiencies. For leptonic processes the relevant cooling times can be smaller than the age of the source (e.g., often for synchrotron emission versus a few kiloyear age for an SNR). This will lead to a significant alteration or evolution of the electron spectrum, and this should be tracked to ensure the correct "evolved" electron

spectrum and subsequent synchrotron, IC, and bremsstrahlung photon components are calculated. Another influence will be the time-dependent nature of the particle accelerator, and these are broadly categorized into "impulsive" (e.g., SNRs operating for a few thousand years) or "continuous" (e.g., particle injection from a pulsar in a PWN) types. The reader is referred to Aharonian & Atoyan (1996), Kelner et al. (2006), Manolakou et al. (2007), and Hinton & Hofmann (2009) for further discussion and useful expressions.

As an illustrative example, Figure 7.5 presents some conceptual energy spectra arising from a particle spectrum of the form given by Equation (7.1).

From here, we can see that observations in the radio, X-ray, and gamma-ray bands are crucial in constraining the properties of the underlying relativistic particles. An overriding scientific goal is to discriminate the leptonic and hadronic processes in order to progress our understanding of accelerator properties. Because, as is apparent in Figure 7.5, there are a variety of spectral shapes characteristic of the leptonic and hadronic processes, detailed spectral studies across the radio, X-ray, and gamma-ray bands can help discriminate the two processes.

However, spectral discrimination is not always feasible due to limited statistics, narrow energy coverage within a band, limited gamma-ray angular resolution, competing thermal sources of radio and X-ray emission, and complex particle propagation properties that can create a variety of spectral shapes (e.g., see Aharonian & Atoyan 1996). The next-generation gamma-ray facilities such as the Cherenkov Telescope Array (CTA Consortium et al. 2019) aims to address many of these issues in the TeV gamma-ray band with its arcminute angular resolution and wide energy coverage (spanning about three decades). Further discussion of CTA and other next-generation facilities is left for a later section.

Another crucially important way to discriminate hadronic from leptonic processes is via their distinct spatial signatures expected in relation to the ambient interstellar gas. As shown in Equations (7.2) and (7.7), gamma-ray emission is directly coupled to the ambient gas properties such as its density n. More specifically,

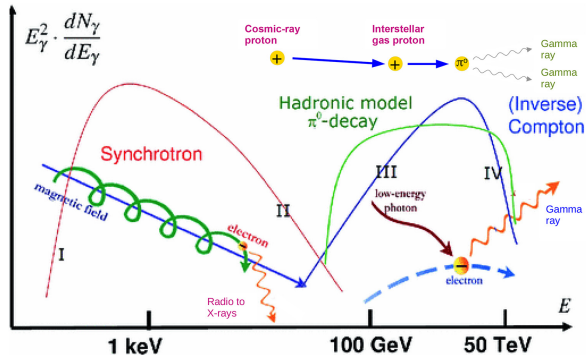

Figure 7.5. Conceptual spectral energy distributions of photons from leptonic (synchrotron, inverse Compton) and hadronic (π^0-decay) processes. Image adapted from Spurio (2015), with permission of Springer. Leptonic bremsstrahlung (not shown) is often subdominant compared to the inverse-Compton component.

the gamma-ray flux from this process $F_\gamma \propto n_{\rm CR}(E_{\rm p})n$, where $n_{\rm CR}$ is the energy-dependent density of cosmic rays interacting with the ambient gas. Thus, the gamma-ray emission to first order is expected to spatially correlate with the ambient gas density (or its mass), assuming $n_{\rm CR}(E_{\rm p})$ does not vary too much with the gas (we will later discuss how this can occur). Because the ambient gas can be traced by a variety of spectral lines, usually in the radio band, this relationship outlines a further important linkage between gamma-ray and radio astronomy.

Already there are several examples of gamma-ray sources (discussed later) spatially matching associated gas clouds traced by spectral lines such as the carbon monoxide (CO) and carbon monosulfide (CS) molecules (tracing molecular hydrogen H_2), as well as the H I spin–flip transition tracing atomic hydrogen. A number of interstellar gas surveys (Dame et al. 2001; Mizuno & Fukui 2004; Jackson et al. 2006; Walsh et al. 2011; Jones et al. 2012; Taylor et al. 2003; McClure-Griffiths et al. 2005; Stil et al. 2006) have been exploited so far, as well as recent surveys (e.g., Braiding et al. 2018; Umemoto et al. 2017; Wang et al. 2020; Dickey et al. 2013) reaching higher resolution (0.5′; not all yet completed). In such sources the hadronic process is implied for the gamma-ray emission, signaling the presence of cosmic-ray accelerators. We note that the leptonic bremsstrahlung process (Equation (7.10)) follows a similar relationship with the ambient gas density, but as discussed earlier, this is very rarely dominant due to stronger electron energy losses via the synchrotron and IC processes.

The hadronic process via Equations (7.4) and (7.5) also signals an obvious linkage to neutrino astronomy (another process via cosmic-ray and photon interactions that also produces neutrinos—see Chapter 8). The neutrino emission will also spatially correlate with the ambient gas density under the same assumptions given above for the gamma-ray emission. Additionally, the spectral signature of neutrinos will be somewhat similar to that of hadronic gamma rays (see, e.g., Kelner et al. 2006). As neutrinos are an unambiguous signature of hadronic interactions, they are seen as the smoking gun to confirm the presence of cosmic rays, and this issue has been a major driver behind facilities like IceCube and KM3NeT, as discussed in Chapter 8.

7.5 Galactic TeV Gamma-Ray Sources

In this section we will review the Galactic TeV gamma-ray source population and highlight some key results that have emerged. Where necessary, we will make reference to the GeV gamma-ray source population as revealed by the Fermi-LAT mission which now lists over 5000 sources (Abdollahi et al. 2020). Figure 7.6 presents Galactic surveys maps at TeV gamma-ray energies from the HESS and HAWC facilities (HESS Collaboration et al. 2018a; Albert et al. 2020d) covering the southern and northern skies, respectively. These are to date the most comprehensive Galactic Plane surveys at these energies. Smaller-scale surveys have been published by HESS (Galactic Center region, HESS Collaboration et al. 2018e), VERITAS (Cygnus region, Abeysekara et al. 2018a; Galactic Center

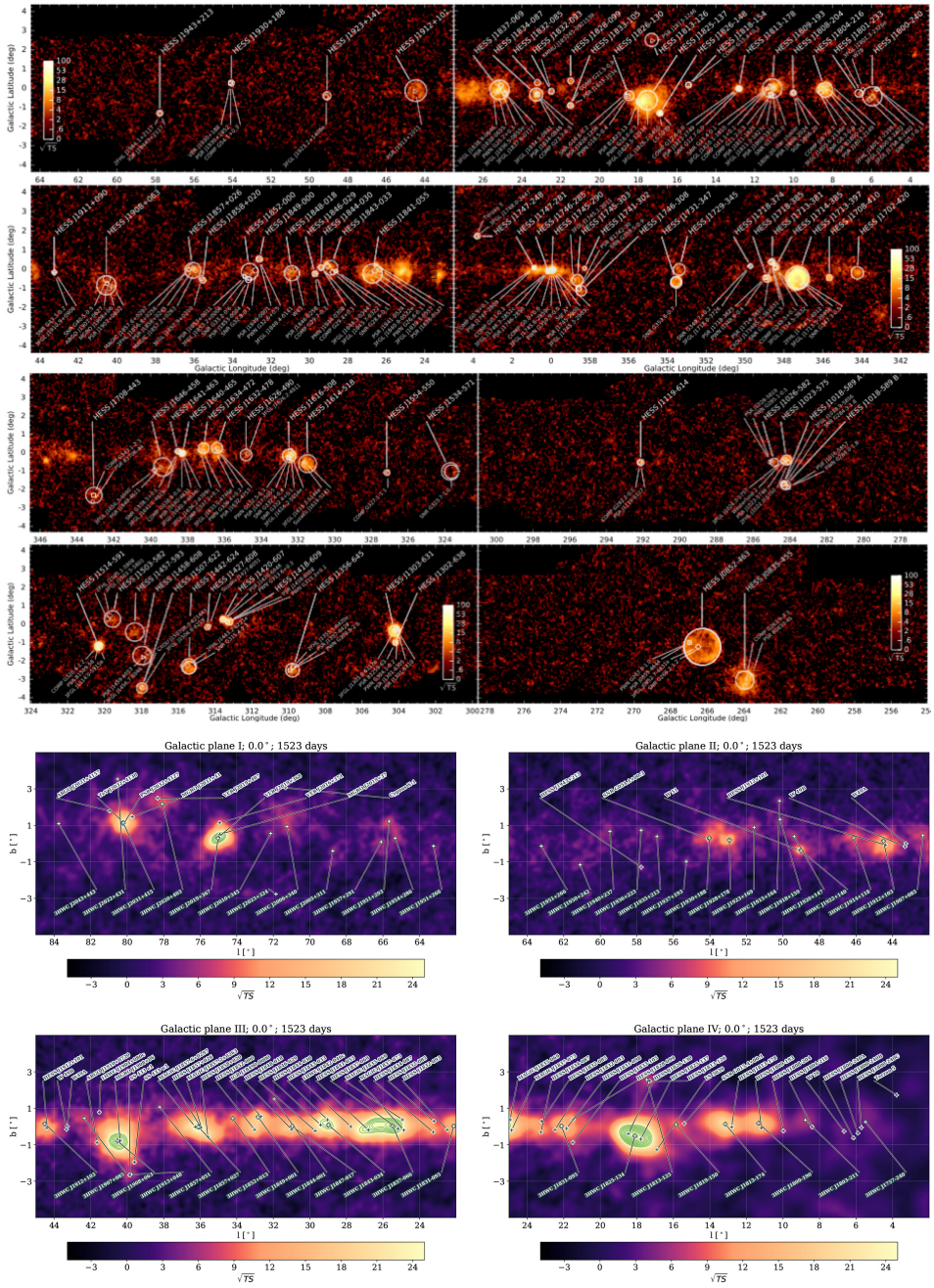

Figure 7.6. TeV gamma-ray survey sky maps from HESS (top four rows) (HESS Collaboration et al. 2018a, reproduced with permission © ESO) and HAWC (bottom four rows) (Albert et al. 2020d) covering the southern and northern Galactic Plane, respectively (note: not all coverage is shown here). Counterpart names are also listed. The sky-map color scales are in units of $\sqrt{\mathrm{TS}}$, representing the statistical significance of gamma-ray features above background fluctuations due to cosmic-ray events.

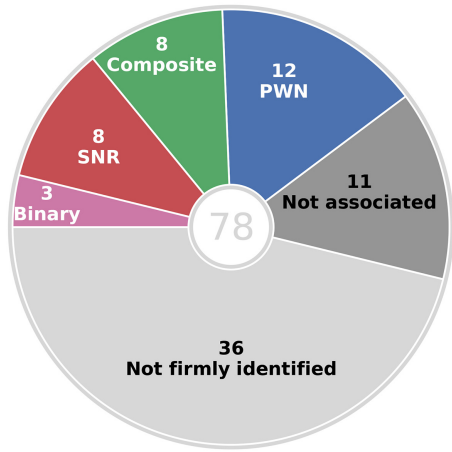

Figure 7.7. TeV gamma-ray source identifications from the HGPS (HESS Collaboration et al. 2018a, reproduced with permission © ESO).

region, Archer et al. 2016), and MAGIC (Galactic Center region, MAGIC Collaboration et al. 2020b).

The HESS Galactic Plane Survey (HGPS; HESS Collaboration et al. 2018a), focusing on the southern hemisphere, has revealed 78 Galactic TeV gamma-ray sources, the bulk of the Galactic population so far. A total of 31 of these sources are associated with multiwavelength counterparts of the following types: SNRs (shell-type), PWNe, composite (composite SNR with interior PWN), binary (binary systems containing an interacting compact object and massive star). These associations follow from morphological, positional, and variability evidence that link the TeV sources to their counterparts at lower energies, usually in the radio and X-ray bands. The good angular resolution of HESS, in the 3′ to 5′ range, has enabled many of these identifications.

A striking aspect of the survey is the large fraction of TeV gamma-ray sources that remain unidentified, with 36 sources listed as not firmly associated with any counterpart although there may be one nearby (for example, an adjacent SNR or a powerful pulsar potentially driving a PWN), and 11 sources with no hints for any association at all. The second HAWC catalog (Abeysekara et al. 2017b) focusing on the northern hemisphere lists 39 TeV sources. Due to HAWC's large (∼1 sr) field of view, it also covered the extragalactic sky. To date, 65 sources have been cataloged, with 20 new sources and the rest associated with known TeV sources (from HESS, VERITAS, or MAGIC). Although its angular resolution at 12′ to 60′ is not as good as that for HESS, HAWC's large field of view and 24 hr operation has enabled it to reveal a number of low-brightness, degree-scale gamma-ray sources, as well as some source reaching energies beyond 50 TeV. Indeed, HAWC's highest-energy catalog has revealed nine sources with emission >56 TeV and three with emission >100 TeV (Abeysekara et al. 2020). All of these sources are spatially close to sources previously identified by HAWC, HESS, VERITAS, and/or MAGIC, and thus, they likely

represent their upper-energy extremes. We will discuss some of these extreme sources in the context of PeVatrons later in Section 7.5.6.

7.5.1 Shell-type Supernova Remnants

Shell-type SNRs have been discussed as the main accelerators of Galactic cosmic rays for over 80 years. It was Baade & Zwicky (1934) who first raised this possibility, and then was then followed up by Morrison (1958) and Ginzburg & Syrovatskii (1964), who considered the origin of the nonthermal radio emission in SNRs. Later, diffusive shock acceleration theory operating in SNR shock fronts was put forward as the ideal mechanism to achieve particle acceleration (Krymskii 1977; Axford et al. 1977; Bell 1978; Blandford & Ostriker 1978), and over time, this has been developed further (e.g., Drury 1983; Bell 2004). The reviews by Hillas (2005), Letessier-Selvon & Stanev (2011), and Aharonian (2013) are suggested reading for further details on this topic.

Some key fundamental arguments favoring SNRs are

1. The luminosity of Galactic cosmic rays ($\sim 10^{41}$ erg s^{-1}) can be met by the supposed Galactic SNR population (roughly three per century) requiring about 10% to 30% of an SNR's kinetic energy of 10^{51} erg being converted to cosmic rays, and
2. Diffusive shock acceleration operating in SNRs can provide a cosmic-ray power-law index of $\Gamma \approx 2.0$, in agreement with the observed cosmic-ray spectral index after accounting for propagation.

The first predictions of hadronic TeV gamma-ray emission (heavily dependent on the factor n/d^2, for gas density n and SNR distance d) from SNRs from Drury et al. (1994), Naito & Takahara (1994), and Aharonian et al. (1994) provided impetus for studies by the first Čerenkov imaging facilities. Following a number of unconvincing claims and upper limits, the first solid detection of the very young SNR Cas A was made by the stereoscopic HEGRA IACT System (Aharonian et al. 2001).

Today, over a dozen SNRs are identified as TeV gamma-ray sources (and over 20 as GeV gamma-ray sources), either via their shell-like morphology, positional overlap with the radio or X-ray shell, or overlap with adjacent interstellar gas. The gamma-ray shell-like morphology, seen in the very young (<500 yr) and young SNRs ($<10^4$ yr) is interpreted via leptonic and/or hadronic processes. The leptonic process is invoked due to the presence of shell-like nonthermal synchrotron X-ray emission (identified via featureless broadband X-ray spectra), signaling the presence of multi-TeV electrons. Evidence for the hadronic process in the very young and young SNRs has come from consideration of the clumpy gas inside and adjacent to the SNR shocks. The mature SNRs ($>10^4$ yr) have gamma-ray emission that tend to overlap large adjacent interstellar gas clouds, and this has been interpreted as evidence for the hadronic process in which cosmic rays are escaping the SNR shock and propagating into the surrounding gas. These SNRs have likely evolved beyond the so-called Sedov–Taylor phase in which the bulk of the cosmic rays are accelerated. The hadronic interpretation is further backed up by the general lack

of nonthermal X-ray emission associated with the mature SNRs because the X-ray synchrotron cooling time is typically less than 10^4 yr (that is, the nonthermal X-ray emission only lasts for a few thousand years). The gamma-ray spectral shapes of the SNRs have provided additional clues. Figure 7.8 summarizes a number of GeV to TeV gamma-ray spectra for SNRs spanning a range of ages.

Here, we can see some clear differences in spectral shapes. The mature SNRs ($>10^4$ years) tend to exhibit GeV-peaked spectra with rather soft spectral indices ($\Gamma \approx 2.6$) in the TeV band. Such a spectral shape is consistent with the energy-dependent escape and diffusion of cosmic rays and their interaction with adjacent gas clouds (e.g., Aharonian & Atoyan 1996; Gabici 2011). The presence of the "pion bump" or sharp rolloff below 135 MeV (the rest mass–energy of $\pi°$; Ackermann et al. 2013) for some mature SNRs is also seen as strong evidence for the hadronic process.

For the young SNRs with strong peaks in the TeV band, both hadronic and leptonic processes have supporting evidence. The hard GeV spectral shape ($\Gamma < 2$) is particularly suggestive of the IC process. However, the energy-dependent interaction of cosmic rays with the clumpy gas is believed to suppress the GeV emission, thereby allowing a hadronic interpretation.

The very young SNRs (two examples so far: Cas A and Tycho) show broad GeV to TeV emission with a peak at a few GeV. Their GeV to TeV spectral broadness is consistent with the hadronic process (in contrast to the leptonic process producing a narrower IC peak). A tentative hint of increasing GeV emission from SN 1987A, now believed to have entered the SNR phase, was recently reported by Malyshev et al. (2019). We should also point out that gamma-ray emission from supernova events (SNe) linked to the initial cataclysmic collapse and powered by the SN ejecta interacting with the progenitor circumstellar medium has attracted attention (Waxman & Loeb 2001; Murase et al. 2011). Indeed, a recent hint for fading transient GeV emission has been reported from SN2004dj ($d = 3.5$ Mpc) (Xi et al.

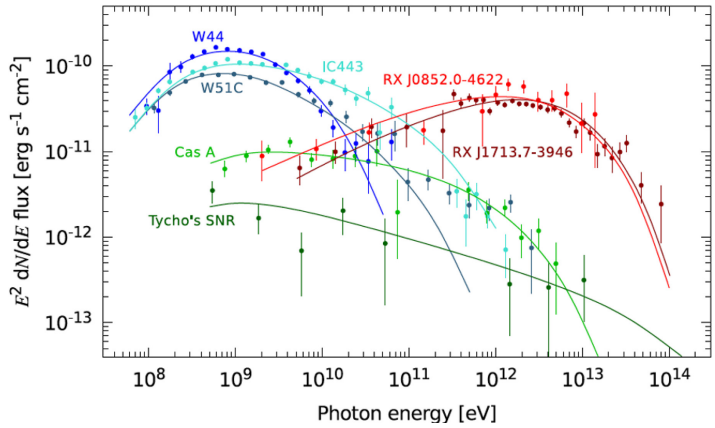

Figure 7.8. GeV to TeV gamma-ray spectra from a number of shell-type SNRs. Very young (<500 yr, Cas A, Tycho) SNRs are shown in green, young SNRs ($<10^4$ yr, RXJ1 713.7−3946, RXJ0 852.0−4622) in red and mature SNRs ($>10^4$ yr, W44, W51C, IC 443) shown in blue/cyan. Image credit: Becker Tjus & Merten (2020), with permission from Elsevier.

2020a), which is a Type IIP SNe where such interactions might occur. We will now discuss some SNR examples to highlight the progress made so far.

The young, 1600 yr old TeV-bright SNR RXJ1713.7−3946 is probably the most studied of all gamma-ray SNRs to date. It exhibits a clear shell-like morphology in the radio, X-rays, GeV, and GeV to TeV gamma-ray bands. Formally, both pure leptonic and hadronic scenarios have been proposed using feasible parameters for the total particle energy budgets ($\sim 10^{47-48}$ erg in electrons and $\sim 10^{49-50}$ erg in cosmic-ray protons), although somewhat low magnetic fields and/or intense optical photon fields are required in the leptonic scenario (HESS Collaboration et al. 2018c). A mixed scenario (e.g., Zirakashvili & Aharonian 2010; Gabici & Aharonian 2014) in which the hadronic process arises from dense gas clumps inside the SNR has gained acceptance. Significant effort has gone into studying the interstellar gas toward RXJ1713.7−3946 in an effort to further examine the viability of any hadronic interpretation and disentangle the hadronic and leptonic components (e.g., Moriguchi et al. 2005; Fukui et al. 2012; Maxted et al. 2012; Sano et al. 2013, 2020). Figure 7.9 presents the latest HESS >2 TeV and earlier XMM-Newton X-ray images from HESS Collaboration et al. (2018c) and Acero et al. (2009b). The GeV gamma-ray and radio continuum images can be found in Lazendic et al. (2004) and Federici et al. (2015).

The study by Fukui et al. (2012) revealed a general correspondence between the interstellar gas and the TeV gamma-ray emission in an annular region focusing on the SNR rim, providing the first suggestion of a global hadronic component. In recent years, attention has focused on the energy-dependent penetration of cosmic rays into dense gas clumps (first pointed out by Gabici et al. 2007). In the limited age of the SNR, the GeV cosmic rays do not penetrate far into the dense clumps due to magnetic turbulence from the SNR shock disturbance (Zirakashvili & Aharonian 2010; Inoue et al. 2012; Celli et al. 2019), thereby providing a natural explanation for the suppressed GeV emission. The most recent work by Sano et al. (2020) mapped the interstellar molecular gas on arcsecond scales and in fact confirmed the very clumpy nature of the gas downstream from the SNR shock.

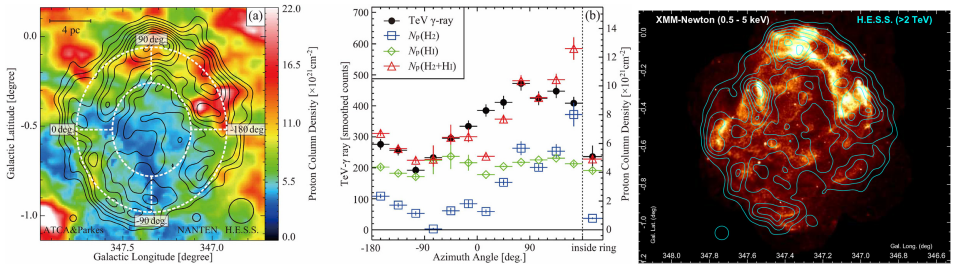

Figure 7.9. Left and middle panels: interstellar gas column density (N_p) image with HESS TeV contours (from Aharonian et al. 2007b) and their resulting azimuthal comparison from Fukui et al. (2012). Right panel: HESS >2 TeV (cyan contours; 10 to 40 counts/pixel) and XMM-Newton (0.5 to 5 keV X-ray; 0 to 1.27×10^{-4} photons cm^{-2} s^{-1} arcmin^{-2}) images using data from HESS Collaboration et al. (2018c) and Acero et al. (2009b). The HESS point-spread function (68% containment radius) is shown as the cyan circle at the bottom left. The XMM-Newton resolution at 6″ is too small to show.

The mature SNR W28 is well known for the extensive adjacent molecular gas surrounding its radio shell (and center filled with thermal X-ray emission). A cluster of 1720 MHz OH masers toward the northeast cloud is evidence of an SNR shock and interstellar gas interaction (Frail et al. 1994; Claussen et al. 1997). Since the discovery of TeV emission overlapping the molecular gas (Aharonian et al. 2008c), W28 has become a prime example to explore the escape of cosmic rays from SNRs and diffusive propagation to the ambient gas as the OH maser emission confirms the close proximity of the gas. Figure 7.10 illustrates the multiwavelength picture toward W28, including the radio SNR shell, TeV gamma-ray emission, and surrounding interstellar gas from various tracers (Maxted et al. 2017).

The TeV gamma-ray emission around W28 remains the best example of a TeV/gas overlap and along with the lack of any nonthermal X-ray emission, the clearest example of where the hadronic process is at work. Interpretation of this and the GeV emission (also from other SNRs with adjacent gas) has looked at the details of cosmic rays escaping from SNRs, the effect of diffusion properties, and the role of accelerated ambient cosmic rays (e.g., Fujita et al. 2009; Yan et al. 2012; Nava & Gabici 2013; Gabici 2014; Cui et al. 2018; Tang 2019).

Another potential example of a mature SNR is HESS J1832−085, which was until recently thought to be an unidentified TeV gamma-ray source. Using the low-frequency radio GLEAM survey by MWA (Hurley-Walker et al. 2017) and VLA survey by Anderson et al. (2017), a radio SNR counterpart of G23.11+0.18 was identified by Maxted et al. (2019). The same authors also found the SNR overlaps with interstellar gas surrounding a bubble in the 4–5 kpc distance range and no shell-like nonthermal X-ray emission. These observations generally support a mature SNR origin and highlight the close relationship between the hadronic gamma-ray

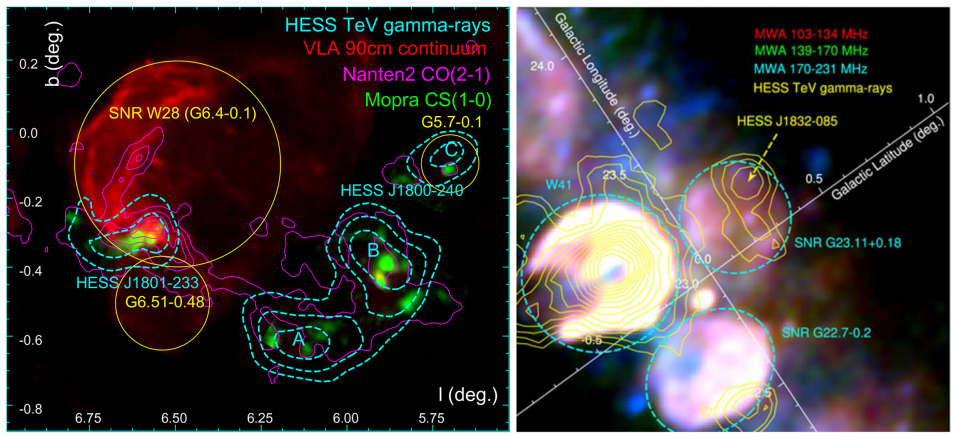

Figure 7.10. Left panel: multiwavelength view of the W28 SNR (G6.4−0.1). The HESS TeV gamma-ray contour (dashed cyan) are overlaid. Other information includes the VLA radio continuum and molecular gas traced by the Nanten2 and Mopra radio telescopes. Other SNRs are indicated with yellow circles. Image credit: Maxted et al. (2017), with the permission of AIP Publishing. Right panel: MWA radio image of the SNR G23.11+0.18 (dashed cyan) with HESS TeV contours (solid yellow) are overlaid. Image credit: Maxted et al. (2019).

and radio synchrotron emission, which have similarly long cooling times ($>10^4$ yr) as per Equations (7.7) and (7.9).

Finally, we want to highlight three additional shell-like TeV gamma-ray sources (HESS Collaboration et al. 2018d), which are suspected to be mature SNRs. At the time of its discovery, HESS 1534−571 was identified as a likely counterpart to the candidate radio SNR G232.7−1.0 (Green et al. 2014; Maxted et al. 2018), making this the first SNR to be discovered in gamma rays. HESS J1912+101 is linked to a TeV "halo" HAWC source (2HWC J1912+099), a GeV source (Zhang et al. 2020), and may also have a polarized radio counterpart (Reich & Sun 2019). On the other hand, HESS J1614−518 still has no obvious counterpart(s).

7.5.2 Pulsar Wind Nebulae (PWNe) and Gamma-Ray Halos

Pulsar-powered PWNe represent the most numerous type of identified Galactic TeV gamma-ray source (Figure 7.7) and a small fraction (< few percent) of the identified GeV Galactic sources (HESS Collaboration et al. 2018a; Abdollahi et al. 2020). The gamma-ray emission is attributed to the IC process from multi-TeV electrons accelerated at a termination shock well away from pulsar's magnetosphere. A termination shock is set up by a pressure balance between the pulsar's electron wind and that of the surrounding SNR ejecta and ambient gas and electrons accelerated at this shock create the PWN. The Crab Nebula (a.k.a. M1 or SN 1054) is the archetype PWN and the first established TeV gamma-ray source (Weekes et al. 1989). Much of the theory behind PWNe and the relativistic flow of electrons and positrons driving them was developed to explain the Crab Nebula's steady emission from the radio to the X-ray bands (e.g., Pacini & Salvati 1973; Rees & Gunn 1974; Kennel & Coroniti 1984; Reynolds & Chevalier 1984 and review by Gaensler & Slane 2006). The Crab Nebula emission is well explained by the SSC model due to the high magnetic field, ~0.3 mG, required, whereas external IC emission (on soft fields such as the CMB) is invoked for other PWNe.

Since the recent discovery of two degree-scale low-surface-brightness TeV sources from nearby pulsars by HAWC (Abeysekara et al. 2017a), the concept of "gamma-ray halos" (or specifically, "TeV halos"; Linden et al. 2017) has become accepted as a probable late stage of PWNe. Figure 7.11 provides a sketch (Giacinti et al. 2020) of the three main stages of PWNe evolution discussed today (see also Blondin et al. 2001).

During stage 1 ($\lesssim$ 10 kyr), the SNR forward shock (FS) propagates outward and a reverse shock (RS) forms as it slows down. The contact discontinuity (CD) separates the SNR ejecta and the forward-shocked interstellar medium (ISM). Beyond the pulsar wind termination shock (TS), the electrons, driven by the pulsar wind, form the PWN which is still inside the SNR. This stage is often when we would see "composite" SNRs (in radio to gamma rays), where the SNR shock is visible as shell-like radio emission and the interior harbors the PWN, which is bright in X-rays and gamma rays (via synchrotron and IC emission, respectively). In stage 2 (10 to 100 kyr), the SNR has evolved beyond the Sedov–Taylor phase and has started to dissipate into the ISM. The PWN morphology is influenced by the incoming RS and

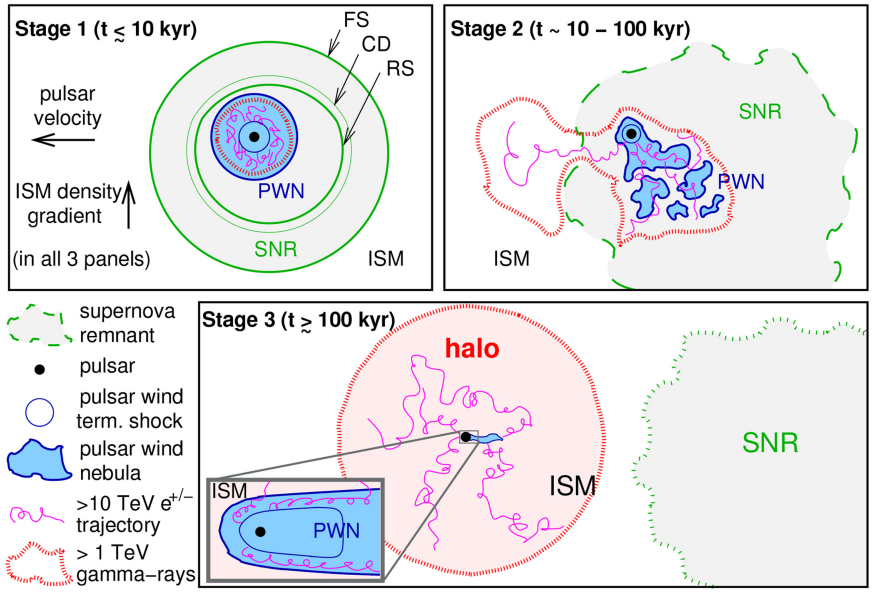

Figure 7.11. Three stages in the evolution of a PWN. Image credit: Giacinti et al. (2020), reproduced with permission © ESO.

can become irregular. The PWN follows the kick velocity of the pulsar and has likely migrated to the edge of the SNR. The PWN electrons begin to escape the PWN boundary and propagate away. In stage 3 (>100 kyr), the PWN has migrated well away from the SNR, most of the PWN electrons have escaped and now propagate diffusively in the undisturbed interstellar gas, and little or no sign of the SNR remains. The "TeV halo" signature of a PWN can be a feature from stage 2 onwards.

The evolution described above provides the morphological clues to identify PWNe, with the most obvious ingredient being a nearby pulsar. The X-ray morphologies of PWNe are extremely varied, reflecting the unique conditions under which they were formed and evolve in (e.g., interstellar gas, supernova properties, pulsar kick velocity; see Reynolds et al. 2017). The associated TeV gamma-ray emission is usually much more spatially extended than that of the X-rays, reflecting the short synchrotron cooling times near the pulsar (high B-field well above 10 μG and decreasing with distance from the pulsar) versus the longer IC cooling time, which is independent of the magnetic field.

From the HGPS, the identified and candidate PWNe are so far mostly linked to relatively young pulsars with spin-down power $\dot{E} > 10^{35}$ erg s^{-1}, and their TeV gamma-ray efficiency improves with pulsar characteristic age τ_c and physical offset from the TeV PWN emission peak (HESS Collaboration et al. 2018b; Figure 7.12). This behavior follows an accepted model of PWN evolution (see HESS Collaboration et al. 2018b) consistent with stage 1 and/or stage 2 as explained above. The trends can also be explained in simple terms via the PWN's decreasing magnetic field with age giving rise to an increased fraction of electron energy going

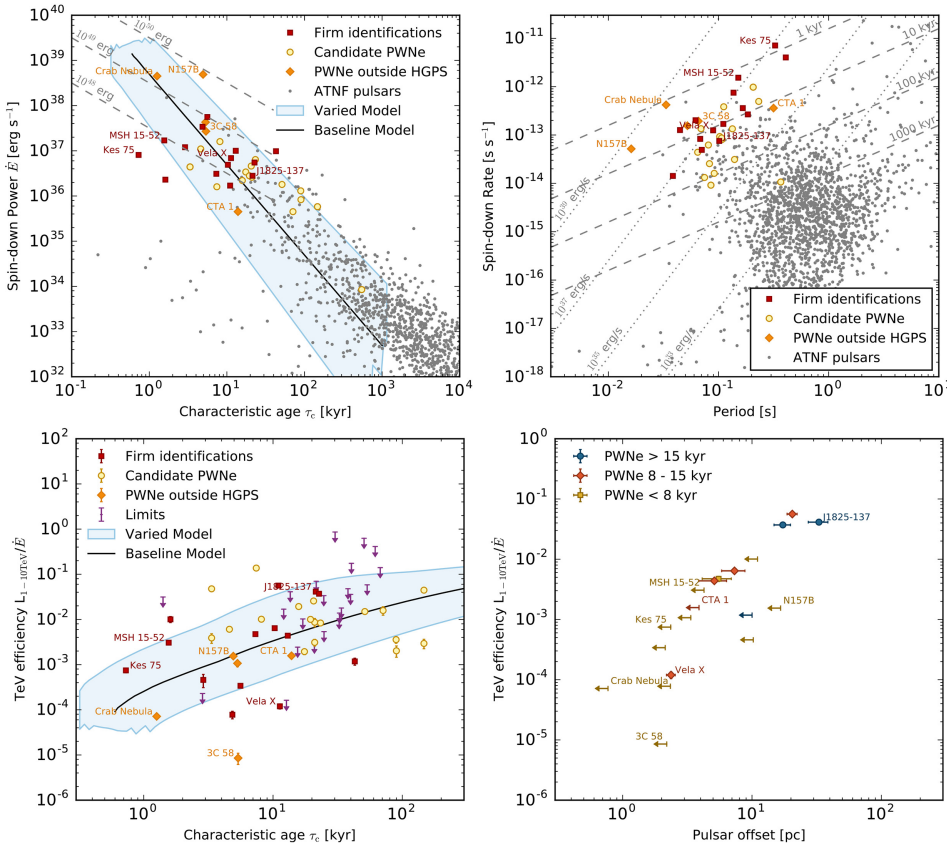

Figure 7.12. Summary of pulsar properties according to their TeV PWN status. Top left to bottom right: pulsar spin-down power $\dot{E}$ versus characteristic age τ_c; pulsar spin-down rate versus period; TeV luminosity efficiency ($L_{1-10\,\mathrm{TeV}}/\dot{E}$) versus τ_c; and TeV luminosity efficiency versus pulsar physical offset from the TeV PWN center. Images credit: HESS Collaboration et al. (2018b), reproduced with permission © ESO.

into the IC process at the expense of X-ray synchrotron emission (see discussion in Section 7.4).

The offset aspect is explained of course by a pulsar's migration distance increasing with age. The TeV halos extending up to 5° in diameter detected by HAWC are found toward two rather old ($\tau_c > 10^5$ yr) nearby pulsars, Geminga and PSR B0656 +14 (associated with the Monogem SNR), less than 300 pc distant with moderate spin-down power (few $\times 10^{34}$ erg s^{-1}). These two examples would be clear outliers against the trends determined by HESS Collaboration et al. (2018b) in Figure 7.12 as expected, given they represent the much older stage 3. We note the recent study by Di Mauro et al. (2021) suggests the presence of GeV halos around some of the bright HAWC TeV sources, indicating that lower-energy GeV electrons may be escaping the PWN region during stage 3. Additionally, Sudoh et al. (2019) has suggested many of the unidentified TeV sources could be related to TeV halos.

Identifying PWNe among the large number of unidentified TeV sources is a key challenge. An obvious morphological signature, at least for stage 1 and stage 2, is a gamma-ray spectral hardening (higher fraction of high-energy gamma rays) toward the underlying pulsar. The most prominent example here is HESS 1825−137 (Aharonian et al. 2006d), the brightest and one of the largest TeV PWN, where GeV spectral evolution has also recently been seen (Principe et al. 2020). Similar evidence has been seen in HESS J1303−631 and the Vela PWN (HESS Collaboration et al. 2012; Reynolds et al. 2017). Figure 7.13 shows the compelling spectral evolution in the TeV band for HESS J1825−137.

The spectral evolution can be used in a relatively simple way to infer the leptonic nature of the TeV gamma-ray emission, and we can use HESS J1825−137 as an example. This PWN is powered by the pulsar PSR J1826−1334 with period $P = 101$ ms, spin-down power $\dot{E} = 3 \times 10^{36}$ erg s^{-1}, characteristic age $\tau_c \sim 20$ kyr, and dispersion-measure distance $d \sim 4$ kpc. The spectral steepening with distance from the pulsar requires emission cooling times to be less than or roughly equal to the source age (20 kyr). Looking at the cooling times for IC $t_{\rm IC}$ on the CMB photon field and synchrotron $t_{\rm Sync}$ emission (Equations (7.8) and (7.9)) for electrons of energy 60 TeV (producing 1 TeV gamma rays and few keV X-rays) and a magnetic field of $B = 10$ μG (certainly expected near the pulsar), we can see that $t_{\rm Sync} \sim$ 1 kyr <<

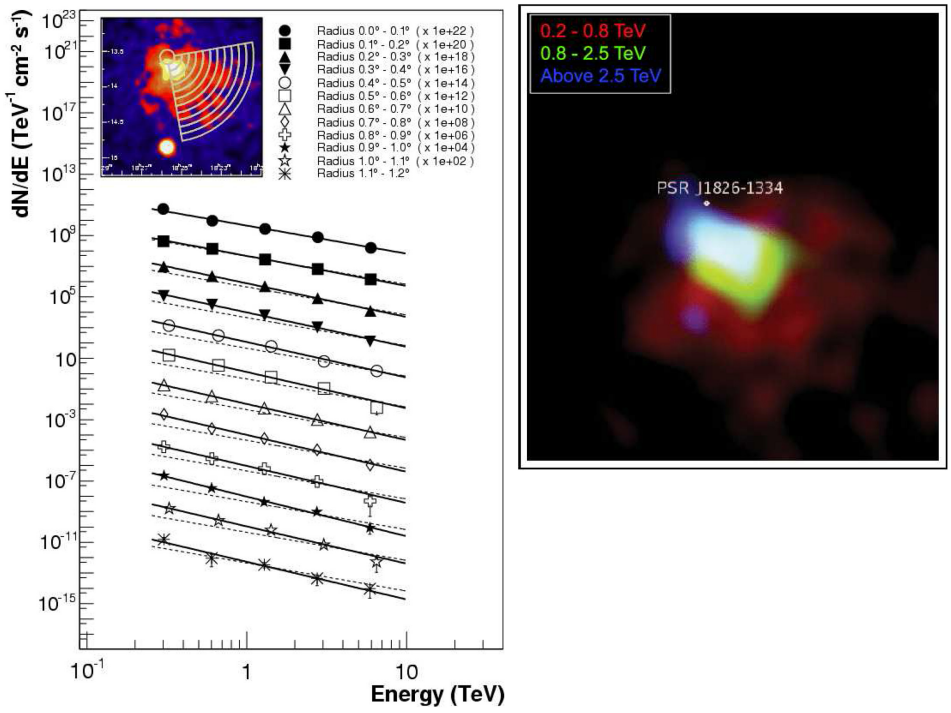

Figure 7.13. Left: spectral steepening of HESS J1825−137 versus distance from the pulsar PSR J1826−1334 (Image credit: Aharonian et al. 2006d, reproduced with permission © ESO). Above: multi-energy-band image of HESS J1825−137 graphically showing the spectral steeping. Image credit: Funk et al. (2008).

$t_{iC} \sim 20$ kyr. Thus, both IC and synchrotron cooling will occur, with the latter being dominant near the pulsar. The PWN magnetic field will decrease with distance (e.g., $B \sim r^{-0.7}$ for radius r) from Van Etten (2011), and so we expect the IC process to gradually become more dominant farther from the pulsar. This gives rise to a compact X-ray synchrotron nebula close to the pulsar with the TeV gamma-ray emission extending much farther out. This is indeed what is seen toward HESS J1825−137 and many other PWNe. In a hadronic scenario, we note that $t_{pp} >> 20$ kyr by some orders of magnitude as the gas density should be very low ($n < 0.1$ cm^{-3}) as argued below. Thus, the hadronic scenario is implausible unless extreme turbulence can diffusively trap cosmic rays for a very long time in the PWN, an unlikely situation, and at odds with the large PWN extension. In fact, additional transport (advection) beyond diffusion may be needed to explain the 100 pc diameter of the PWN (HESS Collaboration et al. 2019).

Another way to help identify PWNe is by studying the interstellar gas toward them. Because PWNe are expanding into a core-collapse SNR bubble, the interstellar gas density there should be quite low ($n < 0.1$ cm^{-3} or so). Thus, a void or bubble in the interstellar gas is a telltale sign. Additionally, the general asymmetric morphology of PWNe is largely influenced by the inhomogenous interstellar gas surrounding the SNR (because the SNR reverse shock is influenced by this gas) and thus moderate to large gas clouds can be expected to be found adjacent to PWNe. The expected distance to the gas or a void in the gas (measured by a radio spectral line with a distance-dependent Doppler shift) can further be constrained according to the underlying pulsar's dispersion measure. Indeed, a large ($>10^4$ M$_\odot$) gas cloud has been found to the north of HESS J1825−137 (Lemiere et al. 2005; Voisin et al. 2016), which helps explain the development of this PWN in a southerly direction. Additional studies of the gas toward other PWN and PWN candidates from the HGPS have recently been carried out (Voisin et al. 2019), revealing several potential gas cloud "partners" to these sources.

During the 2007 to 2010 period, the AGILE and Fermi-LAT missions detected several large flares from the Crab Nebula (Tavani et al. 2011; Abdo et al. 2011). Further flares have been detected since then up to late 2014 (Arakawa et al. 2020). These flares came as a complete surprise, and immediately changed the notion of PWNe as steady, reliable sources. Indeed, up to that point, the Crab Nebula was long considered the standard candle in gamma-ray astronomy (as it is in many other photon bands). The rapid nature of the flares suggests a powerful acceleration mechanism requiring a very strong magnetic field ~1 mG (slightly above the field invoked in the SSC model to explain the steady PWN emission as discussed earlier). Even more revealing was the maximum energy of the flares, which reached 500 MeV, challenging the theoretical maximum energy that electrons could attain due to synchrotron losses under induced electric field conditions in magnetospheric shocks. Acceleration via magnetic reconnection within current sheets was a way to avoid this problem, and this mechanism (well studied as an acceleration mechanism in solar flares) is now often invoked.

We conclude this section with a brief comment on the emerging class of magnetar wind nebulae (MWNe; reviewed by Reynolds et al. 2017). Magnetars are extremely

magnetic neutron stars (fields ~1000× stronger than regular neutron stars) powered largely by magnetic field energy, rather than spin down due to rotational losses. As a result, their outflows and nebulae are quite temporal in nature and often associated with giant flaring and other transient events. Small-scale X-ray nebulae have been detected around several magnetars (although some may be interpreted as dust-scattered halos) and thus present opportunities for the potential to generate gamma-ray emission. We discuss one example magnetar (SGR 1806−20) in Section 7.5.5 due to the presence of overlapping extended TeV emission.

7.5.3 Pulsars

The pulsed emission from neutron stars is driven by their rotation and originates from within the neutron star's magnetosphere. The GeV Fermi-LAT mission has dramatically expanded the number of GeV gamma-ray pulsars over the past decade (Caraveo 2014; Grenier & Harding 2015; Abdollahi et al. 2020), and the current list[2] extends to 253 examples as of April 2020. Among these, 118 are millisecond pulsars, making them a significant fraction of the total, with the rest labeled as "young" pulsars. About 30% of the young pulsars are radio quiet in that their pulsations are detected in the gamma-ray band, not the radio. The MeV to GeV gamma-ray emission is generally believed to originate farther out (in the so-called outer gap and/or slot gap regions) from the pulsar compared to radio emission region thought to be associated close to the neutron star surface in the polar cap region. In recent years, however, gamma-ray emission models involving reconnection acceleration in a current sheet just beyond the light cylinder (where the tangential speed of magnetic field lines reach the vacuum speed of light) have gained some favor. The beam-opening angle of the gamma-ray emission is therefore somewhat wider than that of the radio beam.

The MeV to GeV gamma-ray emission mechanism is usually discussed as curvature radiation, although synchrotron emission has been discussed in the context of acceleration within current sheets. Inevitably, the extreme magnetic field experienced by the gamma rays in this region will mean that they can be readily converted into electron/positron pairs, which can then generate their own synchrotron emission and create secondary lower-energy gamma rays in a cascade process (e.g., Daugherty & Harding 1982, 1983). The end result is that the gamma-ray spectrum exhibits a strong exponential cutoff in the multi-GeV-energy regime and can often be parameterized as

$$dN/dE = KE^{-\Gamma} \exp(-E/E_c)^b, \tag{7.11}$$

where b is the "sharpness" of the cutoff, and the other terms are defined as per Equation (7.1). From the second Fermi-LAT pulsar catalog (Abdo et al. 2013), E_c is typically a few GeV, Γ is in the range 1 to 1.8, and b is unity for all pulsars except for

[2] Public list of LAT pulsars: https://confluence.slac.stanford.edu/display/GLAMCOG/Public+List+of+LAT-Detected+gamma-ray+Pulsars.

a few where $b < 1$, suggesting a subexponential cutoff (see also Abdollahi et al. 2020 for a somewhat different functional form).

Due to the GeV exponential cutoff, detecting pulsed emission at TeV gamma-ray energies has been a much greater challenge owing to the >20 GeV threshold of ground-based gamma-ray telescopes. However, the past decade has seen rapid improvement in the <50 GeV performance of telescopes such that four pulsars are now detected—Crab Pulsar (Aliu et al. 2008; Ansoldi et al. 2016), Vela Pulsar (HESS Collaboration et al. 2018g), PSRB 1706−44 (Spir-Jacob & Djannati-Ata 2019), and Geminga (MAGIC Collaboration et al. 2020a). Not surprisingly, these four are the brightest pulsars in the Fermi-LAT pulsar catalog. Figure 7.14 shows the pulsed energy spectra for three of these pulsars.

The most remarkable aspect is the clear evidence for an additional pulsed spectral component extending beyond the exponential cutoff form determined by Fermi-LAT for the Crab and Geminga pulsars. The extra component is now measured up to 1 TeV in the case of the Crab. The curvature radiation (and synchrotron) model used to explain the pulsed GeV emission is somewhat challenged by these results, as it seems to require rather extreme conditions to reach TeV energies (e.g., Viganò & Torres 2015). Instead, the IC upscattering of X-ray photons by electrons accelerated in the outer gap region at

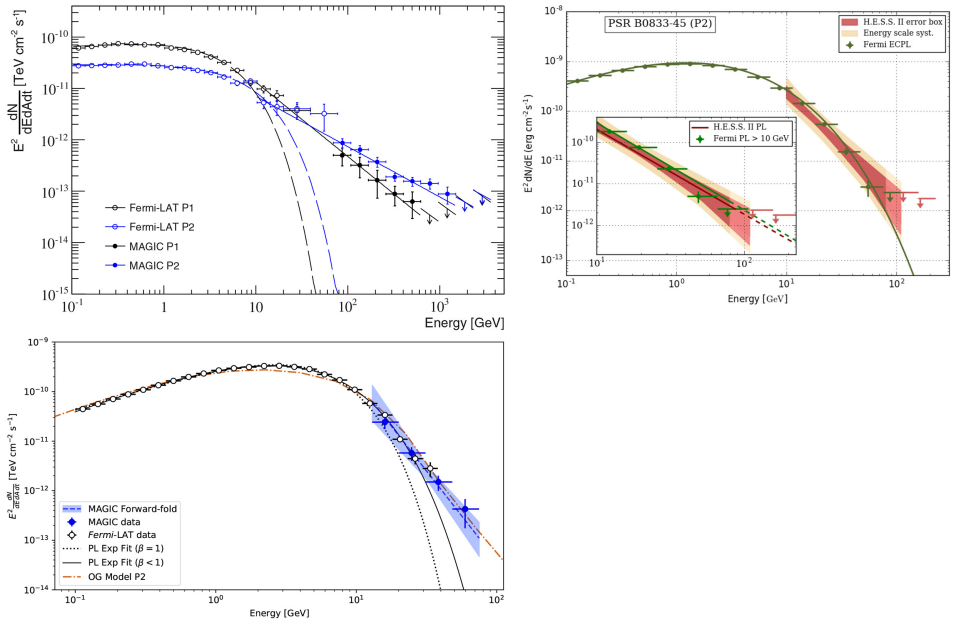

Figure 7.14. Top left: pulsed gamma-ray spectrum (peaks P1 and P2) from the Crab Pulsar with exponential cutoff fits as dashed lines. Image credit: Ansoldi et al. (2016), reproduced with permission © ESO. Bottom left: pulsed gamma-ray spectrum (peak P2) from Geminga with exponential cutoff fits (replace $\beta = b$ in Equation (7.11)) and an outer gap model (OG model). Image credit: MAGIC Collaboration et al. (2020a), reproduced with permission © ESO. Top right: pulsed gamma-ray spectrum from the Vela Pulsar P2 peak with an exponential cutoff fit as the green line. Image credit: HESS Collaboration et al. (2018g), reproduced with permission © ESO.

the edge of the magnetosphere (e.g., Hirotani 2011, 2013; Harding & Kalapotharakos 2015), or from ultrarelativistic "cold" wind electrons extending out to the wind termination shock at the PWN boundary (e.g., Bogovalov & Aharonian 2000; Aharonian et al. 2012; Mochol & Petri 2015) has met with some success.

7.5.4 Gamma-Ray Binary Systems and Related Microquasars

Gamma-ray binaries are often considered a subset of the compact binary class in which one of the binary members is a compact object (white dwarf, neutron star, or black hole) and the other member is a "regular" star powered by fusion (low to high mass). In recent years, the discovery of gamma rays from a massive stellar binary stellar system (η-Car) has extended this definition further.

There are a number of ways in which gamma-ray emission may be produced. Accretion of stellar material toward the compact object, or the interaction of winds from the stellar and neutron star, can set up particle acceleration conditions leading to gamma rays and nonthermal radio to X-ray emission. Strong thermal X-ray emission is also generated by the same processes, giving rise to the terms high-mass X-ray binary (HMXB) and low-mass X-ray binary (LMXB) that have been used for decades.[3] Particle acceleration via rotation of the neutron star may also take place in a similar fashion to that found in pulsars. Additionally, the accretion and rotation processes can lead to the formation of collimated outflows or jets (sometimes reaching relativistic speeds) that can accelerate particles. The presence of jets in such systems has led to the term "microquasar" and "microblazar" in an analogous situation to their much larger extragalactic cousins (discussed in Section 7.6.1). The often highly eccentric orbits in such binary systems lead to particularly active particle acceleration around the periastron phase when the binary members' separation is minimized. Similarly, the rather random nature of accretion also leads to a highly variable and/or transient output, such as in the case of classical novae where gamma rays result from the thermonuclear detonation of accreting material onto a white dwarf.

Here, we will provide a broad overview of the GeV to TeV observations and the various source classes while the reader is referred to the following reviews for more details: Mirabel & Rodríguez (1999), Dubus (2013), Paredes & Bordas (2019), and Chernyakova & Malyshev (2020) (also see Section 6.5.3). At present, there are a total of 13 gamma-ray binaries detected in TeV gamma rays (TeVCat: catalog of tev gamma-ray sources, http://tevcat2.uchicago.edu/) and a similar number detected at GeV energies (Abdollahi et al. 2020).

We will first look at the gamma-ray binaries involving a suspected neutron star compact object and a massive star (OB or Be types), which represent the most numerous subclass. These are often termed high-mass gamma-ray binaries (HMGBs). A key point is that the gamma-ray emission can be modulated by the orbital period (typically months to decades) of the binary system due to orbital-dependent absorption and production. Gamma rays of energy >0.1 TeV (γ)

[3] Indeed, the first extrasolar X-ray source discovered, Sco X-1, is a low-mass X-ray binary.

produced near the neutron star can readily interact with lower-energy optical/UV photons ($\gamma_{\mathrm{Opt-UV}}$) from the massive stellar companion and create electron/positron pairs ($\gamma\ \gamma_{\mathrm{Opt-UV}} \rightarrow e^{-}e^{+}$). This interaction is angle dependent, and the pairs then create lower-energy secondary GeV gamma rays in a cascade process. Additionally, IC scattering by electrons to produce the gamma rays (IC by electrons is usually the proposed mechanism given the presence of nonthermal X-ray and radio emission) is highly anisotropic, giving rise to an orbital dependence in the gamma-ray production. Finally, the underlying particle acceleration and hence gamma-ray emission production are strongly linked to the separation of the binary companion and usually maximizes around the periastron phase of closest separation. Putting all of these effects together leads to a quite complex orbital modulation of the GeV to TeV gamma-ray emission. On the other hand, this modulation has enabled the discovery of new HMGBs using gamma rays (e.g., Corbet et al. 2019) and unique investigations into the properties of the binary companions. Here, we will look at some examples.

The first HMGB detected was the LS 5039 system, which has a 3.9 day orbital period (Aharonian et al. 2005b, 2006e). A clear spectral difference was seen for the orbital phase at inferior conjunction (O star behind the neutron star) versus superior conjunction (O star in front of the neutron star). The situation is illustrated in Figure 7.15. The superior conjunction phase creates the maximum pair absorption in the 0.1 to 1 TeV gamma-ray band, and the periastron phase is slightly offset from superior conjunction. Another example is the recently discovered HMGB linked to PSR J2032+4127 (Abeysekara et al. 2018b; ~50 year period), and its X-ray and TeV gamma-ray light curves (versus orbital phase) are shown in Figure 7.15.

Interestingly, PSR J2032+4127 is located at the edge of the unidentified TeV source TeV J2032+4130, which exhibits weak, extended emission and is thought to be associated with the massive stellar cluster Cyg OB2 (Aharonian et al. 2002, 2005a). The peak emission from PSR J2032+4127 during the previous periastron phase in 2017 was about 10 times larger than the extended emission from TeV J2032 +4130. PSR J2032+4127 and PSR B1259–63/LS 2883 are only HMGBs where the compact object is confirmed as a neutron star due to their pulsar nature. We note though that the compact object in LS 5039 was recently suggested to be a magnetar (Yoneda et al. 2020).

Another binary class detected is the enigmatic stellar binary system η Car (Humphreys & Martin 2012), comprising two massive companions in a 5.52 year orbit. One of the companions is a luminous blue variable (LBV) of ~100 $M_{\odot}$ exhibiting extreme mass loss via its winds. The MeV to GeV gamma-ray emission detected by Fermi-LAT has been detected around the full orbit but the 10 to 300 GeV emission most noticeably peaked around the previous periastron phase (early 2015; Farnier et al. 2011; Reitberger et al. 2015). Just recently, HESS detected TeV gamma-ray emission of up to 0.5 TeV (HESS Collaboration et al. 2020c) in observations concentrated around the previous periastron. The gamma-ray emission is generally believed to come from particles shock-accelerated at the wind-collision region. The hadronic process has been somewhat favored (HESS Collaboration

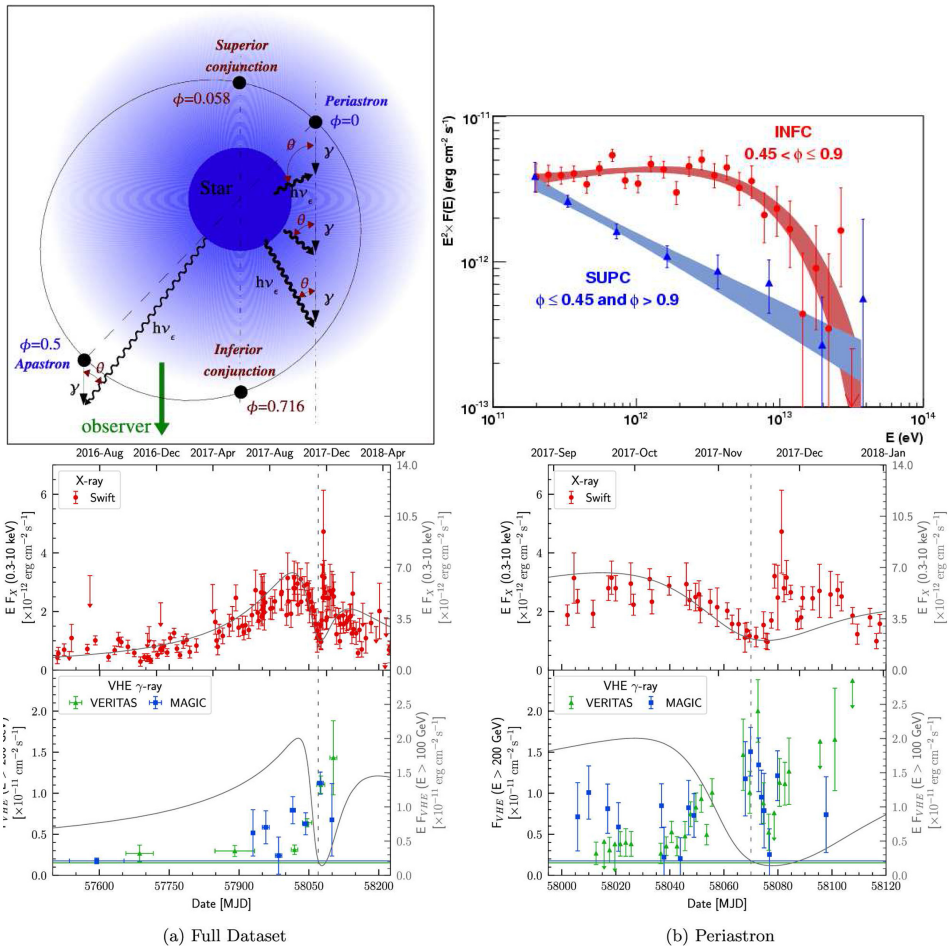

Figure 7.15. Top panels: LS 5039 binary-viewing situation versus orbital phase ϕ (neutron star is the black dot) and gamma-ray spectra for the inferior conjunction (INFC) and superior conjunction (SUPC) phases (Images from Aharonian et al. 2006e, reproduced with permission © ESO). Bottom: X-ray and TeV gamma-ray light curves versus orbital phase for PSR J2032+4127 with periastron as the vertical dashed line. The solid line is a model expectation. Image credit: Abeysekara et al. (2018b).

et al. 2020c) for the multi-GeV to TeV emission due to the intense synchrotron and IC losses electrons might suffer in the wind-collision zone that would prevent them from reaching sufficiently high energies.

The microquasar SS 433 has for decades attracted attention as one of the most powerful objects in our Galaxy (Margon 1984). Its bilobal jets reaching speeds of about $0.3c$ extending for about a degree on either side of the central object (likely a Wolf–Rayet (WR) star accreting onto a black hole in a 13 day orbit) require up to 10^{41} erg s^{-1} to sustain. The jets exhibit several lobes or knots seen mostly in X-rays (Safi-Harb & Ögelman 1997), and also, they are the only jets with evidence for a

baryonic flow (Migliari et al. 2002), making them an ideal laboratory to study extreme cosmic-ray "beam dumps." SS 433 is embedded within the biconical-shaped SNR W50 (Dubner et al. 1998). Extended gamma-ray emission at about 1 GeV was first detected by Bordas et al. (2015), which broadly centered on SS 433 and W50, but the weak signal and resolution of Fermi-LAT prevented firm conclusions as to its origin. The HAWC telescope then discovered two multi-TeV gamma-ray sources at about 25 TeV energy overlapping the inner X-ray knots (Abeysekara et al. 2018c) as shown in Figure 7.16.

A leptonic scenario was favored by Abeysekara et al. (2018c) to explain the TeV emission and suggested electrons are locally accelerated at the knots where the TeV emission is seen. Following the TeV detection by HAWC, Sun et al. (2019) provided an improved Fermi-LAT image of SS 433 in GeV gamma rays, indicating an extension similar to the W50 SNR but centered on the central SS 433 source. The GeV emission is possibly related to the W50 SNR rather than to SS 433.

Additional GeV sources were recently reported by Li et al. (2020a), with one of them reported to show modulation at the ~160 day precessional period of the SS 433 system. However, this has been questioned by Bordas (2020), who notes that modulation would be very unlikely to be maintained over the >30 pc distance to this source from the central system. Overall, the HAWC and Fermi-LAT detections

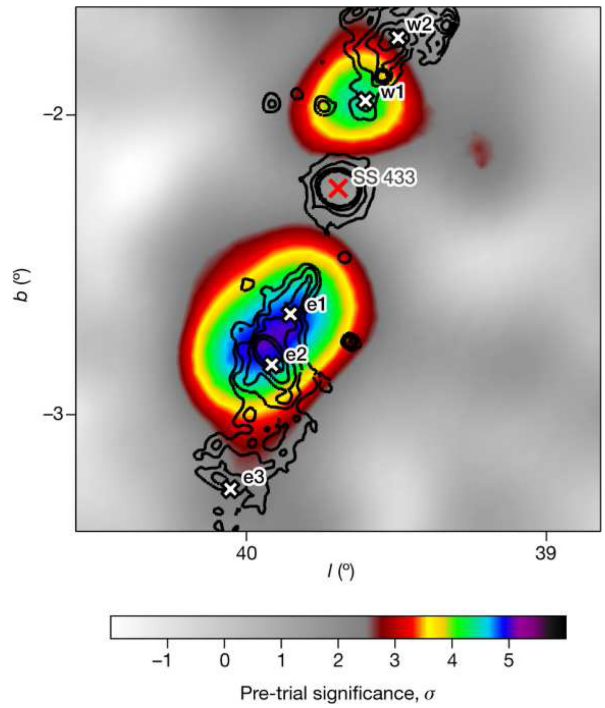

Figure 7.16. HAWC TeV gamma-ray image of SS 433 with X-ray contours (black solid) and knots from Safi-Harb & Ögelman (1997) labeled. Image credit: Abeysekara et al. (2018c), with permission of Springer.

have sparked renewed theoretical activity devoted to extreme particle acceleration in microquasar jets leading to both leptonic and hadronic gamma-ray emission. We will discuss some of these in the context of PeVatrons (Section 7.5.6), but we recommend the recent review devoted to particle acceleration in astrophysical jets (Matthews et al. 2020), which is also relevant to our discussion on AGN (Section 7.6.1).

GeV gamma-ray emission associated with microquasar jets has been detected in three other objects, Cyg X-3, Cyg X-1, and V404 Cygni (Fermi-LAT Collaboration et al. 2009; Tavani et al. 2009; Sabatini et al. 2010; Bodaghee et al. 2013; Malyshev et al. 2013; Zdziarski et al. 2017; Xing 2006). The first three are HMXBs while notably, V404 Cygni is an LMXB (1 $M_{\odot}$ companion). To date, several flares from Cyg X-1 and Cyg X-3 have been detected by Fermi-LAT and/or AGILE. Hints of TeV gamma-ray emission coinciding with an X-ray flare from Cyg X-1 was also reported by MAGIC (Albert et al. 2007) in 2006, but not coinciding with any of the GeV flares and so far not repeated.

We will conclude our discussion of gamma-ray binaries with a brief look at novae that Fermi-LAT has now established as a class of gamma-ray sources. To date, 12 novae are seen in GeV gamma rays (e.g., Xing 2006; Ackermann et al. 2014; Cheung et al. 2016; Li et al. 2020b), all of which were identified by their optical flaring. The gamma-ray flaring episodes can last up ~20 days (usually just after the initial optical flare) with luminosities of 10^{34-36} erg s^{-1} reaching up to ~10 GeV in energy. So-called "classical" novae are powered accretion of material from a donor star onto a white dwarf (WD) compact binary companion. Blobs of accreting material can detonate in a thermonuclear explosion. The gamma-ray emission suggests that this process can create the conditions for particle acceleration to near-TeV energies, and both leptonic and hadronic processes can explain the emission with the latter generally expected given the high density environment within the nova ejecta. Most of the gamma-ray novae are of the classical type, whereas V404 Cyg as a symbiotic system and the gamma-ray emission are thought to be due to interactions of the nova ejecta with the red giant donor star wind. A recent review of this developing source class can be found in Chomiuk et al. (2020).

7.5.5 Other Galactic Sources

In this section we will review the other types of Galactic sources that are established gamma-ray emitters.

Massive Stars and Their Stellar Clusters: The enormous energy liberated by massive stars (up to 10^{39} erg s^{-1}) in O-type wind kinetic energy and subsequently in their clusters has for many years made them ideal places to accelerate particles (Casse & Paul 1980; Voelk & Forman 1982; Cesarsky & Montmerle 1983). Additionally, the longevity of massive stars (10^{6-7} yr) could mean that their cluster may make significant contributions to the Galactic cosmic-ray flux (e.g., Aharonian et al. 2019). Several massive stellar clusters detected in GeV to TeV gamma rays—NGC 3603, Westerlund 1, Westerlund 2, W43 (HESS J1848−018), and Cyg OB2 (HESS Collaboration et al. 2011; Abramowski et al. 2012; HESS Collaboration

et al. 2018a; Yang & Aharonian 2017; Yang et al. 2018; Aharonian et al. 2002, 2005a)—are the most confident associations so far based on the extended nature of the gamma-ray emission, its spectrum, and in some cases, a lack of any obvious alternative accelerators such as SNRs or sufficiently powerful pulsars. Recently, another cluster, RSGC1, was linked to GeV gamma-ray emission (Sun et al. 2020).

These clusters can be considered somewhat extreme in certain aspects of their nature, such as a very large number of O and B stars (NGC 3603, Cyg OB2); over 20 WR stars (Westerlund1); a combination of many O, B, and WR stars; a large number of red supergiant stars (RSGC1); and a "mini" starburst of massive star birth (W43). Another interesting example is C11806−20, where marginally extended TeV emission has been detected (HESS Collaboration et al. 2018f). This cluster harbors the magnetar SGR 1806−20 and the LBV star LBV 1806−20, which is one of the most-luminous stars in our Galaxy. The TeV emission extension may follow a similar morphology to the radio nebula powered by LBV 1806−20, thus hinting that this single star may play a prominent role in the multi-TeV particle acceleration. Cyg OB2 is also rather special for its tight concentration of 50 to 100 O-type stars, several WR stars, and the LBV Cyg OB2#12, making it one of the most powerful sources of stellar winds known. Just recently, the gamma-ray binary PSR J2032+4127 at the edge of Cyg OB2 was detected as a point-like source Abeysekara et al. (2018b), as discussed earlier. It is however resolved in TeV gamma rays from the extended gamma-ray emission overlapping Cyg OB2, and thus, this cluster remains a viable counterpart.

Superbubbles: Following on from the previous discussion on stellar clusters, superbubbles are blown out by the collective winds of massive stellar clusters (the more mature and sparse versions usually known as OB associations) and SNRs over a typical 10^{5-7} year timeframe. Their outer boundaries contain large-scale shocks of over 100 pc in diameter, giving rise to some the largest shock structures in our Galaxy. As a result, they have long-been proposed as particle accelerators (Montmerle 1979; Cesarsky & Montmerle 1983; Bykov & Toptygin 2001; Parizot et al. 2004) to extreme energies. To date there have been two gamma-ray detections that are associated with superbubbles: the Cygnus superbubble (Ackermann et al. 2011; Bartoli et al. 2014) and 30Doc C in the LMC (HESS Collaboration et al. 2015). There is also speculation that the very extended TeV emission (2° diameter) around the extreme cluster Westerlund1 (Abramowski et al. 2012) could also be related to a superbubble process.

The GeV gamma-ray emission in the Cygnus superbubble appears to overlap somewhat and thread in between the massive stellar clusters Cyg OB2, NGC 6910, and the other star-forming regions in a kind of cocoon-like emission. This is attributed to multi-TeV cosmic rays accelerated by the clusters, which then fill in the cavities the clusters have carved out. Additional acceleration may also come from the local SNR γ Cygni. Extended TeV gamma-ray emission seen by the ARGO-YBJ telescope (Bartoli et al. 2014) has a similar morphology to that of the GeV emission and is considered to be the TeV counterpart. Including the MILAGRO source MGRO J2031+41 (Abdo et al. 2007a), which is thought to be related, the energy spectrum extends to >20 TeV.

The 30 Dor C is a superbubble in the LMC and is one of most luminous massive star formation regions known with nonthermal X-ray emission along parts of its rim. This X-ray rim emission is considerably more luminous and larger in size than that typically found in Galactic SNRs. The TeV emission (HESS Collaboration et al. 2015) found by HESS is positioned toward a massive star cluster toward the northwest region of the bubble and overlaps molecular gas (Sano et al. 2017), although the HESS angular resolution prevents a detailed morphological study. A hadronic process for the TeV emission may be at work, suggesting cosmic rays above 100 TeV in energy although a leptonic process is also not ruled out. Recent X-ray observations confirm the presence of nonthermal X-ray emission to >20 keV in energy, and hence electron acceleration to over 100 TeV energies around parts of the superbubble rim (Lopez et al. 2020).

Galactic Center Region and Diffuse Emission: Following the first hints for TeV gamma rays from the Galactic Center region by Kosack et al. (2004), the gamma-ray emission over the inner 500 pc of our Galaxy has now been separated into diffuse and local components (made possible by the 5′ to 6′ resolution at TeV energies). The local components are attributed to the central source Sgr A* (Acero et al. 2010), the composite SNR G0.9+0.1 (Aharonian et al. 2005b), and the PWN G0.13−0.11 (Archer et al. 2016; HESS Collaboration et al. 2018e). The diffuse components comprise the inner 70 pc surrounding Sgr A*, which requires a central PeVatron cosmic-ray accelerator (discussed in Section 7.5.6), and the larger-scale component extending for a few hundred parsecs along the Galactic Plane (Aharonian et al. 2006a; Archer et al. 2016; Ahnen et al. 2017; HESS Collaboration et al. 2018e; MAGIC Collaboration et al. 2020b).

The TeV emission toward Sgr A* appears to be related to our Galaxy's central black hole region although the nearby PWN G359.95−0.04 cannot yet be ruled out as a contribution (Acero et al. 2010). So far, the Sgr A* TeV emission has shown no indication for variability (including during a 2017 pericenter passage of a large molecular cloud), in contrast to the situation in X-rays where a number of flares have been seen over the decades (see Ahnen et al. 2017 and references therein). Immediately upon its discovery by HESS (Aharonian et al. 2006a), the diffuse TeV component overlapping the Galactic "Ridge" showed clear indications for an overlap with the dense interstellar gas (see Figure 7.17), providing the first evidence for multi-TeV cosmic rays within the central few hundred parsecs of the Galactic Center region.

This region hosts a large fraction of our Galaxy's interstellar gas (with over 10^6 $M_\odot$ in mass present) and a number of potential cosmic-ray accelerators nearby besides the central black hole. In 2018, HESS showed that the inner 70 pc of the TeV emission surrounding Sgr A* does not have any indication for a high-energy cutoff in its spectrum, suggesting the presence of cosmic rays reaching PeV energies (HESS Collaboration et al. 2016). When comparing the spatial profile of this TeV emission with that of the dense gas, the inferred cosmic-ray density follows a 1/radius dependence, indicating a quasi-continuous accelerator operating for at least 1000 years. This seems to point toward the central black-hole-powered region as the

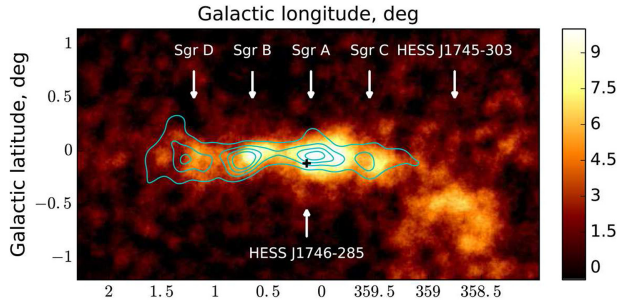

Figure 7.17. TeV gamma-ray emission from the Galactic Center region as detected by HESS The cyan contours depict the dense molecular gas traced by the CS(1–0) transition (HESS Collaboration et al. 2018e) and various other features (identified in radio to X-rays) are labeled. Image from HESS Collaboration et al. (2018f), reproduced with permission © ESO.

accelerator, and moreover, the energy available in the central accelerator (if operating sporadically over the past 10^6 years) could account for a good fraction of the total PeV cosmic rays in our Galaxy. Alternative accelerator scenarios for this PeVatron region and wide diffuse emission have been discussed: millisecond pulsars (Guépin et al. 2018), a combination of millisecond pulsars and dark-matter (Lacroix et al. 2016), and cosmic rays escaping SNRs (Jouvin et al. 2020).

Looking out to wider scales, the diffuse MeV to GeV gamma-ray emission along the Galactic Plane is now a ubiquitous feature (Ackermann et al. 2012) since being revealed in the early days of space-based gamma-ray astronomy (Fichtel et al. 1975). This diffuse emission arises from the long-term resident or "sea" of cosmic rays and electrons pervading the Galaxy. These have long since moved away (via diffusion or otherwise) from their acceleration sites. The broad distribution of the diffuse gamma-ray emission matches that of the Galactic latitude, and the longitude distribution of SNRs, pulsars, massive star clusters, and the interstellar molecular gas provides some clues as to where these particles come from (the IC component from electrons is expected to be somewhat broader, reflecting the distribution of soft infrared photon targets). The only direct measurements of this sea of particles are via satellites in Earth orbit and out to the Voyager probes at the heliopause and just beyond where they have sampled MeV interstellar cosmic rays without solar wind influences for the first time (Stone et al. 2013, 2019).

Measuring the in situ cosmic-ray and electron sea across the Galaxy requires an understanding of secondary by-products such as gamma rays, and detailed models and specific observation strategies have been developed over the years for this purpose. The GALPROP model (Strong & Moskalenko 1998) has been used a basis to estimate the diffuse MeV to GeV gamma-ray background in order to identify MeV to GeV sources in Fermi-LAT data (Abdollahi et al. 2020). Recent updates to GALPROP (Porter et al. 2017; Jóhannesson et al. 2018) set up a 3D distribution of accelerators (e.g., SNRs and pulsars) and follow the trajectories of cosmic rays and electrons via a transport equation (e.g., see Strong & Moskalenko 1998) interacting with the interstellar gas 3D gas distribution (CO and H I for molecular and atomic gas) and radiation fields (infrared and optical) to produce gamma rays via the three

main processes (pp collisions, bremsstrahlung, and IC; synchrotron emission is also calculated). Other models (Kissmann et al. 2015; Evoli et al. 2017) with 3D geometry in various aspects are also advancing (see Becker Tjus & Merten 2020 for a detailed review of various codes). A key driver of these models is the improving sensitivity of TeV gamma-ray facilities (e.g., CTA), which will reach arcminute resolution, demanding more precise 3D grids over which to solve particle transport and interaction.

At TeV energies, the rapid cooling times of electrons in particular mean that the diffuse gamma-ray emission could be quite sporadic and vary considerably for 10^{3-4} years after local acceleration events like SNRs. The most recent enhancements to GALPROP (Porter et al. 2019) have been motivated by this issue. Some indirect observations of the GeV to TeV cosmic-ray sea have come from looking at the Fermi-LAT MeV to GeV gamma-ray emission from passive individual giant molecular clouds that are believed to be not too close to recent accelerators like SNRs and young pulsars. Both Aharonian et al. (2020) and Baghmanyan et al. (2020) recently exploited this idea, which was proposed some time ago (Aharonian 2001; Casanova et al. 2010), and they found cosmic-ray densities up to twice the Earth-like value for clouds in the 4 to 6 kpc galactocentric distance range and for some very nearby clouds (<500 pc from Earth).

The TeV gamma-ray diffuse emission has so far proven to be more difficult to measure. However, evidence for the TeV Galactic Plane diffuse emission has been reported by Abdo et al. (2008), Abramowski et al. (2014a) and Bartoli et al. (2015). The fraction of unresolved sources has been a key uncertainty as to whether this large-scale TeV emission detected so far is from truly diffuse particles or from those accelerated not far from their accelerators as unresolved sources. Some recent estimates (Steppa & Egberts 2020; Cataldo et al. 2020) suggest this fraction could be up to 60%. As further evidence of this diffuse or unresolved source emission, in the analysis of its Galactic Plane data (HESS Collaboration et al. 2018a), HESS had to implement an ad hoc large-scale diffuse component in order to successfully model the complete TeV Galactic Plane emission observed by HESS.

No discussion of diffuse gamma-ray emission would be complete without mentioning the Fermi Bubbles, the multidegree GeV gamma-ray features extending above and below the Galactic Plane (discovered by Su et al. 2010). Their discovery had an immediate impact on the view of our Galaxy's history. There are currently two schools of thought hotly debated as to their origin, based also on prior bubble-like or wisp features seen from radio to X-rays: (1) prior AGN activity driven by our Galaxy's supermassive black hole (e.g., Zubovas et al. 2011; Guo & Mathews 2012; Mou et al. 2014; Bland-Hawthorn et al. 2019; Zhang et al. 2020) or (2) starburst activity driven by the winds and death of massive stars in the inner few hundred parsecs of our Galaxy (e.g., Crocker & Aharonian 2011; Lacki 2014; Crocker et al. 2015). In addition, a fundamental question still surrounds the nature of the underlying particles (cosmic rays and/or electrons) generating the Fermi Bubble emission, with both types of models being put forward (e.g., Crocker & Aharonian 2011; Herold & Malyshev 2019). In any case, the bubbles require a considerable

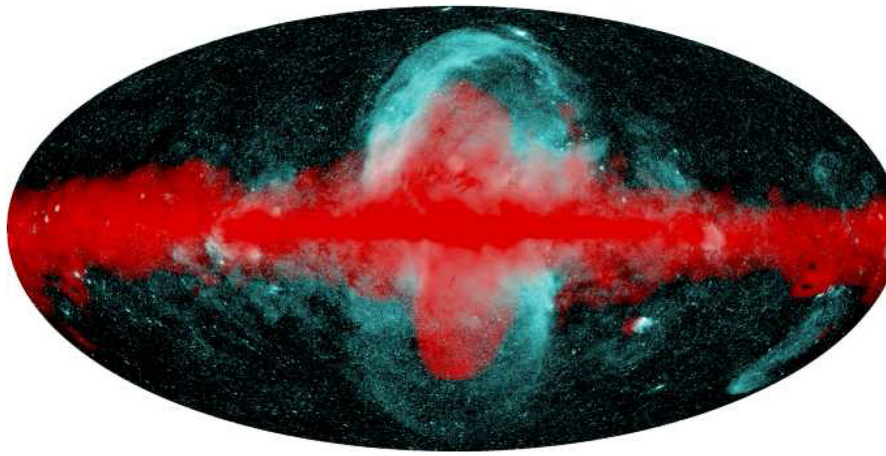

Figure 7.18. eROSITA 0.6–1 keV X-ray emission (cyan) versus Fermi-LAT GeV gamma-ray emission (red) revealing new X-ray bubbles wrapping around the Fermi GeV bubbles. Image credit: Predehl et al. (2020), with permission of Springer.

amount of energy to be injected ($\sim 10^{55}$ erg). The most recent new result in relation to the bubbles was the discovery of soft X-ray emission by eROSITA (Predehl et al. 2020) appearing to wrap around the northern and southern gamma-ray bubbles as shown in Figure 7.18 (this also clearly shows the diffuse gamma-ray emission along the Galactic Plane).

The X-ray emission shows a clear outer boundary, and its total energy is about 10× larger than that in the GeV gamma rays. Current speculation (Predehl et al. 2020) is that the X-rays are revealing a forward shock (through the halo gas of the Milky Way) driven by the Fermi Bubbles, which themselves are driven by energy from the Galactic Center region.

Globular Clusters: Globular clusters are a rapidly growing population of GeV gamma-ray sources with 30 examples now identified (Abdollahi et al. 2020), following on from earlier discoveries (Kong et al. 2010; Abdo et al. 2010e). Only one globular cluster, Terzan5, is detected at TeV gamma-ray energies (HESS Collaboration et al. 2011), and interestingly, the TeV emission appears slightly displaced from the optical center of the cluster. Although dark matter scenarios have been discussed, the gamma-ray emission is most likely attributed to the large population of millisecond pulsars present in globular clusters (and possibly related to XRB emission).

Unidentified Sources: As discussed earlier, the unidentified gamma-ray sources represent typically 30% of the GeV and TeV source population and have been a major area of interest since the first catalogs were released (e.g., Reimer 2001). Today, a majority of the unidentified extragalactic GeV sources detected by Fermi-LAT are thought to be AGN blazars of an unknown class based on their point-like nature, variability, application of machine-learning techniques, and

newly found radio to optical counterparts (e.g., Acero et al. 2013; Doert & Errando 2014; Chiaro et al. 2016; Einecke 2016; Schinzel et al. 2017; Mandarakas et al. 2019). We will leave further discussion of these sources to Section 7.6.1.

The unidentified Galactic gamma-ray sources have, however, presented a much greater challenge. This is due to their extended nature and hence potential to be confused with many potential counterparts along the line of sight plus the ability of single particle accelerators to generate rather specific extended gamma-ray features due to particle transport and interact with the unique interstellar gas situation surrounding them. Additionally, a growing number of unidentified Galactic gamma-ray sources from the COS-B and EGRET missions (Bignami & Hermsen 1983; Hartman et al. 1999); Gehrels et al. 2000) at MeV to GeV energies came with rather large positional uncertainties (degrees or so), complicating counterpart searches. Despite this, the obvious potential connections to SNRs (plus massive star clusters and pulsars) and their surrounding interstellar gas have been noticed for quite some time (Montmerle 1979; Esposito et al. 1996; Romero et al. 1999; Torres et al. 2003).

With Fermi-LAT's angular resolution improving with energy, for example ~0.1° above 10 GeV, Galactic sources detected at much higher energies (Ajello et al. 2017) have much better localization when compared to results using lower-energy analyses. Moreover, many of them can be cross-referenced against the growing number of TeV gamma-ray sources cataloged at similar or better resolution (HESS Collaboration et al. 2018a). The number of unidentified TeV gamma-ray sources has grown steadily (Aharonian et al. 2008a, 2006b; HESS Collaboration et al. 2018a) since the first one, TeV J2032+4130, was discovered in 2002 (Aharonian et al. 2002, 2005a). This source has proved particularly enigmatic and has been linked to the extreme stellar cluster Cyg OB2 although the leptonic and/or hadronic nature of the gamma-ray emission is yet to be firmly established (as for the majority of the Galactic TeV sources). As discussed earlier, this source has an additional component associated with a high-powered pulsar in a binary system (Abeysekara et al. 2018b).

Following the first HESS surveys, many of the unidentified TeV sources appeared not far away from mature SNRs or moderate-power pulsars. A related interpretation was built around these ideas (e.g., de Jager et al. 2009; Yamazaki et al. 2006; Chang et al. 2008; Aharonian et al. 2008b), especially as it was becoming clearer that SNRs with escaping (or runaway) cosmic rays interacting with adjacent or more distant interstellar gas could lead to detectable emission. In more recent times, links to old-pulsar-powered TeV halos have been proposed (Sudoh et al. 2019), as the gamma-ray halo concept has become more widely understood. As a result, the interstellar gas, deeper X-ray observations, and new radio continuum surveys have hence gathered more attention as a way to help identify these TeV sources (e.g., Horns et al. 2007; Matsumoto et al. 2008; Eger et al. 2011; Voisin et al. 2016; Lau et al. 2017b; de Wilt et al. 2017; Lau et al. 2017a, 2019; Maxted et al. 2019; MAGIC Collaboration et al. 2020c; Feijen et al. 2020).

7.5.6 PeVatrons—Extreme Accelerators in the Milky Way

A special mention in this section of Galactic gamma-ray sources is devoted to the concept of accelerators known as PeVatrons, where particle acceleration is able to reach PeV energies or greater. This notion has held great mystery since the "knee" at PeV energies in the local cosmic-ray spectrum was first revealed over 50 years ago (Kulikov & Khristiansen 1958). The knee is suspected to be a signpost of the maximum limits of particle accelerators in our Galaxy (Peters 1961). The knee is a slight steepening of the cosmic-ray spectral index Γ (see Equation (7.1)), and its position in cosmic-ray energy increases proportionally to its charge. Thus, heavier elemental cosmic rays like iron reach energies a factor of 20 higher than proton cosmic rays (Figure 7.19), although the precise spectral limits of the higher-mass cosmic rays are not well known at these energies (Alves Batista et al. 2019). Well above the knee at about 10^{18} eV, the cosmic-ray spectrum flattens slightly in a feature usually called the "ankle." The ankle supposedly represents where the extragalactic cosmic-ray component starts to take over.

In a seminal paper, Hillas (1984) calculated the theoretical maximum energy $E_{\max}$ a charged particle can be diffusively shock-accelerated to by noting that the size of the accelerating shock should be at least twice the particle's Larmor radius (otherwise the particle will escape and no longer be accelerated):

$$E_{\max} \approx 10^{18} Z\beta RB \ \text{eV} \tag{7.12}$$

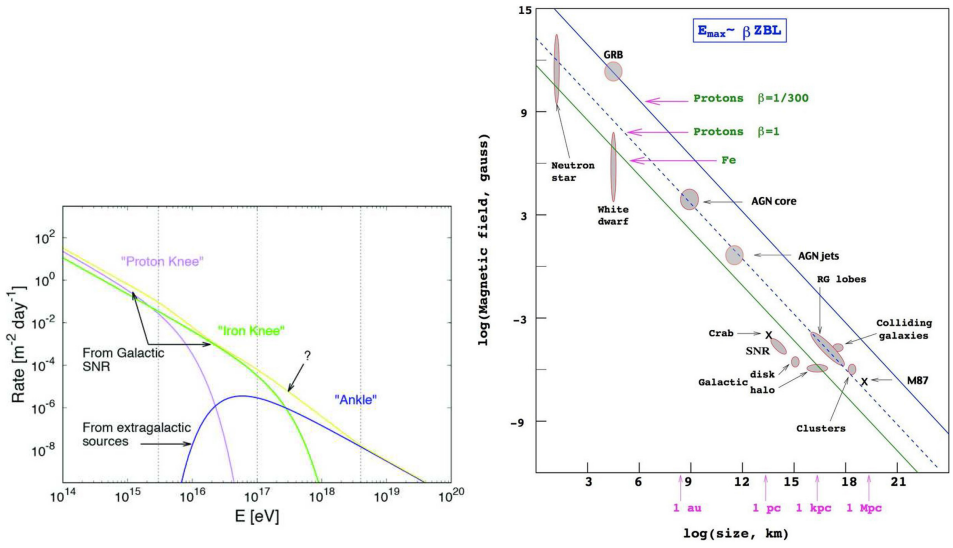

Figure 7.19. Left: cosmic-ray spectrum schematic showing the "knee" and "ankle" features, and the Galactic components from proton, iron, and extragalactic cosmic rays. The latter two are not observationally confirmed, hence the "?" above. Image credit: Alves Batista et al. (2019) with permission of Frontiers. Right: Hillas plot from Letessier-Selvon & Stanev (2011), Copyright 2011 by the American Physical Society, showing the maximum energy attainable by an accelerator with shock speed β, size (L in this figure), and magnetic field B.

for the particle charge Z, shock radius R in kiloparsec, magnetic field B in microgauss, and $\beta = v/c$ for the shock velocity v. With this, Hillas created his famous "Hillas plot," which has been reproduced many times (Figure 7.19 shows a version from Letessier-Selvon & Stanev 2011). It plots the locus of $E_{\max}$ points versus R and B for an assumed β and provided an immediate indication as to what types of objects could accelerate cosmic rays to various energies.

From Figure 7.19 and Equation (7.12), we can see that SNRs with size 1 pc and shock speed 10,000 km s^{-1} early in their evolution, when they are expected to provide their strongest acceleration, can in principle accelerate cosmic rays to 1 PeV provided their postshock magnetic field $B > 100\ \mu$G. Such a high magnetic field was a problem under the diffusive shock acceleration picture for quite some time (Lagage & Cesarsky 1983), until Bell (2004) showed that additional amplification is possible due to the effects of the cosmic rays themselves. Thus, at present, SNRs are considered potential PeVatrons. There are a number of other Galactic source types theoretically able to reach such energies. An incomplete list includes superbubbles (>100 pc scale shocks associated with massive stellar winds and many SNRs), massive stellar clusters, neutron star electric fields, magnetar flares, Galactic Center region, and microquasars.

An ideal way to search for PeVatrons is via the interstellar clouds around SNRs and through other accelerators (Gabici & Aharonian 2007). Here, the expected energy-dependent diffusion properties of cosmic rays toward the surrounding clouds can yield very specific gamma-ray spectra depending on the distance to the cloud and the age of the accelerator (i.e., how long ago did the cosmic-ray escape and then start to diffuse toward the cloud). An expectation is that the more distant clouds will pick up the highest-energy cosmic rays first and thus yield a very hard gamma-ray spectrum. A related scenario exploits the energy-dependent diffusion into dense interstellar gas clouds (Gabici et al. 2007). Here, due to the turbulence inside many dense clouds (especially those disrupted by star formation processes), the diffusion coefficient for low-energy particles will be suppressed. Thus, the penetration depth inside clouds could be shorter for low-energy cosmic rays (Inoue et al. 2012), reducing the gamma-ray emission at low energies, say <1 TeV, compared to that at higher energies. The dense clouds can then act a "reservoirs" of higher-energy cosmic-ray interactions.

Observationally, there are a number of hints for PeVatrons. First, the GeV synchrotron gamma rays detected from the Crab Nebula PWN is an unambiguous indicator of PeV electrons. The large scale of massive stellar clusters (and their long lifetimes as discussed earlier) may help them to accelerate particles to PeV energies, making them potential PeVatrons. The recent work by Aharonian et al. (2019) looked at the GeV emission toward Cyg OB2 and Westerlund 1 and found that a continuous injection of cosmic rays to PeV energies is a feasible interpretation.

The other more convincing cases for PeVatrons are the Galactic Center region surrounding the central black hole (HESS Collaboration et al. 2016), the TeV sources detected by HAWC with emission beyond 56 TeV and 100 TeV (Abeysekara et al. 2020), and diffuse emission along the Galactic Plane detected by the Tibet$AS\gamma$ array (Amenomori et al. 2021). The central black hole source has been discussed

earlier but we would note that the intrinsic cosmic-ray spectral cutoff energy of about 0.4 PeV as determined by the HESS Collaboration et al. (2016) could in fact be up to 2× higher due to the noticeable absorption of >10 TeV gamma rays on the interstellar infrared fields (Porter et al. 2018).

There are a number of TeV sources seen by HESS, MAGIC, and/or VERITAS exhibiting hard gamma-ray spectra or with little to no constraint on any exponential cutoff in their spectral shape (e.g., Abramowski et al. 2014b; HESS Collaboration et al. 2020b; and see HESS Collaboration et al. 2018a). Many of these have HAWC counterparts >56 TeV. Already, these have obviously been linked to PeVatrons with potential counterparts such as SNRs, e.g., HAWC J2227+610 and its association with SNR G106.3+2.7 (Albert et al. 2020c), and very recently, HAWC J1825−134 (Figure 7.20; Albert et al. 2021), which reaches gamma-ray energies of 200 TeV and is

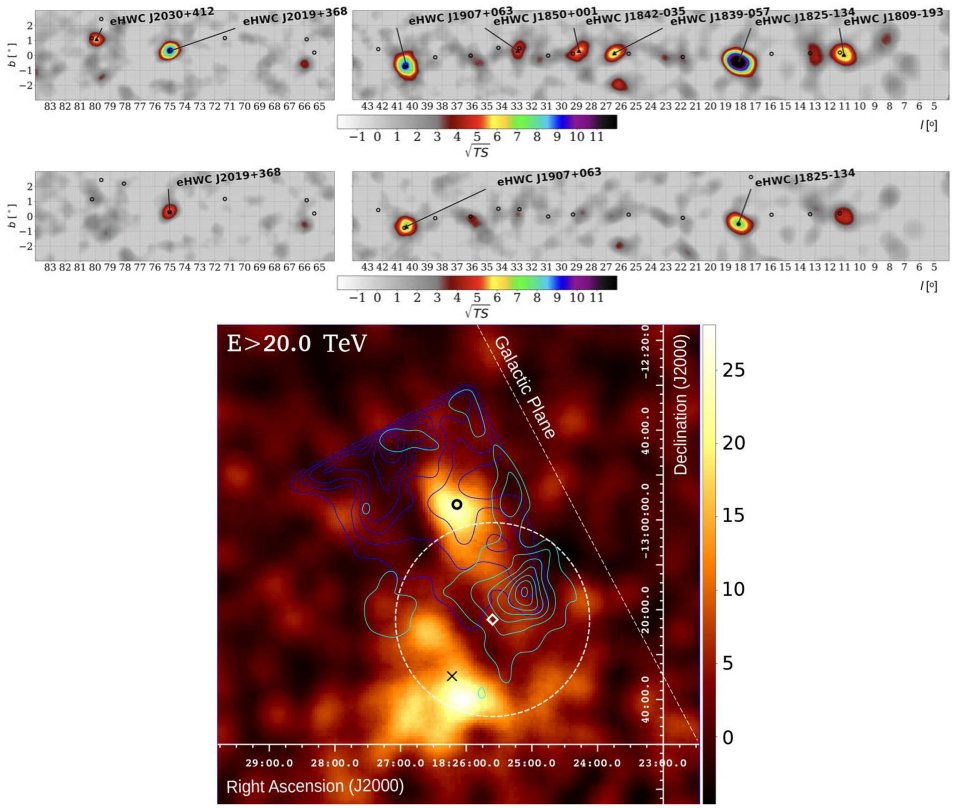

Figure 7.20. Top and middle: HAWC sky maps of statistical significance ($=\sqrt{TS}$) for energies >56 TeV (top) and >100 TeV (middle). Images from Abeysekara et al. (2020), Copyright 2020 by the American Physical Society. Bottom: HESS sky map toward HESS J185−137 and HESS J1826−130 for energies >20 TeV. Other objects are labeled as PSR J1826−1256 (black circle) and PSR J1826−1334 (black cross), eHWC J1825−134 >100 TeV (extension and location as white dashed circle and diamond from Abeysekara et al. 2020). The cyan and blue contours represent the total column density from the Nobeyama ^{12}CO(1–0) and SGPS H I surveys in the velocity ranges 45 to 60 km s^{-1} (4 kpc) and 60 to 80 km s^{-1} (4.6 kpc), respectively (see HESS Collaboration et al. 2020b for references). Image credit: HESS Collaboration et al. (2020b), reproduced with permission © ESO.

found in between the bright PWN HESS J1825−137 and the HESS PeVatron candidate source HESS J1826−130 (Figure 7.20). Interestingly, this highest-energy emission is very close to a dense molecular region associated with a young stellar cluster and star formation region in Voisin et al. (2016), suggesting a hadronic process is at work. If this is the case, it would certainly imply cosmic rays exceeding PeV energies.

We also note a recent discussion on the potential for microquasars to accelerate PeV cosmic rays (e.g., Cooper et al. 2020; Sudoh et al. 2020; Kimura et al. 2020) given the multi-TeV emission seen toward the jet lobes of SS 433 (Abeysekara et al. 2018c), and methods to identify PeVatrons via the spectral properties of unidentified TeV gamma-ray sources (Spengler 2020) and combinations of known SNRs and cataloged molecular clouds as potential targets for cosmic-ray collisions (Mitchell et al. 2021).

The IceCube neutrino detector, in combination with the Ice-Top array, is also sensitive to PeV gamma rays, and their most recent detections (Aartsen et al. 2020) have placed the tightest constraints so far on gamma rays in the 0.6 to 100PeV energy range. At the most extreme energies, $>10^{18}$ eV, gamma-ray flux constraints have been set by the Pierre Auger Observatory (Aab et al. 2017) and the Telescope Array (Abbasi et al. 2020).

Finally, we note the exciting discovery by the LHAASO facility (Cao et al. 2021) of a population of Galactic γ-rays with energies reaching at least 1 PeV. This result certainly opens the door to new insights into our galaxy's most extreme particle accelerators.

7.6 Extragalactic Gamma-Ray Sources

The extragalactic gamma-ray sources represent roughly half of the total population in both the GeV and TeV bands. Here, we will review the catalog of these sources and highlight some of the key results.

7.6.1 AGNs

The dominant extragalactic source class is the AGN of the "blazar" type, where an accretion-powered jet is directed toward Earth. The accretion is powered by a supermassive black hole of mass $>10^7$ $M_\odot$, which is believed to then form a perpendicular jet outflow that usually reaches relativistic speeds. Because the jet direction is toward Earth, strong Doppler effects that significantly boost the observed gamma-ray flux come into play. The observed flux usually attributed to a blob of material in the jet is boosted by a factor δ^4, where the Doppler factor δ is given by

$$\delta = [\Gamma(1 - \beta \cos\theta)]^{-1} \tag{7.13}$$

for the jet observation angle θ, Lorentz factor $\Gamma = (\sqrt{(}1 - \beta^2))^{-1}$, and $\beta = v/c$ for the jet speed v. Note that for head-on viewing ($\theta = 0$) we have $\delta \approx 2\Gamma$. The boosting factor δ^4 comes from three aspects (combining multiplicatively) resulting from special relativity, (1) the energy of each photon is boosted by a factor δ, (2) the effective contraction of time between successive photons means the photon rate is boosted by a factor δ, and (3) the jet angle is tightened such that the photon/solid-angle emitted is boosted by a factor δ^2. Over the past few decades, an AGN

unification picture has been developed (Antonucci 1993; Urry & Padovani 1995) to explain various observational properties according to the viewing orientation. Figure 1.7 shows a version (Reynolds et al. 2014) developed to include radio-quiet AGNs viewed from the side with a weak jet disrupted by the accretion disk, or, with no jet at all (see, e.g., Madejski & Sikora 2016; Padovani et al. 2017; Panessa et al. 2019).

Based on this, AGN classes such as Seyfert, radio-loud/-quiet quasars, blazars, radio galaxies (broad and narrow line) can be defined, although many of the details and class overlaps are still debated. An even broader label is the Fanaroff–Riley (FR) class (Fanaroff & Riley 1974) to distinguish radio-loud AGNs more centrally peaked (FRI class) from radio-loud AGNs with strong emission in jet lobes (FR II class), in cases where the jet and central region are separately visible.

The blazar AGN class itself has a number of subclasses originally based on their radio luminosities, in what is known as the blazar sequence (Fossati et al. 1998). A more recent version (Ghisellini 2016; Ghisellini et al. 2017) uses the third Fermi-LAT AGN catalog (Ackermann et al. 2015b) and predefined spectral components to group blazars according to their GeV gamma-ray luminosity, given the large number of examples detected (>1500) (the recently released fourth Fermi-LAT AGN has over 2800 examples). Figure 7.21 shows this sequence, illustrating the double-peaked nature of the blazar spectra spanning the radio, X-ray, and gamma-ray domains.

The first broad peak represents the radio to X-ray synchrotron emission, while the second peak covering the hard X-ray to gamma-ray band usually represents the IC process, so that the entire spectrum results from accelerated electrons. However, a bit later in this section, we will note that a hadronic process for at least parts of the gamma-ray emission has been put forward. A further broad classification separates blazars into BL Lacs (after the archetype BL Lacertae) and flat spectrum radio

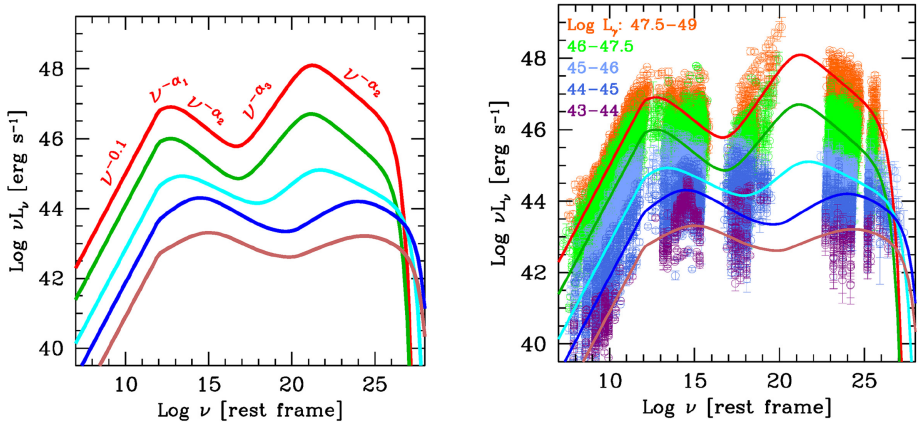

Figure 7.21. Updated version of the AGN blazar sequence based on their GeV gamma-ray luminosities (erg/s) shown as different color bands. The left panel shows the spectral components assumed and the right panel shows the average spectral shapes determined along with observed data. The top two curves represent FSRQs, and the bottom three curves represent BL Lacs (approximately LBL, IBL, HBL/EBL subtypes; cyan, blue, purple). Image credit: Ghisellini (2016), with permission of MDPI.

quasars (FSRQs) based on optical, radio, and variable properties and general spectral shapes. From the previous blazar sequence (Fossati et al. 1998), the labels low-frequency BL Lac, intermediate-frequency BL Lac, high-frequency BL Lac, and extreme-frequency BL Lac (LBL, IBL, HBL, and EBL) were coined according to the radio frequencies where their synchrotron component maximizes. The FSRQs display a relatively constant spectral shape but varying luminosities across whole spectra. In terms of the new blazar sequence by Ghisellini et al. (2017), the FSRQs are represented by the top two curves in Figure 7.21 (red and dark green), whereas the BL Lacs are represented by the bottom three curves (cyan—LBL, blue—IBL, purple—HBL/EBL). We note that the alternative names low-synchrotron-peaked blazar (LSP), intermediate-synchrotron-peaked blazar (ISP), and high-synchrotron-peaked blazar (HSP) have also been used (Ajello et al. 2020a).

At GeV energies, the latest Fermi-LAT catalog (Ajello et al. 2020a) reports 2863 AGN sources with 655 FSRQs (dominantly LBLs), 1067 BL Lacs (evenly split across LBL, IBL, and HBL), 1077 blazars of unknown type, and 64 nonblazar AGNs comprising 38 radio galaxies. At TeV energies (TeVCat: catalog of TeV gamma-ray sources, http://tevcat2.uchicago.edu/) 80 AGN sources are cataloged comprising 74 blazars, 4 radio galaxies, and 2 unknown types. Within the blazars, 63 are BL Lacs dominated by the HBL class (52 examples) and 8 are FSRQs. As expected, the HBLs are a prominent BL Lac class at TeV energies due to the higher-energy photons (and hence particles) being sampled.

The strong Doppler-boosting of the gamma-ray emission enables the detection of AGNs out to cosmological distances with redshift reaching $z = 4$ at GeV energies. Figure 7.22 illustrates the Fermi-LAT AGN blazar redshift distributions for AGNs in the FSRQ and BL Lac classes (Ajello et al. 2020a).

At TeV energies, AGN blazars are presently seen out to a redshift limit of $z \sim 1$ (TeVCat: catalog of TeV gamma-ray sources, http://tevcat2.uchicago.edu/). This limit is mostly due to the absorption of gamma rays on the extragalactic infrared photons, which can significantly reduce the gamma-ray flux for energies >1 TeV (a topic we will cover below). FSRQs dominate the TeV gamma-ray AGNs detected above redshifts $z = 0.5$. Nonblazar AGNs (often termed misaligned AGNs) where the jet does not point toward Earth, and hence the Doppler-boosting of the emission is weak or nonexistent, tend to be found much closer. At GeV energies they are mostly found within redshift $z < 0.2$ reaching up to $z \sim 1$, while at TeV energies the most distant example is at $z \sim 0.02$ (3C264; Archer et al. 2020). Within the AGN unification scheme outlined earlier, the FR I and FR II radio galaxy types are often considered the nonblazar versions of BL Lac and FSRQs blazars, respectively (e.g., Torresi 2020).

Among the nonblazars seen in gamma rays (see review by Sahakyan et al. 2018), the most prominent examples are Centaurus A (Cen A), M87 (Virgo A), and Fornax A. Importantly, the proximity and side-on view of these objects permit a probe of quite different particle acceleration/interaction regions and the potential to identify the host galaxy core from the jet. Indeed, extended gamma-ray emission detected from Cen A (GeV and TeV energies; Abdo et al. 2010b; HESS Collaboration et al. 2020a) and Fornax A (GeV energies only; Ackermann et al.

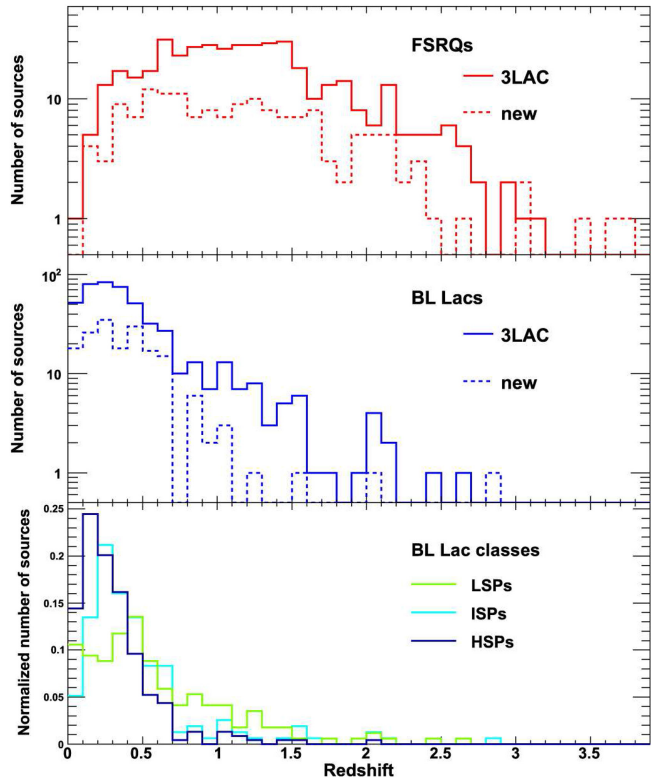

Figure 7.22. Redshift distribution of Fermi-LAT AGN blazars at GeV energies, separated into FSRQs and BL Lac types. Image credit: Ajello et al. (2020a).

2016) has permitted investigation into such issues. The extended emission tracks along the bilobal jets, and the most recent result for Cen A at TeV energies (HESS Collaboration et al. 2020a) from HESS is shown in Figure 7.23.

Here, we can see that the intrinsic source shape is highly elliptical aligned to the orientation of the jets (blue ellipse in Figure 7.23). Explaining this extension (along with similar features in X-rays and radio) appears to require electron acceleration along the jet up to at least 100 TeV in energy. Here, the electrons are responsible for the radio to X-ray synchrotron emission, and the IC emission at TeV gamma-ray energies (with the dominant upscattered photon field from infrared emission). Based on its spectral shape, the GeV gamma-ray emission detected by Fermi-LAT is likely dominated by the core of Cen A. For Fornax A, the GeV gamma-ray emission overlapping the jet lobes might be a combination of leptonic (IC) and hadronic (cosmic-ray and gas collisions) processes.

AGN Variability and Flaring: The nonsteady emission from AGNs is one of their most defining characteristics. The AGN blazars dominate the population of variable sources at gamma-ray energies although the FR II GeV gamma-ray fluxes are usually detected during high states in other wavebands (Torresi 2020). The variability and flaring episodes reflect the inherently stochastic nature of the

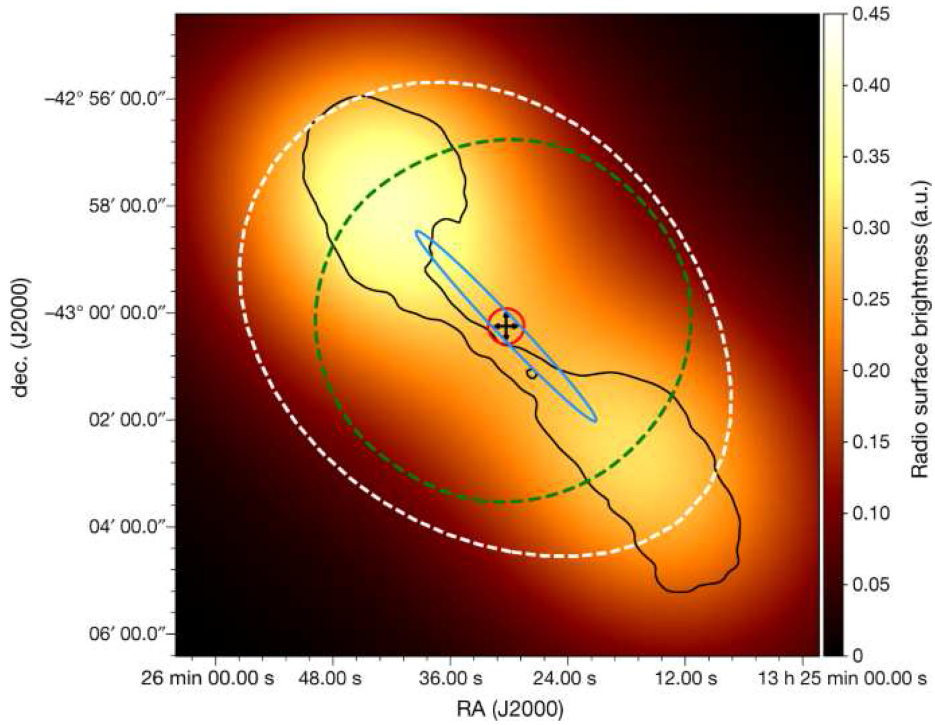

Figure 7.23. VLA 21 cm image of Centaurus A with contours in black (0.5 and 4 Jy beam^{-1}). The white dashed line indicates the TeV gamma-ray morphology convolved with the HESS point-spread function (green dashed circle). The blue-gray ellipse is the intrinsic shape (1σ level) of the TeV gamma-ray emission. The black arrows represent 1σ uncertainties on the TeV gamma-ray position and the red circle the systematic pointing uncertainly of HESS Image credit: HESS Collaboration et al. (2020a), with permission of Springer.

conditions leading to particle acceleration, and especially for blazars, the variability timescales are shortened by Doppler effects as discussed earlier. Variability down to minute timescales has been seen at TeV energies, and from causality arguments, such timescales $\Delta t_{\rm obs}$ can be used to constrain the physical size of the comoving (i.e., in the flow of the AGN jet presumably) source region $R'_{\rm src}$ emitting the photons such that

$$R'_{\rm src} \leqslant c\ \Delta t_{\rm obs}\ \delta = 10^{15}(\delta/10)(\Delta t_{\rm obs}/1\ {\rm h})\ \ {\rm cm}. \tag{7.14}$$

Figure 7.24 illustrates the radio to TeV gamma-ray SEDs for several AGN blazars in the HBL/EBL BL Lac class that show a range of variability across these energy bands.

Here, we can clearly see significant variability in the X-ray and gamma-ray bands for Mkn 501 and 1ES 1426+428 in contrast for the generally stable gamma-ray emission from 1ES 0229+200 (with mild changes in X-ray emission). The latter is part of the emerging class of extreme TeV blazars. The wide variety of variability for AGNs is further illustrated in Figure 7.25, which looks at a detailed

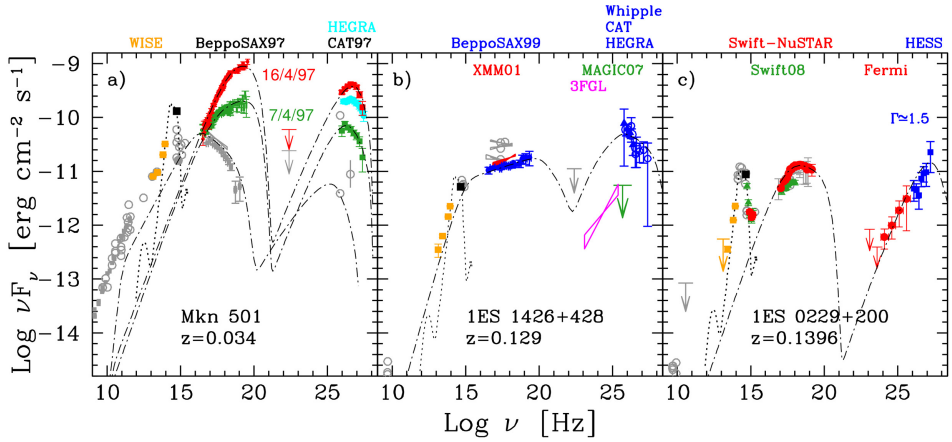

Figure 7.24. SEDs for several AGN blazars of the HBL/EBL BL Lac type. Contemporaneous data (1σ statistical errors; upper limits at 95% confidence level) are labeled with the same color, with gray indicating archival data. Dashed–dotted lines represent synchrotron self-Compton models, and dotted lines thermal emission from host galaxies. The gamma-ray data are corrected for extragalactic background light absorption. Image credit: Biteau et al. (2020), with permission of Springer.

multiwavelength study of two TeV flares from the IBL BL Lac S50716+714 ($z = 0.31$) (MAGIC Collaboration et al. 2018) during 2015.

From this figure we can see that the first TeV gamma-ray flare (phase A) is accompanied by activity in many other bands. However, a particularly noticeable feature is the dramatic change in the optical polarization position angle (formally, the electric vector position angle EVPA) accompanying the phase A TeV flare. This behavior may be attributed to a knot of material entering a shock region in the jet (with the phase B flare occurring later when the knot leaves the shock region). Such EVPA changes have been seen overlapping gamma-ray flares from other AGNs, thus optical polarimetry has gained in popularity as an important tool to help understand the complex high-energy physics occurring in AGN flares, along with regular monitoring and deep follow-up in the radio (e.g., TANAMI project Ojha et al. 2010; Müller et al. 2018) and in the X-ray bands (e.g., Wierzcholska & Wagner 2016).

Another significant flaring event was exhibited by TXS 0506+056 ($z = 0.336\,5$), a blazar of unknown type. The most notable aspect of this event was that the GeV and TeV gamma-ray flares seen by Fermi-LAT and MAGIC correlated in direction and time with an energetic neutrino detected by IceCube (IceCube Collaboration et al. 2018a, 2018b). Further analysis of the IceCube data revealed a burst of neutrinos from the same direction, hinting at an energetic event a few years prior, although this was not accompanied by any gamma-ray activity. The interpretation of this situation is led to much debate and further discussion can be found in Section 8.4.7.

Some of the strongest source constraints come from the two extraordinary flaring episodes in 2006 of the HBL BL Lac PKS 2155−304 ($z = 0.116$; Aharonian et al. 2007a, 2009). The first flare, on 2006 July 28, had a peak flux reaching about 15 Crab units, with luminosity $L_\gamma \sim 10^{12} L_{\rm Crab}$ in the TeV band. The most rapid variation

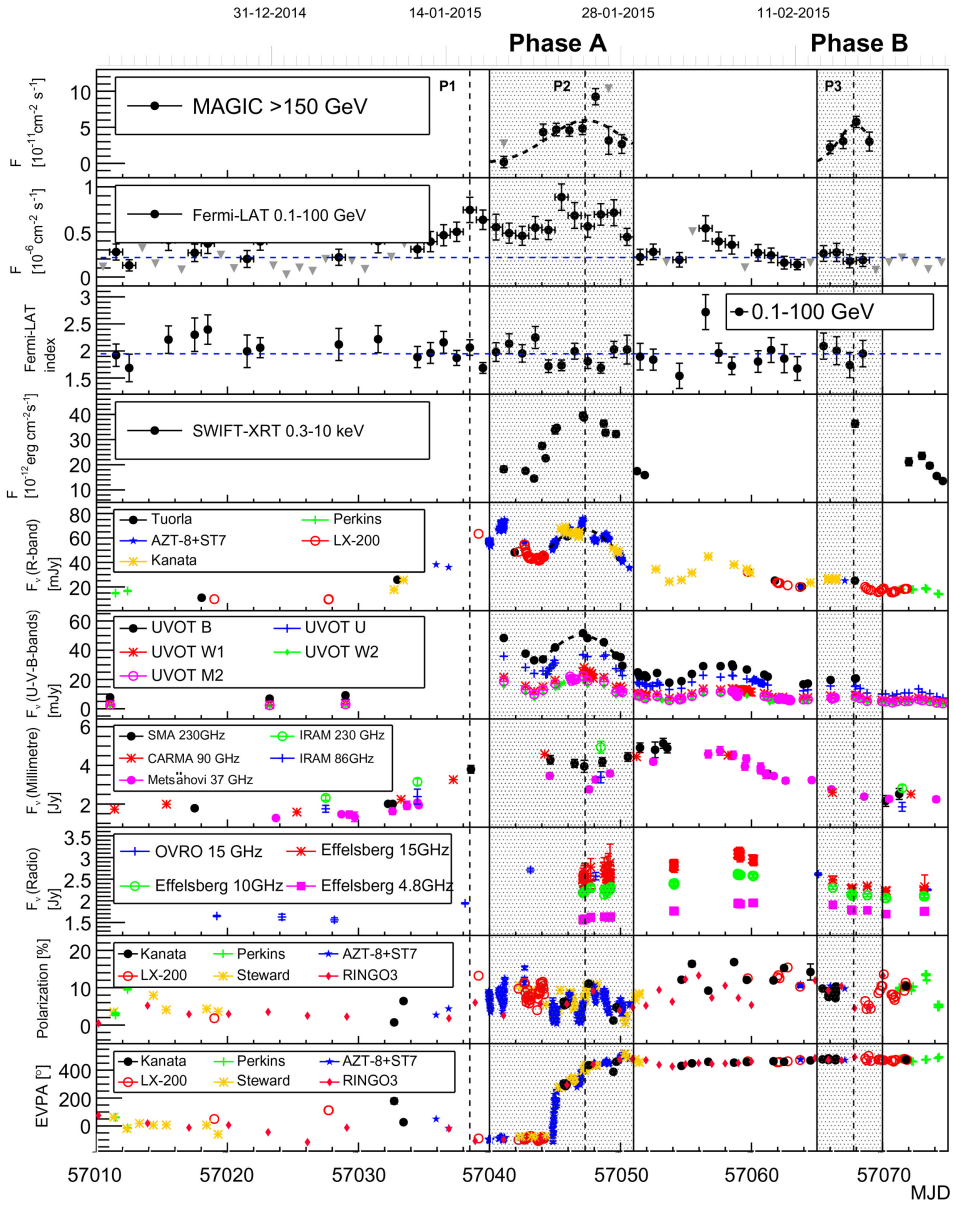

Figure 7.25. Multiwavelength light curve overlapping two TeV gamma-ray flares (top panel) from S50716 +714. The polarization is measured in the optical and near-infrared bands, and its EVPA is shown in the bottom panel. Image credit: MAGIC Collaboration et al. (2018), reproduced with permission © ESO.

timescale detected was $\Delta t_{\rm obs} \sim 2 - 3$ minutes. A second strong flare the next day was accompanied by dedicated X-ray coverage. Figure 7.26 illustrates the first flare light curve and the correlation between the TeV gamma-ray and X-ray emission during the second flare decrease.

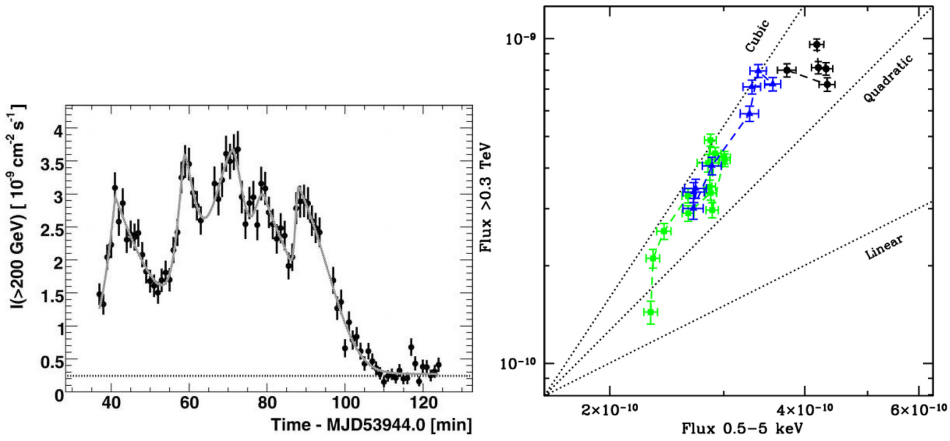

Figure 7.26. Left: TeV gamma-ray light curve of the 2006 July 28, flare from PKS 2155−304 in 1 minute intervals. The solid curve is a fit to the five subpeaks within the flare. Right: TeV gamma-ray and X-ray emission correlation from the second flare, July 29, decay. The colors (black—early; blue—mid; green—late) represent different time intervals within the flare, and the dotted lines represent different slopes for the relation $F_\gamma \propto F_X^\beta$. Image credit: Aharonian et al. (2007a, 2009), reproduced with permission © ESO.

A second flare revealed a roughly cubic relationship between the gamma-ray and X-ray fluxes $F_\gamma \ F_x^\beta$ with $\beta = 3$ during the flare decay phase. This challenges models based on a single population of electrons responsible for the flare (the so-called one-zone models) and suggests a complex source region, perhaps containing several electron populations and/or a dynamically changing source region (e.g., expanding blob with a changing magnetic field).

Using Equation (7.14) and $\Delta t_{\rm obs}$~2 − 3 minutes, the comoving source size can be constrained to $R'_{\rm src} \leqslant 0.3\delta$ au. If we now consider the scale of the underlying central engine in the rest frame of the AGN host galaxy, which is effectively the supermassive black hole's Schwarzschild radius R_S, we can infer the black hole's mass, avoiding the Doppler and Lorentz factor terms This is achieved by noting the rest-frame observed timescale $\Delta t_{\rm obs} = \Delta t'(1+z)/\delta$, for $\Delta t' = R'_{\rm src}/c$, $R_{\rm src} = R'_{\rm src}/\Gamma$ via length contraction and a head-on view such that $\delta \sim 2\Gamma$. We then note that $R_{\rm src} \sim R_s$ and find that $\Delta t_{\rm obs} \geqslant (1+z)R_s/(2c)$ (see Rieger 2019). Thus, the variability timescale constrains the black hole radius and hence its mass. With $\Delta t_{\rm obs}$~2 − 3 minutes, we find $M \leqslant 4 \times 10^7\ M_\odot$, about a factor of 100 below the mass estimated from the host galaxy luminosity, $\sim 10^9\ M_\odot$. However, the situation is likely to be more complex as summarized by Rieger (2019), and we will look at some acceleration scenarios below.

Besides the random/stochastic flaring on short timescales, in recent years a number of AGNs have displayed evidence of quasi-periodic oscillations (QPOs) with periods of 1 to 2 years (see Rieger 2019) although for many only a few cycles have been observed and thus statistical caution is warranted. A prominent example is the HBL PG 1553+113 ($z = 0.5$), which shows some evidence for a ~2.2 yr cycle in

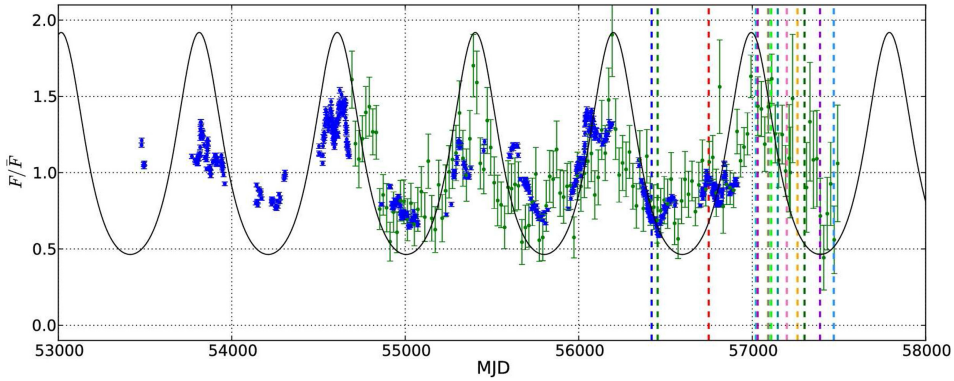

Figure 7.27. Long-term GeV gamma-ray (green points; 20 day bins) and optical (blue points) activity of PS 1553+113. The black line is a periodicity model, and the vertical dashed lines are epochs of spectral calculations. Image credit: Sobacchi et al. (2016) © 2016 The Authors, Published by Oxford University Press on behalf of the Royal Astronomical Society.

its GeV gamma-ray and optical activity (Ackermann et al. 2015a; Sobacchi et al. 2016) as shown in Figure 7.27.

Interpretation of this year-scale QPO behavior has led to the suggestion of binary supermassive black holes in orbit around each other (which would result from historical galaxy mergers) that may lead to peculiar patterns in the circumbinary accretion disk surrounding both black holes. The year-scale periodicity however would demand very close separations and hence significant gravitational-wave emission that would limit the lifetime of the binary system (a merger might be expected on a 10^4 yr timescale as a result). Thus, alternative explanations have been put forward for QPO behavior such as regular motions inside a rotating jet giving rise to periodic changes in the Doppler factor or modulation of the accretion flow onto the black hole. Further unbiased sampling of the gamma-ray and other waveband light curves for many AGN blazars will be needed to advance this topic.

Particle Acceleration in AGNs: The energy for the jet formation and subsequent particle acceleration is ultimately driven by the accretion process as the supermassive black hole converts the gravitational potential energy of surrounding matter to kinetic energy. It is one of the most powerful processes in physics that can generate radiation via heating of the accreting material. For matter falling onto a radius R toward a black hole with Schwarzschild radius R_S at an accretion rate $\dot{M}$, the accretion radiation luminosity can be written as

$$L_{\rm acc} = 0.5\dot{M}c^2(R_S/R) = \eta\dot{M}c^2 \tag{7.15}$$

where $\eta = 0.5(R_S/R)$ is the accreting efficiency to covert the matter rest mass–energy into radiation. Thus, accretion can be remarkably efficient. For AGNs with supermassive black holes we typically find $L_{\rm acc} \sim 10^{46}$ erg/s, which requires an accretion rate of $\dot{M} \sim 1\ M_\odot$/yr. This is to be compared to stellar-sized black hole accretion in

XRBs and microquasars (as discussed earlier) with $L_{acc} \sim 10^{30-40}$ erg/s and $\dot{M} \sim 10^{-7} M_{\odot}$/yr. The formation of the jet associated with the accretion disk is still the topic of much debate. A general principle is that the magnetic field attached to the rotating accretion disk is wound up into a helical pattern, acting as a guide for particles to be accelerated at the jet base or along the jet, perpendicular to the accretion flow. From the Hillas plot shown earlier (Figure 7.19), we can easily see that the size and magnetic field strength of the accretion region and jet are ideal places for particle acceleration to extreme energies, hence the long-held notion that AGNs are the sources of the highest-energy cosmic rays beyond 10^{20} eV. For a more in-depth discussion, the reader is referred to the recent review by Blandford et al. (2019).

Following the review by Rieger (2019), for illustration of some possibilities, we present in Figure 7.28 several scenarios that have been put forward to explain the time-varying particle acceleration and subsequent variable photon emission.

The three shown here (see Rieger 2019 and references therein) all involve small-scale features within the jet or at the jet base close to the black hole horizon. They include electron/positrons accelerated in an electric field near the black hole horizon, jet-in-jets involving mini-jet features that locally accelerate particles via reconnection, and a matter interaction model involving cosmic-ray interactions with photon fields from stars embedded in the jet. The latter involves the hadronic process while the former two involve the leptonic (IC gamma-ray and synchrotron radio to X-ray) process. For the leptonic process, the gamma-ray emission is often attributed to the SSC process but external IC (upscattering of external photon fields such as the CMB and infrared photons farther out in the jet or in a luminous broad line region around the accretion disk) has been considered. For hadronic models, the scenario as shown in Figure 7.28 is one such geometric setup. Generally, the acceleration of protons to over 10^{19} eV in extremely intense magnetic fields of 20 G or more (compared to the milligauss fields required in leptonic SSC models) is required. In this case the gamma-ray emission results from synchrotron emission directly from the protons or from the π° decay generated when these protons interact with low-energy photons ($p\gamma$ process as outlined in Chapter 8 as this is also a major production channel for

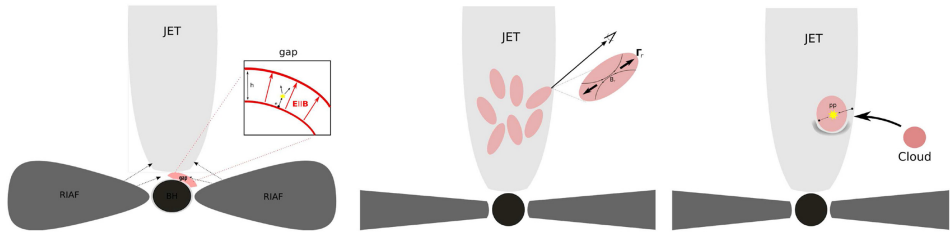

Figure 7.28. Several scenarios to explain TeV gamma-ray variability from AGNs. Left: electron/positrons generated in electric fields near the black hole horizon lead to inverse-Compton gamma rays. Middle: "Jet-in-jet" where many mini-jet plasmoids can accelerate particles via reconnection Right: clouds or stars within the jet act as a dense source of cosmic-ray protons. Image credit: Rieger (2019) with permission of MDPI.

neutrinos). The fast synchrotron cooling time might be a more natural explanation (versus $p\gamma$ processes) to explain the rapid (minute-wise scale) flaring episodes discussed above (e.g., Barkov et al. 2012).

Extragalactic Background Light Constraints: An important issue affecting the observed high-energy flux from AGN blazars is the absorption of gamma rays on the low-energy (or soft) photon fields permeating the universe known as the extragalactic background light (EBL). The level of EBL photons reflects the star formation history of the universe and is thus a fundamental signature of its evolution.

Gamma rays will annihilate to electron/positron pairs upon interaction with soft photon fields such that the observed flux at Earth $F_{\rm obs}(E)$ will be attenuated according to the following relation:

$$F_{\rm obs}(E) = F_{\rm int}(E)\,\exp\bigl(-\tau\bigl(E_\gamma,\, z\bigr)\bigr), \tag{7.16}$$

where $F_{\rm int}(E)$ is the intrinsic flux at the source, and $\tau(E,\, z)$ is the absorption optical depth versus gamma-ray energy E_γ and distance/redshift z. The optical depth is dependent on the distribution of EBL photons and the pair production cross section. The pair production cross section peaks for the interaction of an isotropic soft photon field of blackbody temperature T (eV units, or peak wavelength $\lambda_{\mu\rm m}$) with gamma rays (TeV units) of energy $E_\gamma = 0.9E_{\rm T,eV} \approx 0.7\lambda_{\mu\rm m}$. Thus, optical to infrared photons are relevant to GeV gamma-ray absorption, while mid-infrared photons are relevant to TeV gamma-ray absorption (see, e.g., Aharonian et al. 2006c, 2008d).

The EBL across the optical to infrared bands is quite difficult to measure directly owing to foreground contamination. However, in recent years the EBL has been quantified by fitting Equation (7.16) to the observed flux from an ensemble of blazar spectra spanning a range of redshifts and a variety of EBL models in a statistical approach. Earlier methods adopted the approach that the intrinsic gamma-ray spectral index would be $\Gamma \geqslant 1.5$ based on fundamental particle acceleration and IC scattering theory. Figure 7.29 illustrates the most recent compilations of results from Fermi-LAT at GeV energies (Abdollahi et al. 2018), and those from TeV gamma-ray telescopes such as HESS, MAGIC, and VERITAS (Biteau 2015; HESS Collaboration et al. 2017; Acciari et al. 2019; Abeysekara et al. 2019; Desai et al. 2019).

Here we can see that the EBL constraints from the gamma-ray measurements are generally at the bottom end of those from the direct measurements. The complementary roles of the GeV and TeV bands are also evident with the former constraining the EBL up to a few micrometers and the latter taking over above those wavelengths up to about 100 μm. Ever since the first gamma-ray constraints on the EBL were published (Aharonian et al. 2006c), the GeV to TeV gamma-ray results have suggested that the universe is somewhat more transparent to gamma-ray photons than initially thought, giving promise to future TeV facilities such as the CTA to probe many sources beyond redshift $z = 2$ (as we will highlight briefly at the end of this chapter).

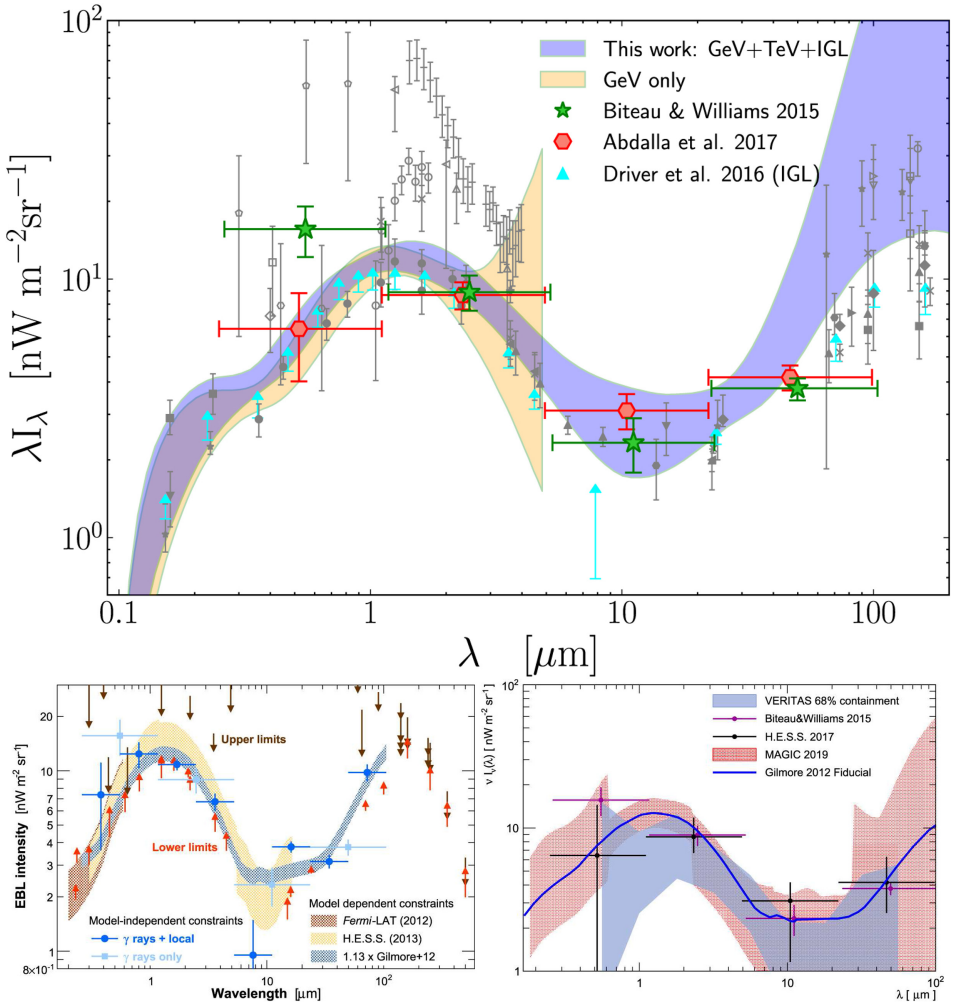

Figure 7.29. Compilation of recent EBL constraints from gamma-ray blazar fluxes and other direct measurements. Top: from Fermi-LAT, separated according to blazar redshift (Desai et al. 2019). Bottom left: from the combination of HESS, MAGIC, and VERITAS up to 2015 at $z = 0$ (Biteau 2015). Bottom right: most recent comparison from VERITAS (Abeysekara et al. 2019) including the latest results from the HESS Collaboration et al. (2017) and MAGIC (Acciari et al. 2019), at $z = 0$.

7.6.2 Non-AGN Galaxies

Among the non-AGN galaxies detected in gamma rays, starburst galaxies (with high rates of massive star formation) represent a prominent type. About a dozen starburst galaxies are seen in the GeV band (Abdollahi et al. 2020; Ajello et al. 2020c) with two of them, NGC 253 and M82, seen at TeV energies (Acero et al. 2009a; VERITAS Collaboration et al. 2009; HESS Collaboration et al. 2018h).

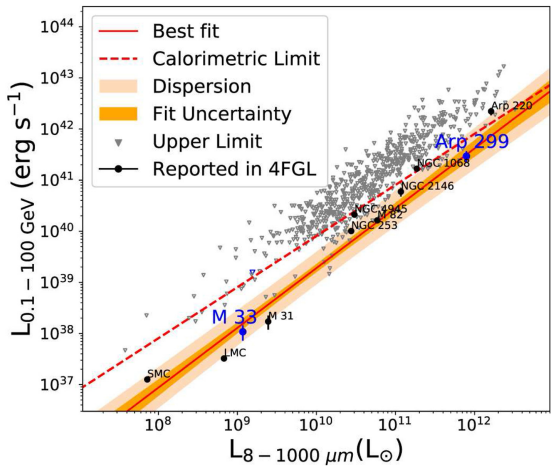

Figure 7.30. GeV gamma-ray and infrared luminosity correlation for starburst galaxies (and normal galaxies with some level of starburst activity). Image credit: Xi et al. (2020b).

At the lower end of starburst activity, several "normal" galaxies have been seen in the GeV band (besides our own Milky Way with disk-dominated GeV emission) such as the Andromeda Galaxy (M31; Abdo et al. 2010a; Ackermann et al. 2017b); the LMC (Abdo et al. 2010c; which was first detected in GeV gamma rays by EGRET Sreekumar et al. 1992); the SMC (Abdo et al. 2010d), which are relatively active in star formation for their small sizes; and M33, a satellite of the Andromeda galaxy. Most recently, GeV gamma-ray emission from M33 and Arp 229 (Xi et al. 2020b) has also been reported. The GeV to TeV gamma-ray emission is thought to be tied to the level of massive star formation (leading to cosmic-ray acceleration and their interaction with the interstellar gas). Evidence of this comes from the general correlation between the GeV and infrared emission, with the latter being a long-recognized tracer of massive star formation (note that the 1.4 GHz radio continuum emission is also a good tracer of star formation).

The GeV emission from two starburst galaxies also appears to be variable (Peng et al. 2019), suggesting the potential for an AGN-like component powered by a central supermassive black hole. Given the expected presence of a high level of cosmic-ray acceleration in starburst galaxies and their recent links to arrival directions of the highest-energy cosmic rays (Aab et al. 2018), they may contribute to the underlying TeV to PeV cosmic rays responsible for the astrophysical neutrinos detected by IceCube (Aartsen et al. 2013) and the extragalactic gamma-ray background (see, e.g., Ajello et al. 2020c and references therein). A suggestion for a large-scale (several kiloparsecs) GeV gamma-ray halo around M31 (Karwin et al. 2019) may indeed have further implications for the connection to the neutrino events seen by IceCube (Recchia et al. 2021).

7.6.3 Gamma-Ray Bursts

GRBs are quite likely to have been the first gamma-ray sources to be detected in the 1960s by US military satellites (e.g., Klebesadel et al. 1973, and as discussed in Section 7.1.1). Today, they are probably the gamma-ray source type that has attracted the most attention. The groundbreaking BATSE detector on board the CGRO, which cataloged over 1600 GRBs (Paciesas et al. 1999), showed that GRBs can be separated into two main types based on the duration of their MeV gamma-ray flares. While all GRBs exhibit a rapid falloff in flux over time, their falloff times are generally characterized as T_{90}, the time taken for their integral photon counts to increase from 5% to 95% of the total counts. The so-called short GRBs (SGRBs) and long GRBs (LGRBs) have $T_{90} \leqslant 2$s and $T_{90} \geqslant 2$ s, respectively, which define their so-called prompt emission. Weaker afterglow emission has been observed from many GRBs up to timescales of months, and often over a wider range of wavebands compared to the prompt emission (usually dominated by low-energy gamma rays).

More than 2000 GRBs are now cataloged by the Swift/Gehrels-BAT and Fermi-GBM telescopes (Lien et al. 2016; von Kienlin et al. 2020). Above 0.1 GeV, Fermi-LAT has detected of order 170 GRBs (Ajello et al. 2019), with a few of them emitting photons above 50 GeV. At TeV energies, GRBs were finally unambiguously detected in 2019 after several decades of searching. An early hint for a GRB detection was reported by MILAGRITO (Atkins et al. 2000), a precursor to the MILAGRO water Čerenkov telescope. The compelling TeV detections by MAGIC and HESS of GRB 190114C, GRB 180729B, and GRB 201216C (MAGIC Collaboration et al. 2019; Abdalla et al. 2019; de Naurois et al. 2019; Blanch et al. 2020) have so far been of LGRBs (up to $z \sim 0.8$), with HESS detecting GRB 180729B up to 10 hr after the prompt emission. However, just recently, MAGIC reported a marginal detection of the nearby ($z = 0.162$) SGRB GRB 160821B (Acciari et al. 2021) starting from 24 s after the burst lasting for 4 hr.

Today, it is accepted that GRBs are generated by relativistic jet outflows generated by two distinct types of objects. The LGRBs are established as the result of the core collapse of a massive star (Woosley & Bloom 2006; often called the "collapsar" model). SGRBs were for many years theoretically linked (e.g., Mészáros 2002) to the merger of compact objects, usually a pair of neutron stars (Berger 2014). It was not until the gravitational-wave signal from the binary neutron star (BNS) merger GW 170817 was linked to the SGRB GRB 170817A (Abbott et al. 2017) and a radio jet (Mooley et al. 2018) that this theory was confirmed. It is recognized that this event was an SGRB viewed slightly off axis from its jet direction (~20°), in what is termed a kilonova, an r-process supernova powered by a BNS or neutron star and black hole merger, with generally isotropic emission that includes an SGRB jet component. The isotropic emission is generated by high-mass element nucleosynthesis, leading to an optical/infrared counterpart. Several other SGRBs are also associated with kilonovae (e.g., GRB 160821B was tentatively detected in the TeV band by MAGIC, as discussed above).

In the GeV band, the LGRBs dominate with less than 20 of the ~170 Fermi-LAT GRBs being SGRBs, suggesting they are somewhat less able, compared to LGRBs,

to accelerate particles above multi-GeV energies. The general picture of particle acceleration in all GRBs involves a jet process, not unlike that found in AGN blazars, although there are some differences. The jet formation is induced by the core collapse or compact object merger process but many aspects remain unclear. In any case, the gamma-ray energy released in GRBs reaching 10^{55} erg (isotropically equivalent) in a few seconds makes them the most extreme explosive events since the Big Bang, thus requiring extraordinary conditions to accelerate particles.

The particle acceleration in a GRB is likely related to the formation of shocks at various locations and times within the jet. What causes these shocks is still the subject of much debate, such as from photon radiative pressure (the fireball model; Meszaros & Rees 1993) or magnetic pressure (see review by Pe'er 2019). Figure 1.4 presents a general picture illustrating shock in a GRB jet (from an LGRB or SGRB progenitor), as well as the prompt and afterglow emission regions. The prompt emission is generated in internal shocks set up when shells of material in the jet (moving at slightly different speeds) interact. The afterglow emission is related to a shock front at the leading edge of the expanding GRB ejecta. Additionally, a "reverse" shock may be generated when the external shock encounters the interstellar medium or the circumstellar medium from the progenitor (e.g., Piran 1999). The reverse shock is believed to be responsible for radio and optical flashes or the brightening detected in some GRBs. Additional components unique to SGRBs are time-extended X-ray emission possibly related to the still-active postmerger object (e.g., a magnetar) and the kilonova emission discussed earlier.

The prompt and afterglow emission components up to GeV energies are generally attributed to the synchrotron process from relativistic electrons. The so-called "Band" function (Band et al. 1993), a broken power law with an exponential cutoff, has been successful in empirically describing the spectral shape of this emission up to about 0.1 GeV. The function parameters (spectral slopes, exponential cutoff, and break energy) can follow the evolution of the GRB spectrum as it evolves from the prompt to the afterglow phase. However, additional high-energy components have been required since the detections of multi-GeV photons by EGRET and Fermi-LAT, and even more so since the recent TeV detections.

We will now take a closer look at the recent TeV gamma-ray results, as they have provided some further insight into GRB physics. The recent TeV detections of the mostly afterglow emission have provided the first observational evidence for an additional IC component (MAGIC Collaboration et al. 2019), and detailed time evolution of the afterglow emission across a wide range of energies. Figure 7.31 compares the light curve and energy spectra evolution for GRB 190114C. We can see that the TeV light curve follows a generally similarly smooth time evolution decay law (flux $\propto t^{-\alpha}$ with α in the range -1.5 to -1.3) seen in the X-ray and GeV bands. The range of α values reflects the different times postburst the measurements concentrate on and the expected evolution of spectral features (e.g., breaks) appearing in the underlying electron spectrum (see Ajello et al. 2020b for a more in-depth discussion).

The appearance of a double peak in the spectrum across the X-ray to gamma-ray bands is a signature of synchrotron and an additional IC process to account for the

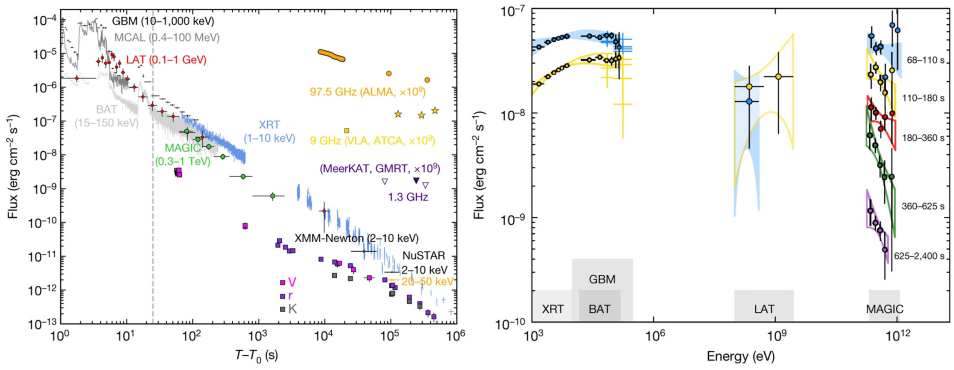

Figure 7.31. Left: light curve (energy flux versus time reference against the initial burst time T_o) for GRB 190114C. The MAGIC TeV fluxes (green) are compared with fluxes from the radio to GeV gamma-ray bands. Right: energy spectra for the interval 68 s to 2400 s after the initial burst, in the X-ray, GeV, and TeV gamma-ray bands. Images from MAGIC Collaboration et al. (2019), with permission of Springer.

TeV emission. Specifically, the TeV emission is thought to arise from the SSC process (upscattering X-ray synchrotron photons via the IC process as discussed earlier for AGN and some other gamma-ray source types). Alternative processes are synchrotron emission directly from electrons or protons. In both cases, particles of extreme energies are required (PeV or higher energies), which would not be necessarily unexpected from GRB jets. However, the total energy budget for proton synchrotron is uncomfortably large (due to the large proton mass) and for electron synchrotron up to TeV energies, the initial jet Lorentz factor would need to exceed values of ~1000 (linked to the maximum energy electrons can attain due to synchrotron losses), also uncomfortably large in the context of how such jets are expected to form. The SSC TeV emission keeps the maximum synchrotron emission to sub-GeV values, thereby constraining the initial jet Lorentz factor to a range 300–700, more in line with the expectation for GRB jets.

7.6.4 Other Flaring Gamma-Ray Sources

We conclude our look at extragalactic sources with a quick look at some additional topics.

The second Fermi-LAT flare catalog (Abdollahi et al. 2017) from 2017 lists over 4000 GeV flare events associated with over 500 sources. The vast majority of these sources are AGNs (BL Lac and FSRQs) as expected, and just over 10 are associated with Galactic sources (XRBs, novae, and pulsars). Interestingly, 77 of the flares have no association and the majority of these are extragalactic with just two found within 5° of the Galactic Plane. Furthermore, the photon spectral index of these nonassociated sources tends to be rather hard ($\Gamma \leqslant 1.5$,) which might suggest a new class of gamma-ray transients that could be studied in more detail by future TeV facilities.

Finally, Fermi-LAT has very recently revealed exciting evidence for GeV emission from a magnetar giant flare (Fermi-LAT Collaboration et al. 2021). The burst location is consistent with several galaxies, IC 1576, IC 1578, and IC 1582, and the starburst galaxy NGC 253 (the Sculptor Galaxy) at 3.5 Mpc distance. It is linked to GRB 200415a, which was originally classified as a short GRB based on its MeV emission as seen by the Fermi-GBM. The unusually long delay (19 s) to the GeV emission and QPO seen in the MeV signal (see references in Fermi-LAT Collaboration et al. 2021) point to a giant magnetar flare. The delayed GeV emission is currently suggested to arise from the ultrarelativistic outflow from the giant flare interacting with dense material surrounding the magnetar. This result may suggest exciting new prospects for GeV to TeV gamma-ray emission to be detected from other magnetar giant flares from within the Milky Way, and other nearby galaxies (as has been long suggested, e.g., Ioka et al. 2005). Giant flares are thought to be related to a significant rupture of neutron star crust or deformation of the neutron star magnetosphere and given they are so far seen only once from different magnetars, they may represent a major step in their evolution.

7.7 Additional Physics Topics with Gamma Rays

So far our discussion has centered on astrophysical situations where particle acceleration is taking place, giving rise to relevant gamma-ray emission. In this section, we will briefly review the range of additional physics topics impacted by gamma-ray studies beyond this discussion so far. These additional topics are within the emerging fields of astroparticle physics and particle cosmology.

Since the Big Bang, the universe has left behind traces of its evolution via many so-called cosmic relics. The elusive dark matter is the best known of these relics, accounting for over 75% of the universe's matter we see today. Its detection via direct and indirect methods is discussed broadly in Chapter 10. Here, we will just emphasize the role that gamma rays play in indirect detection methods.

Weakly interacting massive particles (WIMPs) have been the most popular idea for dark matter. The self-annihilation of WIMPs (such as supersymmetric neutralino particles) can give rise to gamma rays in the form of line emission (with energy matching that of the WIMP) or broadband emission from secondary hadrons. Gamma rays in the GeV to TeV band are considered the most fruitful avenue to probe given the theoretical mass of WIMPs mostly appears in the same energy range. Observationally, gamma-ray emission is ideally searched for in regions that are astrophysically boring. As a result, dwarf galaxies, which are not expected to host strong astrophysical particle accelerators, are considered ideal sources. On the other hand, the intense gravitational attraction at the center of our galaxy makes it a compelling place to look, despite the confusion with astrophysical sources. To date, no convincing GeV to TeV gamma-ray evidence for dark matter has been seen from dwarf galaxies or from our Galactic Center looking for broadband and line emission (e.g., Abdallah et al. 2018; Abdalla et al. 2018; Abdallah et al. 2020; Abdollahi et al. 2020; Hoof et al. 2020).

A well-debated topic has been an excess of emission around GeV energies above the astrophysical background expectation seen by Fermi-LAT and its relation to dark matter (see Ackermann et al. 2017a, and references therein). However, several alternative astrophysical explanations appear feasible, such as an unresolved population of millisecond pulsars, star formation processes, or the central supermassive black hole (e.g., Bartels et al. 2016; Macias et al. 2018). One particular aspect disfavoring the dark matter interpretation is the generally nonspherical and potentially clumpy morphology of this GeV excess (e.g., Yang & Aharonian 2016). The systematic uncertainties in the astrophysical background models that can lead to large-scale GeV gamma-ray features are also being investigated in more detail, shedding light on the need for further understanding of potential particle sources and their time-dependent nature (e.g., Porter et al. 2019).

Besides WIMPs, there are a number of alternative ideas for dark matter across the range of mass scales (see e.g., Bertone & Tait 2018; Doro 2017). Some of them, such as axions (or light axion-like particles, ALPs) and primordial black holes (PBHs), could have distinct signatures in the gamma-ray band. Under certain conditions, gamma-ray photons may oscillate into ALP states (Hooper & Serpico 2007; de Angelis et al. 2011), which can avoid absorption on the EBL over cosmological distances. Thus, a lack of EBL absorption on the GeV to TeV spectra of distant AGN blazars is a way to search for evidence of such ALPs. However, for AGN blazar spectra so far studied in detail at GeV and TeV energies, there is at present no indication for such an effect (e.g., Sanchez et al. 2013; Domínguez & Ajello 2015). The gamma-ALP oscillation may also impart energy-dependent oscillations (dependent on the mass of the ALP and fluctuations in the intervening intergalactic magnetic field) in the gamma-ray flux potentially within the energy resolution of telescopes. So far, rather tight constraints on the ALP mass in the range of 4 to 100 neV have been set using Fermi-LAT and HESS observations of NGC 1275 (radio galaxy) and PKS 2155 −304 (AGN blazar), respectively (Ajello et al. 2016; Abramowski et al. 2013; Zhang et al. 2018).

PBHs across a huge mass range (Planck mass up to $\sim 10^5\ M_\odot$) are a predicted consequence of density fluctuations in the radiation-dominated era of the early universe from inflation up to about 50 kyr after the Big Bang and are a potential source of dark matter (see, e.g., Carr & Kühnel 2020; Ballesteros et al. 2020). The gravitational-wave signals from mergers of black holes with mass $>10\ M_\odot$ (Abbott et al. 2016) and the very recent suggestion for a stochastic gravitational-wave background (Arzoumanian et al. 2020) have sparked renewed interest in PBH studies and their potential as dark matter candidates. PBHs lose energy or evaporate via Hawking radiation according to the PBH's thermal temperature, which follows a $1/M_{\rm BH}(t)$ dependence, where $M_{\rm BH}(t)$ is the PBH's mass varying with time. As the PBH nears its endpoint with ever decreasing mass, its thermal temperature can rise to GeV energies, producing a burst of fundamental particles (quarks, gluons, electrons, neutrinos, photons) and gamma-ray photons. At the current age of the universe, it's expected that PBHs of mass $\sim 5 \times 10^{14}$ g

could emit seconds-duration pulses of GeV to TeV gamma-ray emission at their final stages. To date, no evidence for such gamma-ray signals have been seen, and the most recent searches have been conducted using data from the wide-field Fermi-LAT and HAWC (Ackermann et al. 2018; Albert et al. 2020b) telescopes.

Gamma rays can be used to probe for Lorentz invariance violations (LIVs), a consequence of quantum gravity and string theory models (e.g., Alfaro 2005; Kostelecký & Samuel 1989; Amelino-Camelia 2001). The LIV signatures are suggested to appear via a variety of avenues such as a speed-of-light dependency on photon energy, decay of photons, production of Čerenkov light in the vacuum, and changes in the threshold for pair production leading to reduced EBL absorption (e.g., Amelino-Camelia et al. 1998; Stecker & Glashow 2001; Stecker 2003; Kifune 1999). The LIV effect can be characterized by the energy scale at which it is invoked $E_{\mathrm{LIV}}^{(n)}$, and this is of order the Planck energy ($\sim 1.22 \times 10^{28}$ eV) or higher. A popular LIV effect to search for has been the temporal delay in photon arrival times from pulsed or flaring sources such as the Crab Pulsar, and various AGNs or GRBs across the GeV and TeV bands (e.g., MAGIC Collaboration et al. 2017; Abdalla et al. 2019; Vasileiou et al. 2013). This technique depends on assuming there are no intrinsic temporal delays in the photon production at the source, something that is not always viable.

The strongest constraints on the LIV mass scale of $>2.2 \times 10^{31}$ eV (1800 times the Planck energy) for a so-called LIV effect of order $n = 1$ have so far been set by HAWC using gamma-ray photons of energy $\geqslant$100 TeV (Albert et al. 2020a) looking for the effects of superluminal photon decay giving rise to unusually strong cutoffs in gamma-ray spectra. A more complete review of the various potential LIV gamma-ray photon signatures, LIV theory, and comparison of experimental constraints is given by Martínez-Huerta et al. (2020).

Magnetic monopoles are a fundamental consequence of magnetic quantization (suggested by Dirac in 1931). They are thought to be produced during the very early universe, resulting from Grand Unified Theories of all the fundamental forces, and also specifically during the electroweak phase transition, which saw the separation of the electroweak forces at about 10^{-32} s after the Big Bang (see reviews by Patrizii & Spurio 2015; Patrizii et al. 2019; Mavromatos & Mitsou 2020). Monopole masses ranging from a few TeV up to $\sim 10^{13}$ GeV are suggested and because they are charged (magnetically charged), they can be accelerated to relativistic speeds in cosmic magnetic fields. The makeup of monopoles (a combination or "soup" of fundamental quarks, gluons, W and Z particles, their antiparticles, and photons—e.g., Patrizii et al. 2019) means that they can also lose energy via well-known processes such as ionization, and at extreme energies (with monopole Lorentz factors $>10^7$) via pair production and photonuclear reactions. A fundamental upper limit on the monopole flux, known as the Parker bound, is set according to the maximum flux of monopoles allowed to prevent quenching or short-circuiting of Galactic magnetic fields at a rate faster than such fields are created in galaxies (a modified Parker bound comes from scaling this limit with the monopole mass).

For sufficiently high energy (velocity greater than the local speed of light in a medium such as air or water), monopoles can also create Čerenkov photons at a rate a few 1000× greater than that for a single electric charge (Tompkins 1965). As a result, ground-based gamma-ray telescopes detecting Čerenkov light can probe for ultrarelativistic monopoles (with velocity $v/c \sim 1$) via their unique linear appearance (Doro 2017), and the first upper limits have been set (Spengler & Schwanke 2011) a factor of ∼100 higher than the Parker bound. Much tighter limits (below the Parker bound) are available to neutrino telescopes detecting Čerenkov light in water or ice, as the lower local speed of light permits Čerenkov light to be produced at much lower energies down to $v/c > 0.5$. Additionally, the particle air showers generated by ultrarelativsitic monopoles could be detected by cosmic-ray telescopes like the Pierre Auger Observatory (Aab et al. 2016; Patrizii et al. 2019).

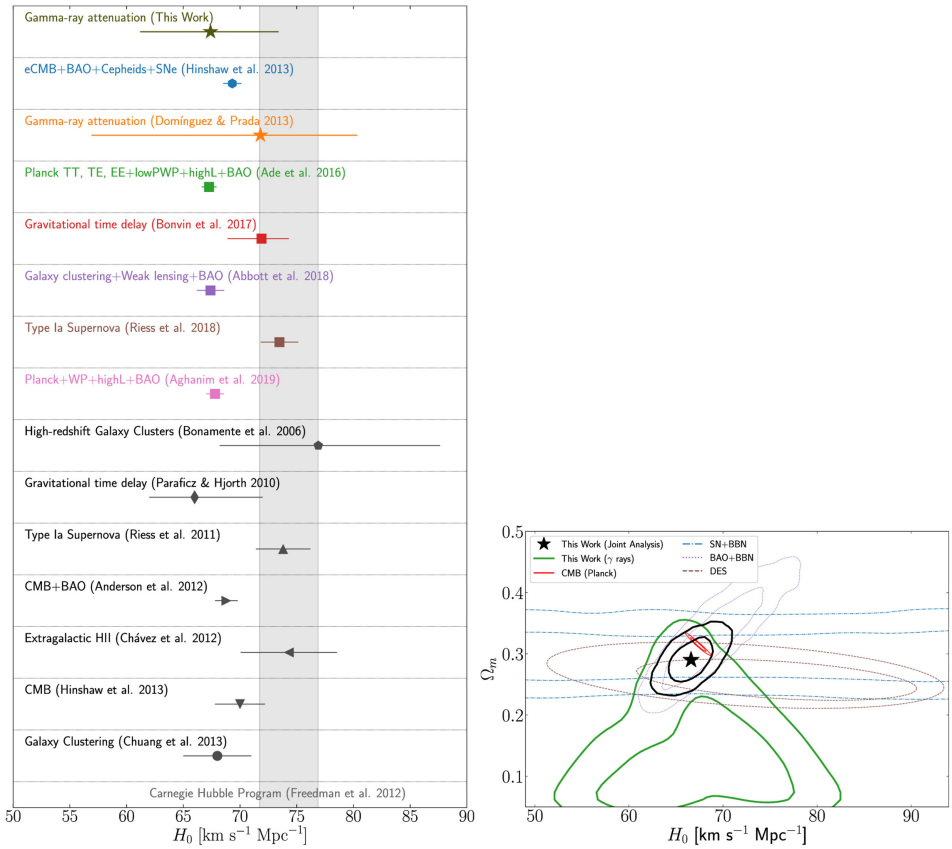

Figure 7.32. Left: Hubble constant H_o constraints from gamma-ray observations (top measurement) compared to results from other techniques (see Domínguez et al. 2019 and references therein). Right: H_o and matter density Ω_m constraints from gamma-ray measurements (green contours) and a joint fit from gamma rays and other techniques (supernova plus Big Bang nucleosynthesis SN+BBN; weak lensing from the Dark Energy Survey, DES; cosmic microwave background, CMB; and baryon acoustic oscillations, BAOs). Images from Domínguez et al. (2019).

Finally, we will examine the determination of cosmological parameters such as the Hubble constant, $H_\circ$ and the matter content in the universe Ω_m. The level of EBL (discussed earlier) in the universe is a fundamental consequence of galaxy evolution as a function of redshift. As a result, constraints on the EBL optical depth can then lead to constraints on $H_\circ$ and Ω_m when interpreted in terms of a model evolution for the universe (e.g., the standard ΛCDM model). The recent results from Domínguez et al. (2019), shown in Figure 7.32, used an ensemble of GeV spectra from 739 AGN blazars (and one GRB) measured by Fermi-LAT (Abdollahi et al. 2018) and TeV spectra from 38 AGN blazars by various ground-based gamma-ray facilities (Desai et al. 2019).

We can see that the gamma-ray measurements of the EBL can offer another measurement of $H_\circ$, in this case with a value of about 65 to 67 km s^{-1} Mpc^{-1} with a 5% to 10% error. This appears consistent with those from the CMB fluctuations and from baryon acoustic oscillations and potentially further supports the tension in the $H_\circ$ measurement arising from supernova and Cepheid measurements. The matter density parameter Ω_m is found to be 0.29 within a percent when jointly combined with other measurements.

7.8 Next-generation Gamma-Ray Observatories and Future Perspectives

In this final section we will briefly look at the next generation of gamma-ray facilities under consideration, construction, or recently commenced and include an outlook on what might come next. Figure 7.33 illustrates the differential flux sensitivity comparisons for various past, current, and proposed gamma-ray facilities.

The MeV band has been undersampled since the end of the COMPTEL telescope in 2000 (it was on board the CGRO satellite along with the EGRET and BATSE telescopes). The MeV telescope proposals eASTROGAM (de Angelis et al. 2018) and AMEGO (McEnery et al. 2019) are gathering momentum (the AMEGO

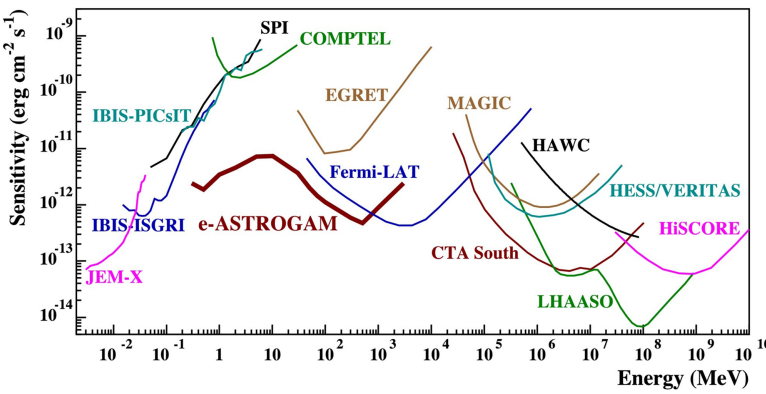

Figure 7.33. Differential flux sensitivities for various MeV to PeV gamma-ray facilities (past, current, and proposed). Tracking facilities like HESS assume a 50 hr observation time while wide-field facilities like HAWC and LHAASO assume a 1 yr observation time. SPI, IBIS, and JEM-X are detectors on board the INTEGRAL satellite. Image credit: de Angelis et al. (2018), Copyright 2018, with permission from Elsevier.

sensitivity and energy coverage are somewhat similar to that of eASTROGAM as shown in Figure refsens). They both aim to significantly improve the angular resolution in the MeV band down to ~1° or better, and energy resolution to 20% or better. A new aspect will be their ability to measure the polarization of gamma rays. This will open up new ways to discriminate the leptonic and hadronic origins of the gamma-ray emission and the ability to track magnetic field structures in relativistic jets (see review by Ilie 2019). Additionally, the THESEUS mission (Amati et al. 2018) has been discussed as the next major facility (following on from Swift-Gehrels-BAT) for transient sources such as GRBs sampled across the X-ray to MeV band with the smaller-scale SVOM mission (Claret 2018) being a potential pathfinder.

In the GeV band, the Fermi-LAT remains the main instrument for the foreseeable future (and can in principle operate for another decade due to its lack of expendables on board). The GAMMA-400 mission (Topchiev et al. 2016) has been proposed as a potential successor to Fermi-LAT, and the AMS100 mission (Schael et al. 2019), designed for cosmic-ray studies, will also have excellent gamma-ray detection performance in the GeV band. The DAMPE gamma-ray telescope (see Li et al. 2021) has a focus on high GeV-energy resolution studies for dark matter searches and the detection of some transients and is expected to operate well into the current decade.

In the multi-GeV band and above, the next-generation ground-based CTA, www.cta–observatory.org is the key facility. CTA will initially comprise 64 telescopes situated across northern and southern sites (Canary Islands, Spain in the north, and Paranal, Chile in the south; the "Alpha" configuration). About 80% of the telescopes will be located at the southern site. The comparatively greater focus on Galactic sources at the southern site requires a wide energy coverage detecting gamma rays beyond 100 TeV in order to probe for extreme Galactic particle accelerators or PeVatrons as discussed earlier. The CTA sensitivity (CTA-North and CTA-South for 50 hr observation; sensitivity versus time and energy) is shown in Figures 7.33 and 7.34. Here we can clearly see CTA is expected to be at about 10 times more sensitive than current instruments in the "workhorse" 1 to 10 TeV energy range and extends the energy coverage from about 20 GeV to beyond 100 TeV. CTA's angular resolution, reaching arcminute scales for gamma rays >10 TeV or so, will also provide the most detailed morphological studies in gamma rays so far. Importantly, CTA will close the energy coverage gap with Fermi-LAT and thus will open up a new window in the study of gamma-ray transients and variable sources (e.g., AGN blazars, GRBs, XRBs, novae, etc.). Figure 7.34 (right panel) shows CTA's time-limited sensitivity improvement over that of Fermi-LAT. This is due to CTA's huge effective collection area ($>10^4$ m^2) in the multi-GeV-energy domain, which may enable CTA to detect AGN blazar flares to redshift $z \sim 2$ and bright GRBs out to redshift $z \sim 4$.

A large fraction of CTA's initial observing time will be devoted to large key science projects (KSPs) focusing on a wide range of topics including systematic surveys of the Galactic Plane, Galactic Center region, extragalactic sky, and LMC, and targeted projects to study transients, AGNs, star formation regions, particle accelerators and PeVatrons, dark matter, and beyond-Standard-Model physics.

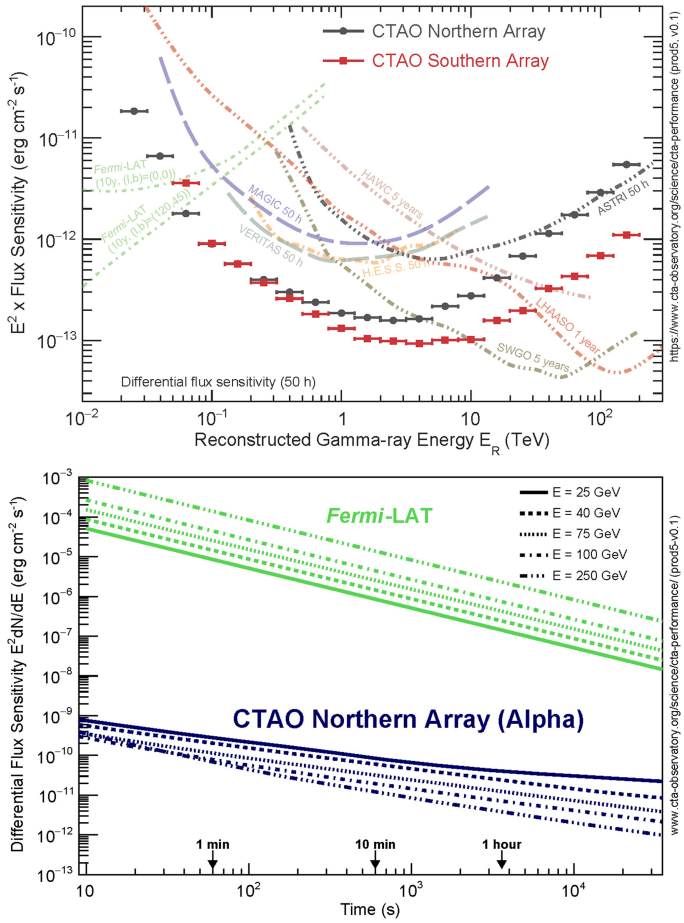

Figure 7.34. Differential flux sensitivities vs. energy and time for CTA ('Alpha' configuration), Fermi-LAT, and several other gamma-ray facilities. Images credit: Cherenkov Telescope Array Observatory (CTAO) Northern/Southern Array, and Cherenkov Telescope Array Consortium (CTAC), CTA performance, https://www.flickr.com/photos/cta_observatory/26079109147/in/album-72157673853528865/ and https://www.cta-observatory.org/wp-content/uploads/2019/04/CTA-Performanceprod3b-v2-South-20deg-ShortTerm.png.

Non-gamma-ray science such as optical intensity interferometry and optical photometry are also being pursued because CTA will represent a large array of optical telescopes in the world. Further details of these science programs can be found in CTA, www.cta-observatory.org. More recently, CTA's potential to probe fundamental physics (such as the EBL absorption, related cosmology, Lorentz invariance in quantum gravity, and dark matter at the Galactic Center) was updated in detail (Abdalla et al. 2021; Acharyya et al. 2021).

Regarding new wide-field ground-based gamma-ray telescopes, the Large High Altitude Air Shower Observatory (LHAASO; http://english.ihep.cas.cn/lhaaso/; Bai et al. 2019) facility has recently commenced operation. LHAASO operates from a

high (>4400 m) plateau in China and comprises an array of solid particle detectors, water-Čerenkov detectors, and wide-field telescopes detecting Čerenkov and fluorescence light. The large collection area LHASSO achieves (more than 10 times larger than that of HAWC) will enable LHASSO to push very deep into the >1PeV gamma-ray band and thus further advance our understanding of PeVatrons. Its large collection also permits a highly sensitive search for transients. In the southern hemisphere, the Southern Wide-field Gamma-ray Observatory (SWGO; Albert et al. 2019) has been proposed and is based primarily on the water-Čerenkov technique. SWGO is designed to operate with a collection area at least five times larger than that of HAWC. Being in the southern hemisphere (high-altitude sites in Chile and Peru are under consideration), SWGO will access the Galactic Plane and thus the rich variety of Galactic gamma-ray sources. As for LHAASO, SWGO is expected to further improve our understanding of PeVatrons and transient sources. Similarly, the HiScore concept (Tluczykont et al. 2014) based on an array of air-Čerenkov detectors could offer excellent angular resolution (0.1°) for PeV gamma rays over a wide field of view. It is currently under development in Russia.

Although not a wide-field array, the TenTen concept (Rowell et al. 2008) considers a "sparse" array of at least 50 imaging Čerenkov telescopes over a wide ground area to achieve a 10km^2 collection area for energies >10 TeV up to at least 500 TeV in energy. The imaging Čerenkov telescopes can achieve an excellent angular resolution (<0.1°) and so are required for detailed morphological studies and comparisons with radio to X-ray images. With PeVatrons becoming a recognized class of gamma-ray sources and CTA's performance expected to have impact in this area, such large sparse array concepts will no doubt attract further attention over the next decade.

Following on further from the opportunities that the next generation of facilities will offer, serious consideration is now going into the development of TeV gamma-ray facilities distributed across Earth to provide 24 hr coverage of transients and variable sources. One such idea is the Čerenkov Ring (Ruhe et al. 2019) concept, which calls for Čerenkov imaging telescopes located across longitude bands in both the northern and southern hemispheres to enable 24 hr coverage. The telescopes would ideally be robotic for ease of operation, have a rapid response, and carry out automated searches or surveys for sources. These telescopes or small arrays of a few telescopes should be sufficiently sensitive to detect and characterize (i.e., determine energy spectra) sources in the 0.1 to 10s of TeV energy band. A threshold energy in the range of 0.1 TeV to 1 TeV is highly desirable to ensure the study of extragalactic sources suffering absorption on the EBL (e.g., AGN blazars and GRBs). Small arrays of two to five imaging Čerenkov telescopes have already clearly proved their worth (e.g., the HEGRA IACT System, Daum et al. 1997; HESS, https://www.mpi-hd.mpg.de/hfm/HESS/; VERITAS, https://veritas.sao.arizona.edu/; MAGIC, https://magic.mpp.mpg.de/) and can achieve arcminute-scale resolution under certain conditions (HESS Collaboration et al. 2018c; HESS Collaboration 2020), which is ideal for point-like transient sources. In the >10 TeV range, excellent performance is also predicted for similarly small arrays (e.g., Stamatescu et al. 2011). Further studies are warranted to explore the potential of small arrays utilizing Čerenkov cameras with large fields of

view (similar to those of the CTA) and optimized for high resolution. For full 24 hr coverage in the southern hemisphere, sites in Australia and Southern Africa are essential to complement CTA-South in Chile.

References

CTA: Cherenkov telescope array, https://www.cta-observatory.org/

CTA performance, https://www.flickr.com/photos/cta_observatory/26079109147/in/album-72157673853528865/

Cta performance, https://www.cta-observatory.org/wp-content/uploads/2019/04/CTA-Performance-prod3b-v2-South-20deg-ShortTerm.png

CTA Consortium 2019, Science with the Cherenkov Telescope Array (Singapore: World Scientific)

HAWC: High-altitude water cherenkov, https://www.hawc-observatory.org/

HESS: High energy stereoscopic system, https://www.mpi-hd.mpg.de/hfm/HESS/

How many known X-ray (and other) sources are there?, https://heasarc.gsfc.nasa.gov/docs/heasarc/headates/how_many_xray.html

LHAASO: Large high-altitude air shower observatory, http://english.ihep.cas.cn/lhaaso/

MAGIC: Major atmospheric gamma imaging cherenkov, https://magic.mpp.mpg.de/

TeVCat: Catalogue of tev gamma-ray sources, http://tevcat2.uchicago.edu/

VERITAS: Very energetic radiation imaging telescope array system, https://veritas.sao.arizona.edu/

Aab, A., Abreu, P., Aglietta, M., et al. 2016, PhRvD, 94, 082002

Aab, A., Abreu, P., Aglietta, M., et al. 2018, ApJ, 853, L29

Aab, A., Abreu, P., Aglietta, M., et al. 2017, JCAP, 2017, 009

Aartsen, M. G., Abbasi, R., Abdou, Y., et al. 2013, PhRvL, 111, 021103

Aartsen, M. G., Ackermann, M., Adams, J., et al. 2020, ApJ, 891, 9

Abbasi, R. U., Abe, M., Abu-Zayyad, T., et al. 2020, MNRAS, 492, 3984

Abbott, B. P., Abbott, R., Abbott, T. D., et al. 2016, PhRvL, 116, 061102

Abbott, B. P., Abbott, R., Abbott, T. D., et al. 2017, ApJ, 848, L12

Abdalla, H., Abe, H., Acero, F., et al. 2021, JCAP, 2021, 048

Abdalla, H., Adam, R., Aharonian, F., et al. 2019, Natur, 575, 464

Abdalla, H., Aharonian, F., Ait Benkhali, F., et al. 2018, JCAP, 2018, 037

Abdalla, H., Aharonian, F., Ait Benkhali, F., et al. 2019, ApJ, 870, 93

Abdallah, H., Abramowski, A., Aharonian, F., et al. 2018, PhRvL, 120, 201101

Abdallah, H., Adam, R., Aharonian, F., et al. 2020, PhRvD, 102, 062001

Abdo, A. A., Ackermann, M., Ajello, M., et al. 2010a, A&A, 523, L2

Abdo, A. A., Ackermann, M., Ajello, M., et al. 2011, Sci, 331, 739

Abdo, A. A., Ackermann, M., Ajello, M., et al. 2010b, Sci, 328, 725

Abdo, A. A., Ackermann, M., Ajello, M., et al. 2010c, A&A, 512, A7

Abdo, A. A., Ackermann, M., Ajello, M., et al. 2010d, A&A, 523, A46

Abdo, A. A., Ajello, M., Allafort, A., et al. 2013, ApJS, 208, 17

Abdo, A. A., Allen, B., Aune, T., et al. 2008, ApJ, 688, 1078

Abdo, A. A., Allen, B., Berley, D., et al. 2007a, ApJ, 658, L33

Abdo, A. A., Allen, B., Berley, D., et al. 2007b, ApJ, 664, L91

Abdo, A. A., Ackermann, M., Ajello, M., et al. 2010e, A&A, 524, A75

Abdollahi, S., Acero, F., Ackermann, M., et al. 2020, ApJS, 247, 33

Abdollahi, S., Ackermann, M., Ajello, M., et al. 2017, ApJ, 846, 34
Abdollahi, S., Ackermann, M., Ajello, M., et al. 2018, Sci, 362, 1031
Abeysekara, A. U., Albert, A., Alfaro, R., et al. 2017a, Sci, 358, 911
Abeysekara, A. U., Albert, A., Alfaro, R., et al. 2017b, ApJ, 843, 40
Abeysekara, A. U., Albert, A., Alfaro, R., et al. 2020, PhRvL, 124, 021102
Abeysekara, A. U., Archer, A., Aune, T., et al. 2018a, ApJ, 861, 134
Abeysekara, A. U., Archer, A., Benbow, W., et al. 2019, ApJ, 885, 150
Abeysekara, A. U., Benbow, W., Bird, R., et al. 2018b, ApJ, 867, L19
Abeysekara, A. U., Albert, A., Alfaro, R., et al. 2018c, Natur, 562, 82
Abramowski, A., Acero, F., Aharonian, F., et al. 2013, PhRvD, 88, 102003
Abramowski, A., Aharonian, F., Ait Benkhali, F., et al. 2014a, PhRvD, 90, 122007
Abramowski, A., Aharonian, F., Ait Benkhali, F., et al. 2014b, ApJ, 794, L1
Abramowski, A., Acero, F., Aharonian, F., et al. 2012, A&A, 537, A114
Acciari, V. A., Ansoldi, S., Antonelli, L. A., et al. 2019, MNRAS, 486, 4233
Acciari, V. A., Ansoldi, S., Antonelli, L. A., et al. 2021, ApJ, 908, 90
Acero, F., Aharonian, F., Akhperjanian, A. G., et al. 2010, MNRAS, 402, 1877
Acero, F., Aharonian, F., Akhperjanian, A. G., et al. 2009a, Sci, 326, 1080
Acero, F., Ballet, J., Decourchelle, A., et al. 2009b, A&A, 505, 157
Acero, F., Donato, D., Ojha, R., et al. 2013, ApJ, 779, 133
Acharyya, A., Adam, R., Adams, C., et al. 2021, JCAP, 2021, 057
Ackermann, M., Ajello, M., Albert, A., et al. 2015a, ApJ, 813, L41
Ackermann, M., Ajello, M., Albert, A., et al. 2017a, ApJ, 840, 43
Ackermann, M., Ajello, M., Albert, A., et al. 2014, Sci, 345, 554
Ackermann, M., Ajello, M., Albert, A., et al. 2017b, ApJ, 836, 208
Ackermann, M., Ajello, M., Allafort, A., et al. 2013, Sci, 339, 807
Ackermann, M., Ajello, M., Allafort, A., et al. 2011, Sci, 334, 1103
Ackermann, M., Ajello, M., Atwood, W. B., et al. 2015b, ApJ, 810, 14
Ackermann, M., Ajello, M., Atwood, W. B., et al. 2012, ApJ, 750, 3
Ackermann, M., Ajello, M., Baldini, L., et al. 2016, ApJ, 826, 1
Ackermann, M., Atwood, W. B., Baldini, L., et al. 2018, ApJ, 857, 49
Aharonian, F., Akhperjanian, A., Barrio, J., et al. 2001, A&A, 370, 112
Aharonian, F., Akhperjanian, A., Beilicke, M., et al. 2002, A&A, 393, L37
Aharonian, F., Akhperjanian, A., Beilicke, M., et al. 2005a, A&A, 431, 197
Aharonian, F., Akhperjanian, A. G., Anton, G., et al. 2009, A&A, 502, 749
Aharonian, F., Akhperjanian, A. G., Aye, K. M., et al. 2005b, Sci, 309, 746
Aharonian, F., Akhperjanian, A. G., Barres de Almeida, U., et al. 2008a, A&A, 477, 353
Aharonian, F., Akhperjanian, A. G., Barres de Almeida, U., et al. 2008b, A&A, 483, 509
Aharonian, F., Akhperjanian, A. G., Bazer-Bachi, A. R., et al. 2007a, ApJ, 664, L71
Aharonian, F., Akhperjanian, A. G., Bazer-Bachi, A. R., et al. 2008c, A&A, 481, 401
Aharonian, F., Akhperjanian, A. G., Bazer-Bachi, A. R., et al. 2006a, Natur, 439, 695
Aharonian, F., Akhperjanian, A. G., Bazer-Bachi, A. R., et al. 2006b, ApJ, 636, 777
Aharonian, F., Akhperjanian, A. G., Bazer-Bachi, A. R., et al. 2006c, Natur, 440, 1018
Aharonian, F., Akhperjanian, A. G., Bazer-Bachi, A. R., et al. 2007b, A&A, 464, 235
Aharonian, F., Akhperjanian, A. G., Bazer-Bachi, A. R., et al. 2006d, A&A, 460, 365
Aharonian, F., Akhperjanian, A. G., Bazer-Bachi, A. R., et al. 2006e, A&A, 460, 743
Aharonian, F. A. 2001, SSRv, 99, 187

Aharonian, F. A., & Atoyan, A. M. 1996, A&A, 309, 917
Aharonian, F. A., Atoyan, A. M., & Kifune, T. 1997, MNRAS, 291, 162
Aharonian, F. A., Bogovalov, S. V., & Khangulyan, D. 2012, Natur, 482, 507
Aharonian, F. A., Drury, L. O. C., Voelk, H. J., et al. 1994, A&A, 285, 645
Aharonian, F. A. 2013, Gamma-Ray Emission of Supernova Remnants and the Origin of Galactic Cosmic Rays (Dordrecht: Springer)
Aharonian, F., Peron, G., Yang, R., Casanova, S., & Zanin, R. 2020, PhRvD, 101, 083018
Aharonian, F., Yang, R., & de Oña Wilhelmi, E. 2019, NatAs, 3, 561
Aharonian, F. A. 2004, Very High Energy Cosmic Gamma Radiation: A Crucial Window on the Extreme Universe (Singapore: World Scientific)
Aharonian, F. A., Khangulyan, D., & Costamante, L. 2008d, MNRAS, 387, 1206
Aharonian, F., Akhperjanian, A. G., Aye, K.-M., et al. 2005b, A&A, 432, L25
Ahnen, M. L., Ansoldi, S., Antonelli, L. A., et al. 2017, A&A, 601, A33
Aielli, G., Assiro, R., Bacci, C., et al. 2006, NIMPA, 562, 92
Ajello, M., Albert, A., Anderson, B., et al. 2016, PhRvL, 116, 161101
Ajello, M., Angioni, R., Axelsson, M., et al. 2020a, ApJ, 892, 105
Ajello, M., Arimoto, M., Axelsson, M., et al. 2020b, ApJ, 890, 9
Ajello, M., Arimoto, M., Axelsson, M., et al. 2019, ApJ, 878, 52
Ajello, M., Atwood, W. B., Baldini, L., et al. 2017, ApJS, 232, 18
Ajello, M., Di Mauro, M., Paliya, V. S., & Garrappa, S. 2020c, ApJ, 894, 88
Albert, A., Alfaro, R., Alvarez, C., et al. 2020a, PhRvL, 124, 131101
Albert, A., Alfaro, R., Alvarez, C., et al. 2020b, JCAP, 2020, 026
Albert, A., Alfaro, R., Alvarez, C., et al. 2020c, ApJ, 896, L29
Albert, A., Alfaro, R., Alvarez, C., et al. 2020d, ApJ, 905, 76
Albert, A., Alfaro, R., Alvarez, C., et al. 2021, ApJL, 907, L30
Albert, A., Alfaro, R., Ashkar, H., et al. 2019, arXiv:1902.08429
Albert, J., Aliu, E., Anderhub, H., et al. 2007, ApJ, 665, L51
Alfaro, J. 2005, PhRvL, 94, 221302
Aliu, E., Anderhub, H., Antonelli, L. A., et al. 2008, Sci, 322, 1221
Alves Batista, R., Biteau, J., Bustamante, M., et al. 2019, FrASS, 6, 23
Amati, L., O'Brien, P., Götz, D., et al. 2018, AdSpR, 62, 191
Amelino-Camelia, G., Ellis, J., Mavromatos, N. E., Nanopoulos, D. V., & Sarkar, S. 1998, Natur, 393, 763
Amelino-Camelia, G. 2001, Natur, 410, 1065
Amenomori, M., Bao, Y. W., Bi, X. J., et al. 2021, PhRvL, 126, 141101
Anderson, L. D., Wang, Y., Bihr, S., et al. 2017, A&A, 605, A58
Ansoldi, S., Antonelli, L. A., Antoranz, P., et al. 2016, A&A, 585, A133
Antonucci, R. 1993, ARA&A, 31, 473
Arakawa, M., Hayashida, M., Khangulyan, D., & Uchiyama, Y. 2020, ApJ, 897, 33
Archer, A., Benbow, W., Bird, R., et al. 2020, ApJ, 896, 41
Archer, A., Benbow, W., Bird, R., et al. 2016, ApJ, 821, 129
Arzoumanian, Z., Baker, P. T., Blumer, H., et al. 2020, ApJ, 905, L34
Atkins, R., Benbow, W., Berley, D., et al. 2000, ApJ, 533, L119
Atwood, W. B., Abdo, A. A., Ackermann, M., et al. 2009, ApJ, 697, 1071
Axford, W. I., Leer, E., & Skadron, G. 1977, ICRC, 11, 132
Baade, W., & Zwicky, F. 1934, PhRv, 46, 76

Baghmanyan, V., Peron, G., Casanova, S., Aharonian, F., & Zanin, R. 2020, ApJ, 901, L4
Bai, X., Bi, B. Y., Bi, X. J., et al. 2019, arXiv:1905.02773
Ballesteros, G., Coronado-Blázquez, J., & Gaggero, D. 2020, PhLB, 808, 135624
Band, D., Matteson, J., Ford, L., et al. 1993, ApJ, 413, 281
Barkov, M. V., Aharonian, F. A., Bogovalov, S. V., Kelner, S. R., & Khangulyan, D. 2012, ApJ, 749, 119
Barrau, A., Bazer-Bachi, R., Beyer, E., et al. 1998, PhRA, 416, 278
Bartels, R., Krishnamurthy, S., & Weniger, C. 2016, PhRvL, 116, 051102
Bartoli, B., Bernardini, P., Bi, X. J., et al. 2014, ApJ, 790, 152
Bartoli, B., Bernardini, P., Bi, X. J., et al. 2015, ApJ, 806, 20
Becker Tjus, J., & Merten, L. 2020, PhR, 872, 1
Bell, A. R. 1978, MNRAS, 182, 147
Bell, A. R. 2004, MNRAS, 353, 550
Berger, E. 2014, ARA&A, 52, 43
Bertone, G., & Tait, T. M. P. 2018, Natur, 562, 51
Bignami, G. F., & Hermsen, W. 1983, ARA&A, 21, 67
Bird, A. J., Malizia, A., Bazzano, A., et al. 2007, ApJS, 170, 175
Biteau, J., Prandini, E., Costamante, L., et al. 2020, NatAs, 4, 124
Biteau, J., & Williams, D. A. 2015, ApJ, 812, 60
Blanch, O., et al. 2020, ATel, 14275
Bland-Hawthorn, J., Maloney, P. R., Sutherland, R., et al. 2019, ApJ, 886, 45
Blandford, R. D., & Ostriker, J. P. 1978, ApJ, 221, L29
Blandford, R., Meier, D., & Readhead, A. 2019, ARA&A, 57, 467
Blondin, J. M., Chevalier, R. A., & Frierson, D. M. 2001, ApJ, 563, 806
Bodaghee, A., Tomsick, J. A., Pottschmidt, K., et al. 2013, ApJ, 775, 98
Bogovalov, S. V., & Aharonian, F. A. 2000, MNRAS, 313, 504
Boley, F. I., & Macoy, N. H. 1961, RScI, 32, 1359
Bordas, P., Yang, R., Kafexhiu, E., & Aharonian, F. 2015, ApJ, 807, L8
Bordas, P. 2020, NatAs, 4, 1132
Bouchet, L., Jourdain, E., Roques, J. P., et al. 2008, ApJ, 679, 1315
Bouchet, L., Jourdain, E., & Roques, J.-P. 2015, ApJ, 801, 142
Braiding, C., Wong, G. F., Maxted, N. I., et al. 2018, PASA, 35, e029
Brennan, M. H., Malos, J., Millar, D. D., & Wallace, C. S. 1958, Natur, 182, 973
Bulgarelli, A., Fioretti, V., Parmiggiani, N., et al. 2019, A&A, 627, A13
Bykov, A. M., & Toptygin, I. N. 2001, AstL, 27, 625
Cao, Z., Aharonian, F. A., An, Q., et al. 2021, Natur, 594, 33
Caraveo, P. A. 2014, ARA&A, 52, 211
Carr, B., & Kühnel, F. 2020, ARNPS, 70, 355
Casanova, S., Aharonian, F. A., Fukui, Y., et al. 2010, PASJ, 62, 769
Casse, M., & Paul, J. A. 1980, ApJ, 237, 236
Cataldo, M., Pagliaroli, G., Vecchiotti, V., & Villante, F. L. 2020, ApJ, 904, 85
Celli, S., Morlino, G., Gabici, S., & Aharonian, F. A. 2019, MNRAS, 487, 3199
Cesarsky, C. J., & Montmerle, T. 1983, SSRv, 36, 173
Chang, C., Konopelko, A., & Cui, W. 2008, ApJ, 682, 1177
Cherenkov Telescope Array Consortium, Acharya, B. S., Agudo, I., et al. 2019 Science with the Cherenkov Telescope Array (Singapore: World Scientific)

Chernyakova, M., & Malyshev, D. 2020, in Multifrequency Behaviour of High Energy Cosmic Sources—XIII, 45
Cheung, C. C., Jean, P., Shore, S. N., et al. 2016, ApJ, 826, 142
Chiaro, G., Salvetti, D., Mura, G. L., et al. 2016, MNRAS, 462, 3180
Chomiuk, L., Metzger, B. D., & Shen, K. J. 2020, arXiv:2011.08751
Claret, A. 2018, in 42nd COSPAR Scientific Assembly, Vol. 42, E1.15-15-18
Claussen, M. J., Frail, D. A., Goss, W. M., & Gaume, R. A. 1997, ApJ, 489, 143
Cooper, A. J., Gaggero, D., Markoff, S., & Zhang, S. 2020, MNRAS, 493, 3212
Corbet, R. H. D., Chomiuk, L., Coe, M. J., et al. 2019, ApJ, 884, 93
Crocker, R. M., & Aharonian, F. 2011, PhRvL, 106, 101102
Crocker, R. M., Bicknell, G. V., Taylor, A. M., & Carretti, E. 2015, ApJ, 808, 107
Cui, Y., Yeung, P. K. H., Tam, P. H. T., & Pühlhofer, G. 2018, ApJ, 860, 69
Dame, T. M., Hartmann, D., & Thaddeus, P. 2001, ApJ, 547, 792
Daugherty, J. K., & Harding, A. K. 1982, ApJ, 252, 337
Daugherty, J. K., & Harding, A. K. 1983, ApJ, 273, 761
Daum, A., Hermann, G., & Heß, M. 1997, APh, 8, 1
de Angelis, A., Tatischeff, V., Grenier, I. A., et al. 2018, JHEAp, 19, 1
De Angelis, A., Tatischeff, V., Tavani, M., et al. 2017, ExA, 44, 25
de Angelis, A., Galanti, G., & Roncadelli, M. 2011, PhRvD, 84, 105030
de Jager, O. C., Ferreira, S. E. S., & Djannati-Ataï, A. 2009, arXiv:0906.2644
de Naurois, M., & Mazin, D. 2015, CRPhy, 16, 610
de Naurois, M., et al. 2019, ATel, 13052
de Wilt, P., Rowell, G., Walsh, A. J., et al. 2017, MNRAS, 468, 2093
Desai, A., Helgason, K., Ajello, M., et al. 2019, ApJ, 874, L7
Di Mauro, M., Manconi, S., Negro, M., & Donato, F. 2021, PhRvD, 104, 103002
Dickey, J. M., McClure-Griffiths, N., Gibson, S. J., et al. 2013, PASA, 30, e003
Diehl, R., Dupraz, C., Bennett, K., et al. 1995, A&A, 298, 445
Doert, M., & Errando, M. 2014, ApJ, 782, 41
Domínguez, A., Wojtak, R., Finke, J., et al. 2019, ApJ, 885, 137
Domínguez, A., & Ajello, M. 2015, ApJ, 813, L34
Doro, M. 2017, EPJWC, 136, 01003
Drury, L. O. 1983, RPPh, 46, 973
Drury, L. O., Aharonian, F. A., & Voelk, H. J. 1994, A&A, 287, 959
Dubner, G. M., Holdaway, M., Goss, W. M., & Mirabel, I. F. 1998, AJ, 116, 1842
Dubus, G. 2013, A&ARv, 21, 64
Eger, P., Rowell, G., Kawamura, A., et al. 2011, A&A, 526, A82
Einecke, S. 2016, Galax, 4, 14
Esposito, J. A., Hunter, S. D., Kanbach, G., & Sreekumar, P. 1996, ApJ, 461, 820
Evoli, C., Gaggero, D., Vittino, A., et al. 2017, JCAP, 2017, 015
Fanaroff, B. L., & Riley, J. M. 1974, MNRAS, 167, 31P
Farnier, C., Walter, R., & Leyder, J. C. 2011, A&A, 526, A57
Federici, S., Pohl, M., Telezhinsky, I., Wilhelm, A., & Dwarkadas, V. V. 2015, A&A, 577, A12
Fegan, D. 2019, Cherenkov Reflections. Gamma-Ray Imaging and the Evolution of TeV Astronomy (World Scientific: Singapore)
Feijen, K., Rowell, G., Einecke, S., et al. 2020, PASA, 37, e056
Fermi-LAT Collaboration, Abdo, A. A., Ackermann, M., et al. 2009, Sci, 326, 1512

Fermi-LAT Collaboration, Ajello, M., Atwood, W. B., et al. 2021, NatAs, 5, 385
Fichtel, C. E., Hartman, R. C., Kniffen, D. A., et al. 1975, ApJ, 198, 163
Fossati, G., Maraschi, L., Celotti, A., Comastri, A., & Ghisellini, G. 1998, MNRAS, 299, 433
Frail, D. A., Goss, W. M., & Slysh, V. I. 1994, ApJ, 424, L111
Fujita, Y., Ohira, Y., Tanaka, S. J., & Takahara, F. 2009, ApJ, 707, L179
Fukui, Y., Sano, H., Sato, J., et al. 2012, ApJ, 746, 82
Funk, S., Hinton, J. A., & De Jager, O. C. 2008, ICRC, 2, 605
Gabici, S., & Aharonian, F. A. 2014, MNRAS, 445, L70
Gabici, S. 2011, MmSAI, 82, 760
Gabici, S. 2014, in IAU Symp. 296, Supernova Environmental Impacts, ed. A. Ray, & R. A. McCray (Cambridge: Cambridge Univ. Press), 320
Gabici, S., & Aharonian, F. A. 2007, ApJ, 665, L131
Gabici, S., Aharonian, F. A., & Blasi, P. 2007, Ap&SS, 309, 365
Gaensler, B. M., & Slane, P. O. 2006, ARA&A, 44, 17
Gaisser, T., Engel, R., & Resconi, E. 2016, Cosmic Rays and Particle Physics (2nd ed.; Cambridge: Cambridge Univ. Press)
Galbraith, W., & Jelley, J. V. 1953, Natur, 171, 349
Gehrels, N., Macomb, D. J., Bertsch, D. L., Thompson, D. J., & Hartman, R. C. 2000, Natur, 404, 363
Ghisellini, G., Righi, C., Costamante, L., & Tavecchio, F. 2017, MNRAS, 469, 255
Ghisellini, G. 2016, Galax, 4, 36
Giacinti, G., Mitchell, A. M. W., López-Coto, R., et al. 2020, A&A, 636, A113
Gingrich, D. M., Boone, L. M., Bramel, D., et al. 2005, ITNS, 52, 2977
Ginzburg, V. L., & Syrovatskii, S. I. 1964, The Origin of Cosmic Rays (Amsterdam: Elsevier)
Green, A. J., Reeves, S. N., & Murphy, T. 2014, PASA, 31, e042
Grenier, I. A., & Harding, A. K. 2015, CRPhy, 16, 641
Grindlay, J. E., Helmken, H. F., Brown, R. H., Davis, J., & Allen, L. R. 1975, ApJ, 197, L9
Guépin, C., Rinchiuso, L., Kotera, K., et al. 2018, JCAP, 2018, 042
Guo, F., & Mathews, W. G. 2012, ApJ, 756, 181
Kulikov, G. V., & Khristiansen, G. B. 1958, JETP, 35, 635
HESS Collaboration 2020, NatAs, 4, 167
HESS Collaboration, Abdalla, H., Abramowski, A., et al. 2018e, A&A, 612, A9
HESS Collaboration, Abdalla, H., Abramowski, A., et al. 2018d, A&A, 612, A8
HESS Collaboration, Abdalla, H., Abramowski, A., et al. 2017, A&A, 606, A59
HESS Collaboration, Abdalla, H., Abramowski, A., et al. 2018b, A&A, 612, A2
HESS Collaboration, Abdalla, H., Abramowski, A., et al. 2018c, A&A, 612, A6
HESS Collaboration, Abdalla, H., Abramowski, A., et al. 2018f, A&A, 612, A11
HESS Collaboration, Abdalla, H., Abramowski, A., et al. 2018a, A&A, 612, A1
HESS Collaboration, Abdalla, H., Adam, R., et al. 2020c, A&A, 635, A167
HESS Collaboration, Abdalla, H., Adam, R., et al. 2020a, Natur, 582, 356
HESS Collaboration, Abdalla, H., Adam, R., et al. 2020b, A&A, 644, A112
HESS Collaboration, Abramowski, A., Aharonian, F., et al. 2016, Natur, 531, 476
HESS Collaboration, Abramowski, A., & Acero, F. 2011, A&A, 531, L18
HESS Collaboration, Abdalla, H., Aharonian, F., et al. 2018g, A&A, 620, A66
HESS Collaboration, Abdalla, H., Aharonian, F., et al. 2018h, A&A, 617, A73
HESS Collaboration, Abdalla, H., Aharonian, F., et al. 2019, A&A, 621, A116

HESS Collaboration, Abramowski, A., Acero, F., et al. 2012, A&A, 548, A46
HESS Collaboration, Abramowski, A., Acero, F., et al. 2011, A&A, 525, A46
HESS Collaboration, Abramowski, A., Aharonian, F., et al. 2015, Sci, 347, 406
Harding, A. K., & Kalapotharakos, C. 2015, ApJ, 811, 63
Hartman, R. C., Bertsch, D. L., Bloom, S. D., et al. 1999, ApJS, 123, 79
Herold, L., & Malyshev, D. 2019, A&A, 625, A110
Hill, D. A., & Porter, N. 1961, Natur, 191, 690
Hillas, A. M. 1984, ARA&A, 22, 425
Hillas, A. M. 1985, ICRC, 3, 445
Hillas, A. M. 2005, JPhG, 31, R95
Hillas, A. M. 2013, APh, 43, 19
Hinton, J. A., & Hofmann, W. 2009, ARA&A, 47, 523
Hirotani, K. 2011, ApJ, 733, L49
Hirotani, K. 2013, ApJ, 766, 98
Hoof, S., Geringer-Sameth, A., & Trotta, R. 2020, JCAP, 2020, 012
Hooper, D., & Serpico, P. D. 2007, PhRvL, 99, 231102
Horns, D., Hoffmann, A. I. D., Santangelo, A., Aharonian, F. A., & Rowell, G. P. 2007, A&A, 469, L17
Humphreys, R. M., & Martin, J. C. 2012, in Eta Carinae and the Supernova Impostors (Berlin: Springer), 1
Hurley-Walker, N., Callingham, J. R., Hancock, P. J., et al. 2017, MNRAS, 464, 1146
IceCube Collaboration, M. G., Aartsen, M., & Ackermann, M. 2018a, Sci, 361, 147
IceCube Collaboration, M. G., Aartsen, M., & Ackermann, M. 2018b, Sci, 361, eaat1378
Ilie, C. 2019, PASP, 131, 111001
Inoue, T., Yamazaki, R., Inutsuka, S. i., & Fukui, Y. 2012, ApJ, 744, 71
Ioka, K., Razzaque, S., Kobayashi, S., & Mészáros, P. 2005, ApJ, 633, 1013
Jackson, J. M., Rathborne, J. M., Shah, R. Y., et al. 2006, ApJS, 163, 145
Jóhannesson, G., Porter, T. A., & Moskalenko, I. V. 2018, ApJ, 856, 45
Jones, P. A., Burton, M. G., Cunningham, M. R., et al. 2012, MNRAS, 419, 2961
Jouvin, L., Lemière, A., & Terrier, R. 2020, A&A, 644, A113
Kafexhiu, E., Aharonian, F., Taylor, A. M., & Vila, G. S. 2014, PhRvD, 90, 123014
Karwin, C. M., Murgia, S., Campbell, S., & Moskalenko, I. V. 2019, ApJ, 880, 95
Kelner, S. R., Aharonian, F. A., & Bugayov, V. V. 2006, PhRvD, 74, 034018
Kennel, C. F., & Coroniti, F. V. 1984, ApJ, 283, 710
Kifune, T. 1996, NCimC, 19C, 953
Kifune, T. 1999, ApJ, 518, L21
Kimura, S. S., Murase, K., & Mészáros, P. 2020, ApJ, 904, 188
Kissmann, R., Werner, M., Reimer, O., & Strong, A. W. 2015, APh, 70, 39
Klebesadel, R. W., Strong, I. B., & Olson, R. A. 1973, ApJ, 182, L85
Knödlseder, J., Jean, P., Lonjou, V., et al. 2005, A&A, 441, 513
Kong, A. K. H., Hui, C. Y., & Cheng, K. S. 2010, ApJ, 712, L36
Kosack, K., Badran, H. M., Bond, I. H., et al. 2004, ApJ, 608, L97
Kostelecký, V. A., & Samuel, S. 1989, PhRvD, 39, 683
Kraushaar, W. L., & Clark, G. W. 1962, PhRvL, 8, 106
Kraushaar, W. L., Clark, G. W., Garmire, G. P., et al. 1972, ApJ, 177, 341
Krymskii, G. F. 1977, DoSSR, 234, 1306

Lacki, B. C. 2014, MNRAS, 444, L39
Lacroix, T., Silk, J., Moulin, E., & BÅ'hm, C. 2016, PhRvD, 94, 123008
Lagage, P. O., & Cesarsky, C. J. 1983, A&A, 125, 249
Lau, J. C., Rowell, G., Burton, M. G., et al. 2017a, MNRAS, 464, 3757
Lau, J. C., Rowell, G., Voisin, F., et al. 2019, MNRAS, 483, 3659
Lau, J. C., Rowell, G., Voisin, F., et al. 2017b, PASA, 34, e064
Lazendic, J. S., Slane, P. O., Gaensler, B. M., et al. 2004, ApJ, 602, 271
Lemiere, A., Terrier, R., & Djannati-Ataï, A. 2005, ICRC, 4, 105
Letessier-Selvon, A., & Stanev, T. 2011, RvMP, 83, 907
Li, J., Torres, D. F., Liu, R.-Y., et al. 2020a, NatAs, 4, 1177
Li, K.-L., Hambsch, F.-J., Munari, U., et al. 2020b, ApJ, 905, 114
Li, X., Duan, K., Jiang, W., Shen, Z., & Salinas, M. M. 2021, PoS, 358, 576
Lien, A., Sakamoto, T., Barthelmy, S. D., et al. 2016, ApJ, 829, 7
Linden, T., Auchettl, K., Bramante, J., et al. 2017, PhRvD, 96, 103016
Lopez, L. A., Grefenstette, B. W., Auchettl, K., Madsen, K. K., & Castro, D. 2020, ApJ, 893, 144
Macias, O., Gordon, C., Crocker, R. M., et al. 2018, NatAs, 2, 387
Madejski, G., & Sikora, M. 2016, ARA&A, 54, 725
MAGIC Collaboration, Ahnen, M. L., Ansoldi, S., et al. 2017, ApJS, 232, 9
MAGIC Collaboration, Acciari, V. A., Ansoldi, S., et al. 2020a, A&A, 643, L14
MAGIC Collaboration, Acciari, V. A., Ansoldi, S., et al. 2019a, Natur, 575, 455
MAGIC Collaboration, Acciari, V. A., Ansoldi, S., et al. 2020b, A&A, 642, A190
MAGIC Collaboration, Acciari, V. A., Ansoldi, S., et al. 2020c, MNRAS, 497, 3734
MAGIC Collaboration, Acciari, S., Ansoldi, S., et al. 2019b, Natur, 575, 459
MAGIC Collaboration, Ahnen, M. L., & Ansoldi, S. 2018, A&A, 619, A45
Malyshev, D., Pühlhofer, G., Santangelo, A., & Vink, J. 2019, arXiv:1903.03045
Malyshev, D., Zdziarski, A. A., & Chernyakova, M. 2013, MNRAS, 434, 2380
Mandarakas, N., Blinov, D., Liodakis, I., et al. 2019, A&A, 623, A61
Manolakou, K., Horns, D., & Kirk, J. G. 2007, A&A, 474, 689
Margon, B. 1984, ARA&A, 22, 507
Martínez-Huerta, H., Lang, R. G., & de Souza, V. 2020, Symm, 12, 1232
Matsumoto, H., Uchiyama, H., Sawada, M., et al. 2008, PASJ, 60, S163
Matthews, J. H., Bell, A. R., & Blundell, K. M. 2020, NewAR, 89, 101543
Mavromatos, N. E., & Mitsou, V. A. 2020, IJMPA, 35, 2030012–191
Maxted, N., Rowell, G., de Wilt, P., et al. 2017, in AIP Conf. Ser. 1792, High Energy Gamma-Ray Astronomy (Melville, NY: AIP), 040034
Maxted, N. I., Braiding, C., Wong, G. F., et al. 2018, MNRAS, 480, 134
Maxted, N. I., Filipović, M. D., Hurley-Walker, N., et al. 2019, ApJ, 885, 129
Maxted, N. I., Rowell, G. P., Dawson, B. R., et al. 2012, MNRAS, 422, 2230
McClure-Griffiths, N. M., Dickey, J. M., Gaensler, B. M., et al. 2005, ApJS, 158, 178
McEnery, J., van der Horst, A., Dominguez, A., et al. 2019, BAAS, 51, 245
Mészáros, P. 2002, ARA&A, 40, 137
Meszaros, P., & Rees, J. 1993, ApJ, 405, 278
Migliari, S., Fender, R., & Méndez, M. 2002, Sci, 297, 1673
Millar, D. D., Malos, J., Wallace, C. S., & McCusker, C. B. A. 1962, JPSJS, 17, 114
Mirabel, I. F., & Rodríguez, L. F. 1999, ARA&A, 37, 409
Mirzoyan, R. 2014, APh, 53, 91

Mitchell, A. M. W., Rowell, G. P., Celli, S., & Einecke, S. 2021, MNRAS, 503, 3522
Mizuno, A., & Fukui, Y. 2004, in ASP Conf. Ser. 317, Milky Way Surveys: The Structure and Evolution of our Galaxy, ed. D. Clemens, R. Shah, & T. Brainerd (San Francisco, CA: ASP), 59
Mochol, I., & Petri, J. 2015, MNRAS, 449, L51
Montmerle, T. 1979, ApJ, 231, 95
Mooley, K. P., Deller, A. T., Gottlieb, O., et al. 2018, Natur, 561, 355
Moriguchi, Y., Tamura, K., Tawara, Y., et al. 2005, ApJ, 631, 947
Morrison, P. 1958, NCim, 7, 858
Mou, G., Yuan, F., Bu, D., Sun, M., & Su, M. 2014, ApJ, 790, 109
Müller, C., Kadler, M., Ojha, R., et al. 2018, A&A, 610, A1
Murase, K., Thompson, T. A., Lacki, B. C., & Beacom, J. F. 2011, PhRvD, 84, 043003
Naito, T., & Takahara, F. 1994, JPhG, 20, 477
Nava, L., & Gabici, S. 2013, MNRAS, 429, 1643
Nesterova, N. M., & Čudakov, A. E. 1955, JETP, 28, 384
Oh, K., Koss, M., Markwardt, C. B., et al. 2018, ApJS, 235, 4
Ojha, R., Kadler, M., Böck, M., et al. 2010, A&A, 519, A45
Paciesas, W. S., Meegan, C. A., Pendleton, G. N., et al. 1999, ApJS, 122, 465
Pacini, F., & Salvati, M. 1973, ApJ, 186, 249
Padovani, M., Galli, D., & Glassgold, A. E. 2009, A&A, 501, 619
Padovani, P., Alexander, D. M., Assef, R. J., et al. 2017, A&ARv, 25, 2
Panessa, F., Baldi, R. D., Laor, A., Padovani, P., Behar, E., & McHardy, I. 2019, NatAs, 3, 387
Paré, E., Balauge, B., Bazer-Bachi, R., et al. 2002, NIMPA, 490, 71
Paredes, J. M., & Bordas, P. 2019, in Frontier Research in Astrophysics—III, 44
Parizot, E., Marcowith, A., van der Swaluw, E., Bykov, A. M., & Tatischeff, V. 2004, A&A, 424, 747
Patrizii, L., & Spurio, M. 2015, ARNPS, 65, 279
Patrizii, L., Sahnoun, Z., & Togo, V. 2019, RSPTA, 377, 20180328
Pe'er, A. 2019, Galax, 7, 33
Peng, F.-K., Zhang, H.-M., Wang, X.-Y., Wang, J.-F., & Zhi, Q.-J. 2019, ApJ, 884, 91
Peters, B. 1961, NCim, 22, 800
Pinkau, K. 2009, ExA, 25, 157
Piran, T. 1999, PhR, 314, 575
Pliasheshnikov, A. V., & Bignami, G. F. 1985, NCimC, 8, 39
Porter, T. A., Jóhannesson, G., & Moskalenko, I. V. 2017, ApJ, 846, 67
Porter, T. A., Jóhannesson, G., & Moskalenko, I. V. 2019, ApJ, 887, 250
Porter, T. A., Rowell, G. P., Jóhannesson, G., & Moskalenko, I. V. 2018, PhRvD, 98, 041302
Predehl, P., Sunyaev, R. A., Becker, W., et al. 2020, Natur, 588, 227
Principe, G., Mitchell, A. M. W., Caroff, S., et al. 2020, A&A, 640, A76
Recchia, S., Gabici, S., Aharonian, F. A., & Niro, V. 2021, ApJ, 914, 135
Rees, M. J., & Gunn, J. E. 1974, MNRAS, 167, 1
Reich, W., & Sun, X.-H. 2019, RAA, 19, 045
Reimer, O. 2001, Unidentified Gamma-Ray Sources (Berlin: Springer)
Reitberger, K., Reimer, A., Reimer, O., & Takahashi, H. 2015, A&A, 577, A100
Reynolds, C., Ueda, Y., Awaki, H., et al. 2014, arXiv:1412.1177
Reynolds, S. P., & Chevalier, R. A. 1984, ApJ, 278, 630
Reynolds, S. P., Pavlov, G. G., Kargaltsev, O., et al. 2017, SSRv, 207, 175

Rieger, F. 2019, Galax, 7, 28
Roland, D. 2016, JPhCS, 703, 012001
Romero, G. E., Benaglia, P., & Torres, D. F. 1999, A&A, 348, 868
Rowell, G. P., Stamatescu, V., Clay, R. W., et al. 2008, NIMPA, 588, 48
Ruhe, T., Elsässer, D., Rhode, W., Nöthe, M., & Brügge, K. 2019, EPJWC, 207, 03002
Sabatini, S., Tavani, M., Striani, E., et al. 2010, ApJ, 712, L10
Safi-Harb, S., & Ögelman, H. 1997, ApJ, 483, 868
Sahakyan, N., Baghmanyan, V., & Zargaryan, D. 2018, A&A, 614, A6
Sanchez, D. A., Fegan, S., & Giebels, B. 2013, A&A, 554, A75
Sano, H., Inoue, T., Tokuda, K., et al. 2020, ApJ, 904, L24
Sano, H., Tanaka, T., Torii, K., et al. 2013, ApJ, 778, 59
Sano, H., Yamane, Y., Voisin, F., et al. 2017, ApJ, 843, 61
Schael, S., Atanasyan, A., Berdugo, J., et al. 2019, NIMPA, 944, 162561
Schinzel, F. K., Petrov, L., Taylor, G. B., & Edwards, P. G. 2017, ApJ, 838, 139
Schönfelder, V., Bennett, K., Blom, J. J., et al. 2000, A&AS, 143, 145
Smith, A. J. 2005, ICRC, 10, 227
Sobacchi, E., Sormani, M. C., & Stamerra, A. 2016, MNRAS, 465, 161
Spengler, G., & Schwanke, U. 2011, ICRC, 5, 105
Spengler, G. 2020, A&A, 633, A138
Spir-Jacob, M., Djannati-Ataï, A., & Mohrmann, L. 2019, arXiv:1908.06464
Spurio, M. 2015, The Sky Seen in Gamma-rays (Cham: Springer)
Sreekumar, P., Bertsch, D. L., Dingus, B. L., et al. 1992, ApJ, 400, L67
Stamatescu, V., Rowell, G. P., Denman, J., et al. 2011, APh, 34, 886
Stecker, F. W. 2003, APh, 20, 85
Stecker, F. W., & Glashow, S. L. 2001, APh, 16, 97
Steppa, C., & Egberts, K. 2020, A&A, 643, A137
Stil, J. M., Taylor, A. R., Dickey, J. M., et al. 2006, AJ, 132, 1158
Stone, E. C., Cummings, A. C., McDonald, F. B., et al. 2013, Sci, 341, 150
Stone, E., Cummings, A., Heikkila, B., & Lal, N. 2019, NatAs, 3, 11
Strong, A. W., & Moskalenko, I. V. 1998, ApJ, 509, 212
Su, M., Slatyer, T. R., & Finkbeiner, D. P. 2010, ApJ, 724, 1044
Sudoh, T., Inoue, Y., & Khangulyan, D. 2020, ApJ, 889, 146
Sudoh, T., Linden, T., & Beacom, J. F. 2019, PhRvD, 100, 043016
Sun, X.-N., Yang, R.-Z., Liu, B., Xi, S.-Q., & Wang, X.-Y. 2019, A&A, 626, A113
Sun, X.-N., Yang, R.-Z., & Wang, X.-Y. 2020, MNRAS, 494, 3405
Tang, X. 2019, MNRAS, 482, 3843
Tavani, M., Bulgarelli, A., Piano, G., et al. 2009, Natur, 462, 620
Tavani, M., Bulgarelli, A., Vittorini, V., et al. 2011, Sci, 331, 736
Taylor, A. R., Gibson, S. J., Peracaula, M., et al. 2003, AJ, 125, 3145
Thompson, D. J. 2015, CRPhy, 16, 600
Tluczykont, M., Hampf, D., Horns, D., et al. 2014, APh, 56, 42
Tompkins, D. R. 1965, PhRv, 138, 248
Topchiev, N. P., Galper, A. M., Bonvicini, V., et al. 2016, JPhCS, 675, 032010
Torres, D. F., Romero, G. E., Dame, T. M., Combi, J. A., & Butt, Y. M. 2003, PhR, 382, 303
Torresi, E. 2020, in IAU Proc. 342, Perseus in Sicily: From Black Hole to Cluster Outskirts (Cambridge: Cambridge Univ. Press), 158

Umemoto, T., Minamidani, T., Kuno, N., et al. 2017, PASJ, 69, 78
Urry, C. M., & Padovani, P. 1995, PASP, 107, 803
Van Etten, A., & Romani, R. W. 2011, ApJ, 742, 62
Vasileiou, V., Jacholkowska, A., Piron, F., et al. 2013, PhRvD, 87, 122001
VERITAS Collaboration, Acciari, V. A., Aliu, E., et al. 2009, Natur, 462, 770
VERITAS Collaboration, Aliu, E., Arlen, T., et al. 2011, Sci, 334, 69
Viganò, D., & Torres, D. 2015, MNRAS, 449, 3755
Voelk, H. J., & Forman, M. 1982, ApJ, 253, 188
Voisin, F., Rowell, G., Burton, M. G., et al. 2016, MNRAS, 458, 2813
Voisin, F. J., Rowell, G. P., Burton, M. G., et al. 2019, PASA, 36, e014
von Kienlin, A., Meegan, C. A., Paciesas, W. S., et al. 2020, ApJ, 893, 46
Walsh, A. J., Breen, S. L., Britton, T., et al. 2011, MNRAS, 416, 1764
Wang, Y., Beuther, H., Rugel, M. R., et al. 2020, A&A, 634, A83
Waxman, E., & Loeb, A. 2001, PhRvL, 87, 071101
Weekes, T. C. 1988, PhR, 160, 1
Weekes, T. C., Cawley, M. F., Fegan, D. J., et al. 1989, ApJ, 342, 379
Wierzcholska, A., & Wagner, S. J. 2016, MNRAS, 458, 56
Woosley, S. E., & Bloom, J. S. 2006, ARA&A, 44, 507
Xi, S.-Q., Liu, R.-Y., Wang, X.-Y., et al. 2020a, ApJ, 896, L33
Xi, S.-Q., Zhang, H.-M., Liu, R.-Y., & Wang, X.-Y. 2020b, ApJ, 901, 158
Xing, Y., & Wang, Z. 2006, arXiv:2006.15790
Yamazaki, R., Kohri, K., Bamba, A., et al. 2006, MNRAS, 371, 1975
Yan, H., Lazarian, A., & Schlickeiser, R. 2012, ApJ, 745, 140
Yang, R.-z., & Aharonian, F. 2016, A&A, 589, A117
Yang, R.-z., & Aharonian, F. 2017, A&A, 600, A107
Yang, R.-z., de Oña Wilhelmi, E., & Aharonian, F. 2018, A&A, 611, A77
Yoneda, H., Makishima, K., Enoto, T., et al. 2020, PhRvL, 125, 111103
Zdziarski, A. A., Malyshev, D., Chernyakova, M., & Pooley, G. G. 2017, MNRAS, 471, 3657
Zhang, C., Liang, Y.-F., Li, S., et al. 2018, PhRvD, 97, 063009
Zhang, H.-M., Xi, S.-Q., Liu, R.-Y., et al. 2020, ApJ, 889, 12
Zirakashvili, V. N., & Aharonian, F. 2007, A&A, 465, 695
Zirakashvili, V. N., & Aharonian, F. A. 2010, ApJ, 708, 965
Zubovas, K., King, A. R., & Nayakshin, S. 2011, MNRAS, 415, L21